

## Chapter 1: Introduction to polymer photovoltaic cells

*Forenote: Much of the following chapter is from: Bilby, et al., Pure Appl. Chem. 83, [1], 127 (2011).*

Organic photovoltaics have commanded quite an interest in the renewable energy devices research community [1]. These devices will take advantage of the vast resource that is sunlight as well as relatively inexpensive processing routes. Polymer solar cells (PSCs), due to their solution processability, show promise to eventually be cost competitive with conventional fossil fuel based electricity generation technologies. Roll-to-roll processing enables large scale, morphology optimized production of these devices [2-5]. Thus, increasing device efficiency and lifetime through device and polymer design remain the primary obstacles to cost competitiveness [3-5]. However, with record power conversion efficiencies (PCEs) reaching 11.1% and lifetimes greater than 1 year, these devices are on track to become economically viable [6,7].

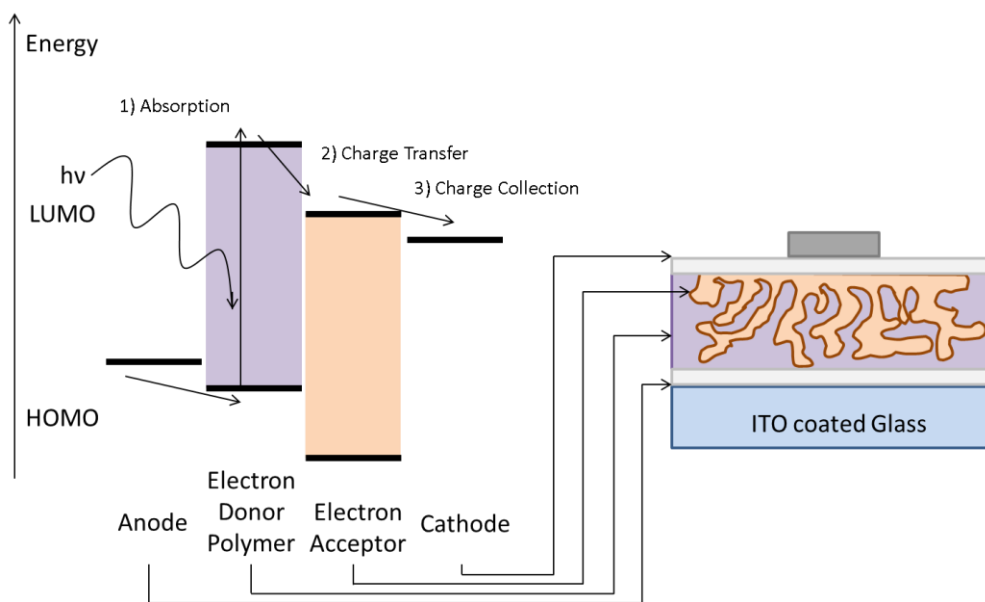


Figure 1.1: A simplified schematic of current production and BHJ morphology in an organic photovoltaic fabricated on an indium-tin oxide (ITO) anode.

A brief explanation of the operational physics, as portrayed in Figure 1.1, of PSCs provides the foundation for device improvement through molecular design. First a photon, of sufficient energy to overcome the highest occupied (HOMO) to lowest unoccupied (LUMO) molecular orbital energy level band gap of the conjugated polymer, is absorbed. This creates a charge neutral, tightly bound electron hole pair known as an exciton. In order to extract this energy, the exciton must diffuse to an interface with an electron accepting material (typically phenyl C61 butyric acid methyl ester (PCBM)) where charge transfer rapidly takes place, splitting the exciton into a hole and an electron [8-10]. The separated charges are then conducted to their respective electrodes to power an external circuit.

The power conversion physics combine with material properties to impose constraints on the fabrication and performance of the devices. For instance, the exciton diffusion length in conjugated polymers is typically very short; in a very common electron donor polymer, poly(3-hexylthiophene) (P3HT, Figure 1.2 a), the exciton diffusion length is about 8.5 nm [9,11]. This means that in a device which is thick enough to absorb most of the incident sunlight (about 240 nm thick) most of the excitons will recombine rather than separate into useful charge [12]. This deficiency is overcome by using a bulk-heterojunction (BHJ) device morphology; interpenetrating domains of the electron acceptor and donor materials provide nearby charge separation interfaces wherever an exciton may form, as shown in Figure 1.1 [13]. Additionally, charge carrier mobilities in PSCs are quite low, typically ranging from  $10^{-6}$  to  $10^{-1}$   $\text{cm}^2\text{V}^{-1}\text{s}^{-1}$ , limiting the distance charges can travel before succumbing to recombination (and therefore limiting the overall device thickness) [14-16]. Thus, compromises are made with regards to device thickness in order to optimize both device current density and absorption [16].

Innovative molecular design seeks to take advantage of the operational physics of the devices in order to overcome material limitations in PSCs. This allows for enhanced open circuit voltage ( $V_{oc}$ ), short circuit current density ( $J_{sc}$ ), and fill factor leading to an increased PCE [17-21]. The following discussion will present many design routes which have been taken to tune morphology, polymer packing and molecular orbital energy levels, among other things, of electron donating conjugated polymer materials. The influence of these design changes on the PSC performance via the aforementioned operational physics will also be discussed. These ideas

represent some basic molecular design methods to improve PSCs, and they provide an underpinning for future PSC material development.

## Section 2: Inter- and Intramolecular Conformation Control

The energy transfer and transport characteristics of conjugated polymers depend greatly on their physical conformation [22,23]. The spacing and orientation between two chromophores (or other energy transfer systems) can dictate the extent and type (long-range Forster via dipoles or short-range Dexter via diffusion/contact) of energy transfer that occurs. Similarly, energy transport within a single chromophore system is influenced by molecular planarity and packing. Because of these effects, much effort has been given to control the conformation of conjugated polymers for PSCs [18,21,24-30].

One major goal of polymer conformation control is to increase the chain planarity. Highly planar chains extend the effective conjugation length of the polymer. This improves absorption by red-shifting the band gap energy and it improves exciton and charge transport by further delocalizing electrons and excited states while reducing the population of carrier trapping sites. Strategies to increase polymer planarity have previously involved designing tight-packing, fairly crystalline materials [24,29,30]. Although the crystallinity is typically enhanced by post-processing annealing steps, design of the polymer can improve this characteristic. For instance, by controlling the regioregularity, spacing and size (length and bulkiness) of the solubilizing side chains, one can create a material with a high tendency to tightly pack and  $\pi$ - $\pi$  stack its conjugated backbone [24]. Through these methods (Figure 1.2 b) charge carrier mobilities of  $0.6 \text{ cm}^2\text{V}^{-1}\text{s}^{-1}$  have been achieved [30].

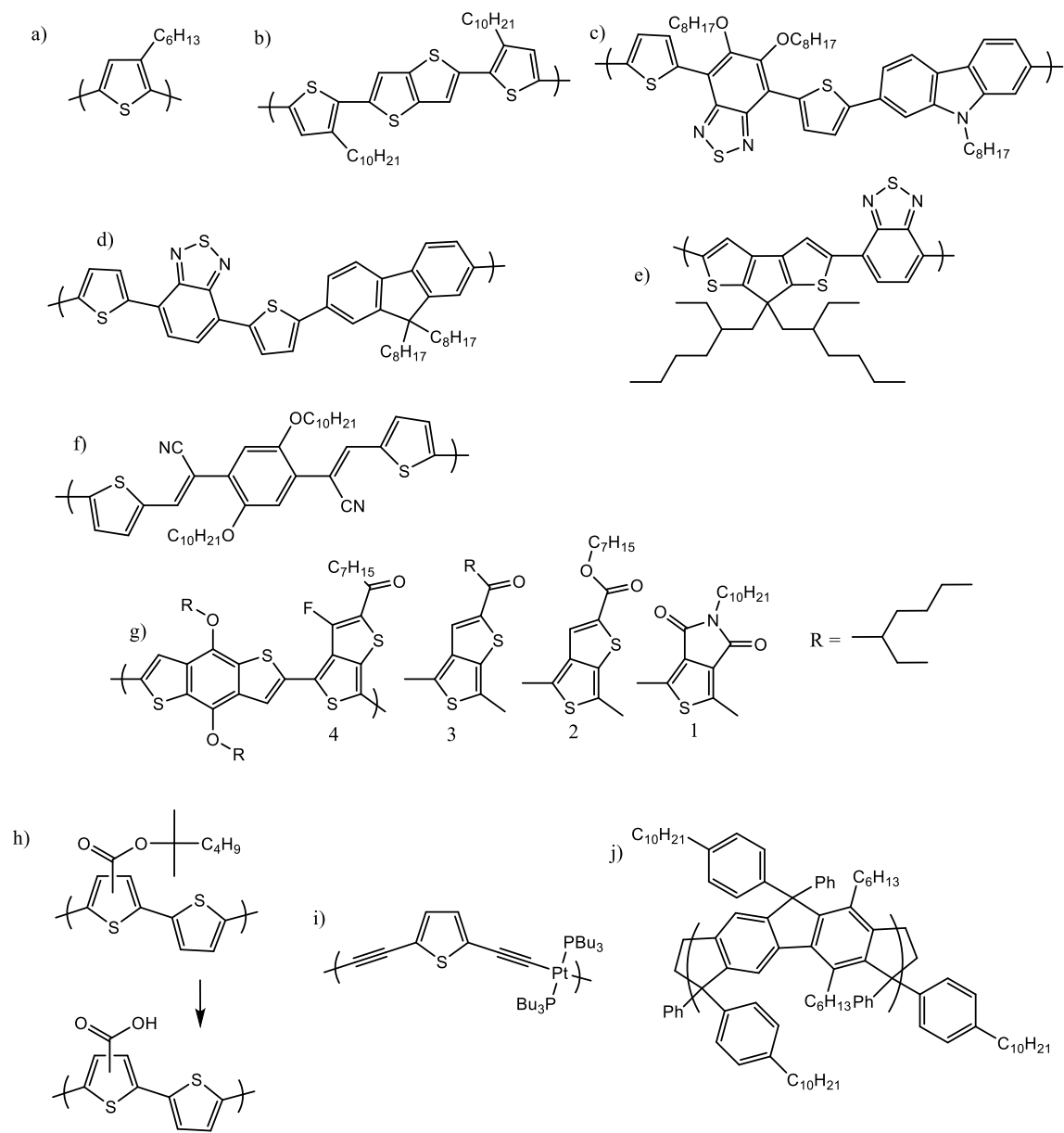


Figure 1.2: Chemical structures of interesting conjugated polymers for PSCs. a) P3HT, b) high hole mobility PBTBT exhibits a fused ring thienothiophene and control over side chain spacing and length, [30], c) by incorporating an electron donating carbazole and a withdrawing benzothiadiazole, this is a low band gap polymer [26], d) low band gap polymer exhibiting a fluorene donor and benzothiadiazole acceptor [31], e) low band gap polymer with a strong donor (cyclopentadithiophene) and benzothiadiazole as an acceptor [32], f) electron withdrawing cyano pendants lower the HOMO of this polymer [33], g) increasing the strength of electron withdrawing co-monomers (in the order 2,3,4,1) contribute to a lower HOMO in combination with electron donating benzodithiophene [34,35], h) thermally cleavable side groups allow for thermal stability of the PSC morphology [36,37], i) a novel thiophene acetylide polymer with Pt in the backbone that promotes triplet generation [38], j) a novel ladder-type poly(p-phenylene) with 120-200 ppm covalently bound Pd promotes triplet generation [39].

More recently, design of conjugated polymers with a high degree of backbone planarity has focused on the moieties in the backbone itself. Besides the aforementioned sterics of side chain interactions, bulky conjugated segments of the polymer backbone can also inhibit planarity. For instance, bonds to thiophenes are potentially more planar than bonds to benzene because the five-membered ring is physically smaller near the backbone linkage. This provides relatively less steric interference at the bond (pendant hydrogen interference), thus allowing for a planar conjugated backbone. Similarly, polymers with a zig-zag backbone structure place pendant side chains and hydrogens farther apart than polymers with a linear backbone. Alternately, some research groups are including a vinylene group along the backbone because it is very small and still maintains the conjugation [25]. These routes reduce the steric interactions between conjugated backbone structures and reduce backbone twist relative to other, more bulky moieties.

The most popular and successful route to maintain conjugated polymer planarity is to use fused ring structures along the backbone. This removes most of the flexibility from relatively larger sections of the polymer because the ring structures are much more rigid than the (conjugated) “single” bonds that are conventionally used. Even in polymers with fairly bulky side chains, the effect of the planar, fused rings comes through. Because of these effects, many researchers have incorporated moieties with two- and three-ringed structures into polymers and have achieved PSC efficiencies greater than 4% [18,21,26,27]. Finally, the two aforementioned methods which involve control of sterics are commonly implemented and balanced together with the fused ring method in order to optimize backbone planarity. Although many other routes for controlling molecular planarity exist (via secondary bonding interactions such as hydrogen bonding), these three are the primary ones used in PSCs to improve charge carrier and exciton transport [40-42].

Efficient PSCs should produce a large voltage in addition to a large current density. When characterizing a device, a potential is swept across it from the point of maximum current ( $J_{sc}$ ) to the point of no current flow ( $V_{oc}$ ). While losses in  $J_{sc}$  are primarily the result of poor transport (and can be reduced by improving polymer planarity), both  $V_{oc}$  and  $J_{sc}$  are influenced by intermolecular energy transfer. Current generation relies on efficient electron transfer from

the donor to the acceptor molecule, however the converse of this, bimolecular recombination of charge carriers at the donor-acceptor interface, is detrimental to the  $V_{oc}$  [43,44].

As stated earlier, intermolecular spacing and conformation greatly influence energy transfer, thus in an effort to reduce losses to the  $V_{oc}$  via bimolecular recombination, molecules are designed to control intermolecular spacing. For instance, in a small molecule based solar cell Perez, et al. chose donor molecules with bulky pendant groups and showed that the  $V_{oc}$  losses were decreased [44]. The bulky pendant groups increased the spacing between donor and acceptor molecules and thus reduced the level of intermolecular recombination. Similarly, many donor polymers in PSCs with high  $V_{oc}$  and low  $V_{oc}$  losses utilize long or bulky side chains like the 2-ethylhexyl group (Figure 1.2 g) [18,27,31,34,35,45-47].

As has been discussed, control over the inter- and intra-molecular conformation of electron donor polymers is of great interest in optimizing PSCs. While careful design of the molecule can lead to tuned properties, some of these design changes follow naturally from each other. For instance, since conjugated polymers are rigid, they require side chains for good solubility. When taking advantage of the enhanced planarity of fused conjugated rings, larger, bulky side chains become necessary in order to obtain sufficient solubility. Thus both the inter- and intra-molecular energy transfer and transport character will be affected. Finally, although other forms of conformation induced changes in energy transport and transfer exist (orientation, etc.) control over these through molecular design has not been explored in PSCs to the best of the authors' knowledge.

### Section 3: Electronic Band Gap and Absorption Tuning

One simple requirement for an efficient PSC is effective utilization of the solar spectrum. Absorption of light is dependent on the conjugated polymer's band gap energy; however conventional conjugated polymers usually have wide band gaps. For instance, the most widely studied polymer for PSCs, P3HT, has a band gap energy around 1.9 eV. Since more than 52% of the total solar irradiance is at energies below 1.77 eV there has been much interest in tailoring/reducing the polymer band gap to absorb more of the solar spectrum [48,49].

The primary way to increase absorption of the solar spectrum is to reduce the energy required to excite the electron donor conjugated polymer. The simplest scheme involves polymer planarity and packing: increasing the effective conjugation length can red-shift the absorption slightly (by about 0.3 to 0.6 eV) due to increased delocalization of the pi electrons [29]. This effect is primarily seen in the film state of the polymers relative to their solution state absorption, (especially in regioregular P3HT). More effective means of reducing the band gap rely on chemical tuning [50]. By alternating electron donating and electron withdrawing moieties in the conjugated polymer's structure, one can reduce the band gap (Figure 1.2 c-e, g, Figure 1.3) [51]. This push-pull structure allows for absorption transitions not only by the polymers individual moieties, but also in between them because of an appreciable difference in their energy levels (Figure 1.3 left). By setting up an internal donor-acceptor structure, the band gap is reduced to that of the intra-molecular charge transfer absorption edge [51].

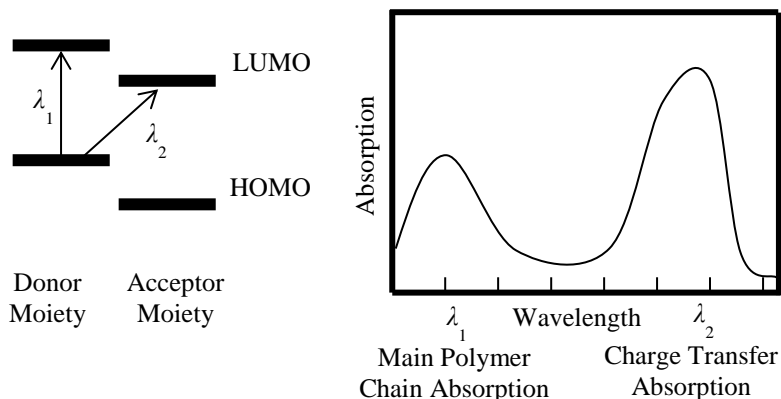


Figure 1.3: Strategies for low band gap conjugates polymers: Intramolecular charge transfer. Alternating electron donating and withdrawing moieties can result in a reduced band gap because the relatively blue absorption of the polymers main chain ( $\lambda_1$ ) is augmented by a lower energy charge transfer (between the donor and acceptor moieties,  $\lambda_2$ ) absorption.

Polymers containing alternating electron donating and electron withdrawing moieties, either along the main backbone chain or within side-chains, have tuned band gaps [17,52]. For instance, by creating a copolymer of alternating benzodithiophene and thieno[3,4-c]pyrrole-4,6-dione units (Figure 1.2 g-1) Zou, et al. were able to achieve a bandgap of about 1.8 eV [35]. Although the absorption edge is not very red-shifted relative to P3HT, the combination of the electron donating benzodithiophene and electron withdrawing thieno-pyrrole-dione units does

lower the band gap. Additionally, a band gap of about 1.4 eV can be achieved with an alternating 2,1,3-benzothiadiazole (strong acceptor) and cyclopentadithiophene (strong donor) units (Figure 1.2 e) [32]. These moieties are chosen based on the intra-molecular conformation considerations discussed earlier as well as their relative donor or acceptor strength. Increasing the strength of a donor (by raising its HOMO) or acceptor (by lowering its LUMO), all else equal, will result in a reduced band gap. Some common donor moieties include carbazole, fluorene, thiophene, and thienothiophene (in the polymers in Figure 1.2). There are also many electron withdrawing moieties (some candidates are in Figure 1.4.), but the most popular is 2,1,3-benzothiadiazole (in many polymers in Figure 1.2) (more will be presented later about energy level tuning) [53]. Thus, by varying the donating and withdrawing strength of the constituent moieties, one can achieve a wide range of band gaps.

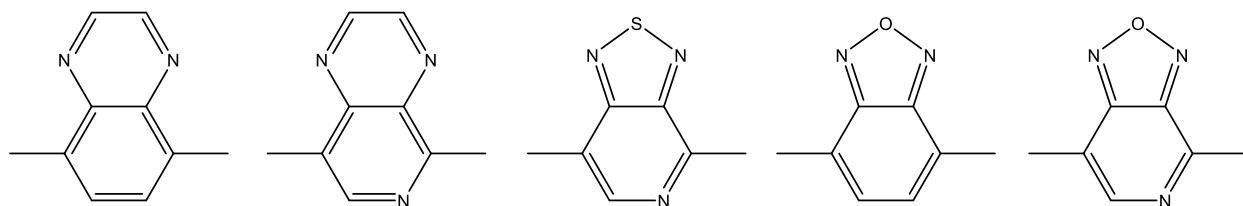


Figure 1.4: Some electron withdrawing moieties [53].

The ideal band gap energy is determined by a balance between absorption gains and conversion losses. Although a reduced band gap results in greater absorption of the available light, it also limits the ultimate level of the captured energy; an absorbed photon will relax to an energy level slightly less than the band gap of the polymer. Although a polymer could absorb 90% (70%) of the sun's irradiance with a band gap of 0.73 eV (1.24 eV), this would result in much energy loss in the conversion to useful current [48]. Therefore, in the interest of balancing these effects, an ideal band gap for donor polymers in PSCs is expected to be around 1.5 eV (with an absorption maximum around the maximum photon flux near 650-700 nm) [42,46,54].

A polymer with an appropriate band gap and a wide spectral absorbance will maximize utilization of the solar spectrum [54]. Luckily, the amorphous nature of conjugated polymer films results in a wide range of effective conjugation lengths so that a wide band of wavelengths

are absorbed. When this is combined with appropriate molecular design tailoring of the band gap, a material acceptable for efficient PSCs can be created.

#### Section 4: Tuning the Highest Occupied Molecular Orbital and Open Circuit Voltage

Efficient PSCs must produce voltages commensurate with the energy that they absorb. Absorbed energy loses potential as it relaxes and is separated in the conversion process (Figure 1.5). The maximum voltage that an organic solar cell can produce is limited by the minimum energy separation between the charges in a functioning device [55]. It has been observed that  $V_{oc}$  scales with the difference between the HOMO energy level of the donor polymer and the LUMO energy level of the acceptor molecule [34,42,56-59]. Aside from the recombination losses to  $V_{oc}$  mentioned earlier, this is a primary bottleneck for high PCE devices.

The most popular molecular design strategies for increasing  $V_{oc}$  involve increasing the donor HOMO - acceptor LUMO energy gap. By introducing pendant electron withdrawing groups or by controlling polymer planarity the HOMO level can be modulated [17,18,26,27,31,33-35,46,59-61]. Since electronegative groups pull electron density into a localized area, they bind the electrons more tightly to, and stabilize the molecule thus lowering the HOMO. By increasing the strength (electronegativity) of the withdrawing group, the HOMO can be sequentially lowered. Chen, et al. were able to progressively lower the HOMO of a poly(thienothiophene-alt-benzodithiophene) from -5.01 to -5.12 to -5.22 eV by changing the pendant groups from an ester to a ketone and finally to a fluorine and ketone pair (Figure 1.2 g 2,3,4) [34]. This resulted in an increase in PSC  $V_{oc}$  from 620 to 700 to 760 mV (note that this gain in  $V_{oc}$  is not perfectly coupled to the energy level change) [34]. Some representative electron withdrawing groups include diketone, benzothiadiazole (in the polymer backbone), ester, cyano and fluorine [17,18,26,27,31,33-35,46,60]. The inclusion of these groups has led to HOMO levels lower than -5.73 eV (Fig. 2 f), and  $V_{oc}$  values above 0.99 V [17,33]. These values are relative enhancements when compared to the HOMO (-4.9 eV) and  $V_{oc}$  (0.6 V) of the conventional material for PSCs, regioregular P3HT.

Polymer planarity and packing also play a role in determining the HOMO level. As the effective conjugation length increases in a polymer, the electrons are further delocalized and the

HOMO level is raised. For instance, Trznadel et al. showed that increasing molecular weight led to a reduction in the oxidation potential of P3HT from 0.55 to 0.45 V; this corresponds to a HOMO level increase with increasing effective conjugation length [62]. This idea has been applied to modulate or reduce the HOMO to increase  $V_{oc}$ : Li et al. has varied the length and position of alkyl and alkoxy side chains on a polymer (Figure 1.2 d) and noticed a modulation the HOMO level between -5.4 and -5.6 eV [31]. Furthermore, Hou et al. created a polythiophene with a bulky 2-hexyldecyl chain on every third monomer (as compared to the hexyl side chain on each P3HT monomer) resulting in a lowered HOMO level at -5.3 eV and an increased  $V_{oc}$  (0.82 V) [59]. While these HOMO level alterations could be attributed to changes in the population and electron donating power of the side chains, one cannot ignore the effect of side chain bulkiness; bulky side chains can reduce inter chain packing and therefore the effective conjugation length (leading to a deeper HOMO level and a higher  $V_{oc}$ ).

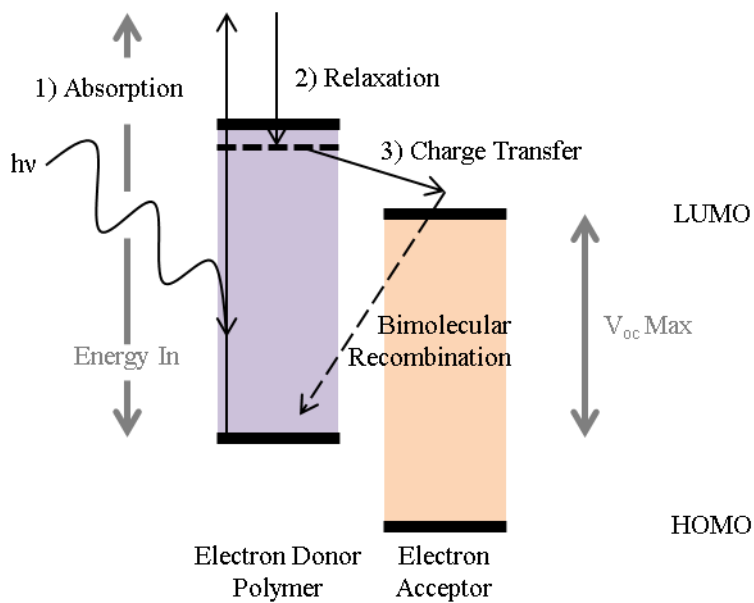


Figure 1.5: The open circuit voltage and energy conversion losses. Energy conversion losses at zero current flow contribute to lowered  $V_{oc}$ . For instance, the absorption maximum of P3HT (530 nm) has the potential to create 2.34 eV, but relaxation to just below (due to the binding energy) its 1.9 eV band gap reduces this prospective. Finally, charge transfer and bimolecular recombination losses further reduce the voltage creating capability to about 0.6 V in optimized devices.

Tuning the HOMO level of conjugated polymers has recently become the most popular method of increasing overall device efficiency [34,46]. However, much room for  $V_{oc}$  and PCE improvement remains; an absorbed photon has at least 1.7 eV (for that band gap), yet most of the donor HOMO-acceptor LUMO energy gaps fall between 0.6 to 1.4 eV, furthermore  $V_{oc}$  values are typically 0.1 to 0.3 eV lower than this [34,42,59,60]. Thus, more than half the potential voltage creating capacity of an absorbed photon is lost in the conversion process (Figure 1.5). Control over polymer packing, as mentioned earlier, and molecular orbital energy level tuning through molecular design can lead to further reductions in these losses and increases in device efficiency.

## Section 5: Stability of Polymer Solar Cells

Practical implementation of PSCs will require long device lifetimes (5-10 years at 8-16% PCE by one estimate) in order to be cost effective [63]. Although there have been reports of device lifetimes exceeding one year, there are many more reports of lifetimes closer to days or even just hours [4,7,19,37,64]. Unfortunately, there are relatively fewer publications about device lifetime enhancement (in comparison to efficiency enhancement or to understanding device physics) via molecular design, especially with regards to the polymer materials in champion efficiency devices. Nonetheless, we will briefly mention molecular design routes which can be used to enhance lifetime by combatting morphological instability and polymer degradation [4,19,36,37].

The performance of polymer solar cells is sensitive to the phase-separated morphology of the donor-acceptor blend. Due to the exciton diffusion length limitations and the necessity for percolated conduction pathways in each phase, if the phase separation is not optimized the device PCE suffers. Even when a device is fabricated with a near optimum morphology, over time the morphology may overdevelop, especially for polymers with low glass transition temperatures, leading to reduced lifetimes [37,65]. In order to combat this effect, some polymers have been designed with thermo-cleavable side chains (at the junction between an ester and a tertiary alkyl chain, Figure 1.2 h). The side chains initially impart the polymers with sufficient solubility for solution state processing. Once the polymers are cast into a film the side chains are

removed and the polymers have good thermal stability due to an increased glass transition temperature [37]. Krebs, et al. found that before cleavage, a PSC based on a polythiophene with a cleavable side chain degraded within 2 hours; the analogous device with side chains removed showed no appreciable degradation over the same time period [37]. Based on accelerated lifetime tests, they expect that a properly encapsulated device with a stable morphology would have a lifetime over 2 years [37].

Chemical degradation of conjugated polymers is a primary contributor to PSC device lifetime limitations. Studies where different encapsulation layers (which select particular ambient gasses) or different atmospheres are exposed to devices have shown that oxygen diffusion into the polymer and subsequent photo-oxidation lead to reduced device PCEs [4,5,19,36]. Energy transfer from the photo-excited polymer to oxygen can create a reactive singlet oxygen which will attack the polymer and oxidize the unsaturated backbone, thus leading to breakage of the conjugation (loss of conductivity) and device degradation [19,36]. While device encapsulation can greatly reduce these effects, molecular design can also enhance the oxidative stability of the polymers and devices [7,19,36]. The primary design route to protect against oxidation is to increase the oxidation potential of the polymer, or in other words, to reduce the HOMO level. For instance, utilizing a polymer with a low HOMO level of -5.5 eV, Kim, et al. found that no oxygen had attacked the conjugated backbone during a forty hour illumination/degradation test (whereas in P3HT Fourier-transform infrared spectroscopy indicated that oxygen had bonded to the thiophene rings) [19]. Furthermore, this enhanced oxidative stability led to slight reductions in the device degradation rate [19]. Molecular design can lower the HOMO level of the polymers as outlined in the previous section, and can therefore improve the PSC lifetime.

## Section 6: Morphology Control

Morphology control and optimization in PSCs is a critical factor in determining the PCE. Appropriate phase separation that maintains connected pathways within each phase allows for efficient exciton separation and charge conduction, both critical steps in the power conversion process. Since this is such an important design factor, many reviews have been written on this subject [1,63,66-71]. As is detailed in the reviews, most schemes for controlling the

micromorphology involve varying the polymer:PCBM mix ratio, using processing additives or appropriate solvents, or using post processing steps such as solvent vapor or thermal annealing. Less commonly, the thermodynamics of phase separation are altered via molecular design [72-74]. For example, by modifying the surface energy of P3HT (with alcohol, bromo, methyl, or pentafluoro group backbone-chain termination) to better match that of PCBM, the mixing can be improved [72]. This mixing modification resulted in an increase in fill factor from 46% to 69% and an improvement in PCE from 3.2% to 4.5% [72]. Other more audacious schemes seek to take advantage of morphological self-assembly via block copolymer physics [73-75]. However, whether using the assembly of the block copolymers directly in the device or using the assembly as a template, these methods have not achieved great success, with PCEs below 1% [73,74]. The importance of morphology in PSCs cannot be overstated; despite the previous lack of great success in molecular design of PSC blend morphology, these routes will likely continue to be explored in search of improved exciton and charge transport and improved PCE.

## Section 7: Novel Polymers for PSCs

The aforementioned polymer design rules work to reduce losses in the energy conversion processes by increasing energy gathering, improving energy transport, and by optimizing molecular energy levels. Further improvements will continue to be made through synthesis of novel polymers that take advantage of the device operation physics. For instance, there has been some interest in replacing the fullerene electron acceptor molecules with n-type conducting polymers because they absorb the solar spectrum more strongly [76-82]. In order to function as an electron acceptor, a polymer must have a LUMO and HOMO lower than those of the donor material and it must be able to conduct electrons. Polymer design strategies that assure electron accepting character involve lowering the HOMO (and accompanying LUMO) level with electron withdrawing groups similar to routes described in previous sections [77,81-83]. Although conjugated polymers have been shown to possess ambipolar conductivity, their electron mobility is typically one to three orders of magnitude smaller than their hole mobility, and is a performance limiting property [80,82,84]. Molecular design routes for improving the electron mobility are also similar to those mentioned in earlier sections; charge carrier mobility is greater in more planar polymers, and planarity can be enhanced with large, rigid, fused ring moieties

along the polymer backbone. By implementing almost comically large fused rings into the polymer backbone, the electron mobility has been enhanced to  $10^{-1}$  to  $10^{-2}$   $\text{cm}^2\text{V}^{-1}\text{s}^{-1}$  [83,85]. Despite these advancements, polymer-polymer blend solar cells are not widely popular and their PCEs are still limited to around 1.8% [82].

Another category of novel polymers for PSCs seeks to increase the exciton diffusion length by using long lived triplet excitons. As mentioned in the outset, short exciton diffusion lengths are a critical factor limiting the allowable morphologies in PSCs for effective energy conversion. Since the exciton diffusion length scales with the square root of the excitons lifetime, and since triplet excitons have lifetimes on the order of  $\mu\text{s}$ - $\text{ms}$ , there has been interest in using phosphorescent materials to enhance PSCs [38,39,86-88]. Intersystem crossing to the triplet state is a forbidden transition and special materials are required to facilitate its occurrence; molecular design routes to achieve triplet generating polymers rely on the presence of heavy metal atoms like platinum and palladium [38,39,88]. For instance, by binding trace amounts of Pd onto a ladder-type poly(para-phenylene) (Figure 1.2 j), Arif et al. were able to increase the PCE by a factor of ten (although only to 0.23%) over the same polymer without heavy metals [39,88]. They attribute the improvement to the presence of long lived ( $\tau = 8.7$  ms) triplet excitons which enhance the current density (via improved exciton separation) [39]. Similarly, by including Pt atoms in the backbone of a thiophene acetylide polymer (Figure 1.2 i), Guo et al. were able to promote the formation of a triplet state ( $\tau = 5.8$   $\mu\text{s}$ ) in PSCs that contributed to charge separation and power conversion [38]. These devices show a good proof of concept that triplet states can enhance PSCs performance; the overall efficiencies of these devices have the potential to be improved by the molecular design routes discussed in earlier sections.

These two examples show how novel molecular design is being explored to improve PSCs. By taking advantage of the understanding of PSC operational physics one can design novel materials which will pave the way for future improvements in molecular design.

## Section 8: Faux Pas in Polymer Solar Cell Design

The design of efficient PSCs is a very subtle endeavor; many of the materials' tailored properties can affect device performance in ways which are coupled or convoluted with device

fabrication. Also, ideal material and device characteristics are not well defined. For instance, in spite of the improvement which has been shown by promoting the triplet exciton state in PSCs, there is evidence that polymer triplet states act as a detrimental trap site [89,90]. Further, although PSCs are diodes and are operated under electrical bias, the role of bias in power conversion is not yet clear; there is evidence for and against the necessity of bias in separating and conducting photogenerated charge carriers [91-93]. These and other ill-defined ideal-case characteristics leave the design and fabrication of high-performance materials and devices very open to interpretation.

The length and time scales over which the important power conversion processes occur are very small (nano, pico and shorter) leading to difficulty controlling and characterizing the soft, polymeric materials and PSC devices. The BHJ morphology, for example, has proven to be a boon to making highly efficient devices, but the definition of that structure remains elusive. Although optimization of the BHJ morphology through device design has proven to yield efficient devices, characterization and control over the BHJ morphology through molecular design is quite challenging [94]. Conjugated polymers typically require aliphatic side chains which interfere with  $\pi$ - $\pi$  interactions in order to remain soluble. Since synthesis is a very laborious process, many materials are effectively given arbitrary side chains which impart only the necessary solubility for synthesis and solution processing. Unfortunately, this is a critical faux pas due to the subtle role that side chains play in controlling the morphology of a spincoated BHJ film. For instance, there are many instances in which a low band gap polymer backbone is chosen, but does not give highly efficient devices until systematic variation of the side chains is explored [95-98]. These side chain changes, although shown to help make devices perform optimally, affect so many characteristics of the film, from de-mixing with the fullerene, to energy level, absorption coefficient, charge carrier mobility, and intermolecular spacing changes, that isolating the positive effect into a universal design rule is nigh impossible.

The understanding of PSC devices is still developing and many synthetically controllable material properties have yet to be explored or discovered. Although the synthesis of new materials is a time consuming process, care must be taken in order to optimize all facets of new materials, including characterizing the effect of side chain type and placement, and film morphology development. These steps must be taken, lest a researcher may fall into a faux pas

associated with attributing a change in device performance to an underdeveloped idea associated with an under-characterized film or device.

## Section 9: Outlook

The future of PSCs is very promising due to recent advances in molecular design and device PCE. A better understanding of the operational physics of PSCs through careful characterization has created a foundation for device improvement. Each step in the energy conversion process has potential for loss, but some steps are more critical than others. Absorption of sunlight places certain demands on the band gap and thickness of the device. But efficient conversion to electricity requires optimized energy levels, morphology and exciton and charge transport. Molecular design has afforded solutions to most of these problems, namely the HOMO level has been lowered to enhance  $V_{oc}$  and the band gap has been reduced to improve absorption of sunlight. Despite the improvements in PSC lifetime and PCE, there are still device limiting material properties like exciton diffusion length and charge carrier mobility. Continuous development of the electron donor and acceptor materials (whether polymer or small molecule) will refine exciton and charge transport through tools like energy level and morphology tuning. It is also possible that novel design routes will become more successful or popular in the future. Different populations of excitons, such as triplet excitons, may be more thoroughly utilized in efficient PSCs. Or self-assembly may be utilized to control donor-acceptor phase separation and inter-and intra-molecular packing and conformation. In any case, the flexibility afforded to conjugated polymers through intelligent molecular design will allow further development of these materials to take advantage of the peculiarities of the energy conversion process. Synthesis of new polymer materials will continue to lead to improvements in understanding PSC operation and improvements in PCE.

## Section 10: References

1. W. Cai, X. Gong, Y. Cao. *Sol. Energy Mater. Sol. Cells.* 94, 114-127 (2010).
2. H. J. Park, M. G. Kang, S. H. Ahn, L. J. Guo. *Adv. Mater.* 22, E247-E253 (2010).
3. F. C. Krebs, T. Tromholt, M. Jørgensen. *Nanoscale.* 2, 873-886 (2010).
4. A. J. Medford, M. R. Lilliedal, M. Jørgensen, D. Aarø, H. Pakalski, J. Fyenbo, F. C. Krebs. *Opt. Express.* 18, A272-A285 (2010).
5. F. C. Krebs, S. A. Gevorgyan, J. Alstrup. *J. Mater. Chem.* 19, 5442-5451 (2009).
6. Best research-cell efficiencies, [http://www.nrel.gov/ncpv/images/efficiency\\_chart.jpg/](http://www.nrel.gov/ncpv/images/efficiency_chart.jpg/) (accessed February 2014 ).
7. J. A. Hauch, P. Schilinsky, S. A. Choulis, R. Childers, M. Biele, C. J. Brabec. *Sol. Energy Mater. Sol. Cells.* 92, 727-731 (2008).
8. I. W. Hwang, D. Moses, A. J. Heeger. *J. Phys. Chem. C.* 112, 4350-4354 (2008).
9. R. A. Marsh, J. M. Hodgkiss, S. Albert-Seifried, R. H. Friend. *Nano Lett.* 10, 923-930 (2010).
10. A. Pivrikas, N. S. Sariciftci, G. Juska, R. Osterbacka. *Prog. Photovoltaics Res. Appl.* 15, 677-696 (2007).
11. P. E. Shaw, A. Ruseckas, I. D. W. Samuel. *Adv. Mater.* 20, 3516-3520 (2008).
12. K. M. Coakley, M. D. McGehee. *Chem. Mater.* 16, 4533-4542 (2004).
13. G. Yu, J. Gao, J. C. Hummelen, F. Wudl, A. J. Heeger. *Science.* 270, 1789-1791 (1995).
14. Y. Li, Y. Zou. *Advanced Materials* 20, 2952-2958 (2008).
15. H. A. Becerril, N. Miyaki, M. L. Tang, R. Mondal, Y. S. Sun, A. C. Mayer, J. E. Parmer, M. D. McGehee, Z. Bao. *J. Mater. Chem.* 19, 591-593 (2009).
16. M. S. Kim, B. G. Kim, J. Kim. *ACS Appl. Mater. Interfaces.* 1, 1264-1269 (2009).
17. F. Huang, K. S. Chen, H. L. Yip, S. K. Hau, O. Acton, Y. Zhang, J. Luo, A. K. Y. Jen. *J. Am. Chem. Soc.* 131, 13886-13887.
18. L. Huo, J. Hou, S. Zhang, H. Y. Chen, Y. Yang. *Angew. Chem. Int. Ed.* 122, 1542-1545 (2010).
19. S. H. Kim, I. W. Hwang, Y. Jin, S. Song, J. Moon, H. Suh, K. Lee. *Sol. Energy Mater. Sol. Cells.* (2010), doi:10.1016/j.solmat.2009.12.013.
20. Y. Li, Y. Zou, *Adv. Mater.* 20, 2952-2958 (2008).
21. Y. Liang, Y. Wu, D. Feng, S. T. Tsai, H. J. Son, G. Li, L. Yu. *J. Am. Chem. Soc.* 131, 56-57 (2009).
22. B. J. Schwartz. *Annu. Rev. Phys. Chem.* 54, 141-172 (2003).
23. J. Lee, H. J. Kim, T. Chen, K. Lee, K. S. Kim, S. C. Glotzer, J. Kim, N. A. Kotov. *J. Phys. Chem. C.* 113, 109-116 (2009).
24. Y. Kim, S. Cook, S. Tuladhar, S. A. Choulis, J. Nelson, J. R. Durrant, D. C. Bradley, M. Giles, I. McCulloch, C. S. Ha, M. Ree. *Nat. Mater.* 5, 197-203 (2006).
25. B. Lim, K. J. Baeg, H. G. Jeong, J. Jo, H. Kim, J.-Woo Park, Y. Y. Noh, D. Vak, J. H. Park, J.-Woong Park, D. Y. Kim. *Adv. Mater.* 21, 1-7 (2009).

26. R. Qin, W. Li, C. Li, C. Du, C. Veit, H. F. Schleiermacher, M. Andersson, Z. Bo, Z. Liu, O. Inganas, U. Wuerfel, F. Zhang. *J. Am. Chem. Soc.* 131, 14612-14613 (2009).
27. S. Xiao, A. C. Stuart, S. Liu, W. You. *ACS Appl. Mater. Interfaces.* 1, 1613-1621 (2009).
28. C. Y. Yu, B. T. Ko, C. Ting, C. P. Chen. *Sol. Energy Mater. Sol. Cells.* 93, 6113-620 (2009).
29. P. J. Brown, D. S. Thomas, A. Kohler, J. S. Wilson, J. S. Kim, C. M. Ramsdale, H. Sirringhaus, R. H. Friend. *Phys. Rev. B.* 67, 064203 (2003).
30. I. McCulloch, M. Heeney, C. Bailer, K. Genevicius, I. MacDonald, M. Shkunov, D. Sparrowe, S. Tierney, R. Wagner, W. Zhang, M. L. Chabinyc, R. J. Kline, M. D. McGehee, M. F. Toney. *Nat. Mater.* 5, 328-333 (2006).
31. W. Li, R. Qin, Y. Zhou, M. Andersson, F. Li, C. Zhang, B. Li, Z. Bo, F. Zhang. *Polymer* 51, 3031-3038 (2010).
32. D. Mühlbacher, M. Scharber, M. Morana, Z. Zhu, D. Waller, R. Gaudiana, C. Brabec. *Adv. Mater.* 18, 2884-2889 (2006).
33. K. Colladet, S. Fourier, T. J. Cleij, L. Lutsen, J. Gelan, D. Vanderzande, L. H. Nguyen, H. Neugebauer, S. Sariciftci, A. Aguirre, G. Janssen, E. Goovaerts. *Macromolecules.* 40, 65-72 (2007).
34. H. Y. Chen, J. Kou, S. Zhang, Y. Liang, G. Yang, Y. Yang, L. Yu, Y. Wu, G. Li. *Nat. Photonics.* 3, 649-653 (2009).
35. Y. Zou, A. Najari, P. Berrouard, S. Beaupré, B. R. Aïch, Y. Tao, M. Leclerc. *J. Am. Chem. Soc.* 132, 5330-5331 (2010).
36. M. Jørgensen, K. Norrman, F. C. Krebs. *Sol. Energy Mater. Sol. Cells.* 92, 686-714 (2008).
37. F. C. Krebs, H. Spanggard. *Chem. Mater.* 17, 5235-5237 (2005).
38. F. Guo, Y. G. Kim, J. R. Reynolds, K. S. Schanze. *Chem. Commun.* 17, 1887-1889 (2006).
39. M. Arif, K. Yang, L. Li, P. Yu, S. Guha, S. Gangopadhyay, M. Forster, U. Scherf. *Appl. Phys. Lett.* 94, 063307 (2009).
40. O. Bolton, J. Kim. *J. Mater. Chem.* 17, 1981-1988 (2007).
41. Z. Zhu, D. Mühlbacher, M. Morana, M. Koppe, M. C. Scharber, D. Waller, G. Dennler, C. J. Brabec. In *High-Efficient Low-Cost Photovoltaics*, Vol. 140, pp. 195-222, Springer, Berlin/Heidelberg (2009).
42. M. C. Scharber, D. Mühlbacher, M. Koppe, P. Denk, C. Waldauf, A. J. Heeger, C. J. Brabec. *Adv. Mater.* 18, 789-794 (2006).
43. K. Vandewal, K. Tvingstedt, A. Gadisa, O. Inganas, J. V. Manca. *Nat. Mater.* 8, 904-909 (2009).
44. M. D. Perez, C. Borek, S. R. Forrest, M. E. Thompson. *J. Am. Chem. Soc.* 131, 9281-9286.
45. Y. Zhang, S. K. Hau, H. L. Yip, Y. Sun, O. Acton, A. K. Y. Jen. *Chem. Mater.* 22, 2696-2698 (2010).

46. Y. Liang, Z. Xu, J. Xia, S. T. Tsai, Y. Wu, G. Li, C. Ray, L. Yu. *Adv. Mater.* 22, E135-E138 (2010).
47. M. Svensson, F. Zhang, S. C. Veenstra, W. J. H. Verhees, J. C. Hummelen, J. M. Kroon, O. Inganäs, M. R. Andersson. *Adv. Mater.* 15, 988-991 (2003).
48. C. A. Gueymard. *Sol. Energy.* 76, 423-453 (2004).
49. C. Winder, N. S. Sariciftci. *J. Mater. Chem.* 14, 1077-1086 (2004).
50. J. Roncali. *Chem. Rev.* 97, 173-205 (1997).
51. E. E. Havinga, W. Hoeve, H. Wynberg. *Polym. Bull.* 29, 119-126 (1992).
52. H. Zhou, L. Yang, S. Stoneking, W. You. *ACS Appl. Mater. Interfaces.* 2, 1377-1383 (2010).
53. N. Blouin, A. Michaud, D. Gendron, S. Wakim, E. Blair, R. Neagu-Plesu, M. Belletête, G. Durocher, Y. Tao, M. Leclerc. *J. Am. Chem. Soc.* 130, 732-742 (2008).
54. F. Shi, G. Fang, F. Liang, L. Wang, Z. Mu, X. Zhang, Z. Xie, Z. Su. *Eur. Polym. J.* 46, 1770-1777 (2010).
55. B. P. Rand, D. P. Burk, S. R. Forrest. *Phys. Rev. B.* 75, 115327 (2007).
56. A. Gadisa, M. Svensson, M. R. Andersson, O. Inganäs. *Appl. Phys. Lett.* 84, 1609-1611 (2004).
57. T. Yamanari, T. Taima, J. Sakai, K. Saito. *Sol. Energy Mater. Sol. Cells.* 93, 759-761 (2009).
58. V. D. Mihailetschi, P. W. M. Blom, J. C. Hummelen, M. T. Rispen. *J. App. Phys.* 94, 6849-6854 (2003).
59. J. Hou, T. L. Chen, S. Zhang, L. Huo, S. Sista, Y. Yang. *Macromolecules.* 42, 9217-9219 (2009).
60. S. Berson, S. Cecioni, M. Billon, Y. Kervella, R. de Bettignies, S. Bailly, S. Guillerez. *Sol. Energy Mater. Sol. Cells.* 94, 699-708 (2010).
61. E. Wang, L. Wang, L. LAn, C. Luo, W. Zhuang, J. Peng, Y. Cao. *Appl. Phys. Lett.* 92, 033307 (2008).
62. M. Trznadel, A. Pron, M. Zagorska, R. Chrzaszcz, J. Pielichowski. *Macromolecules.* 31, 5051-5058 (1998).
63. G. Dennler, M. C. Scharber, C. J. Brabec. *Adv. Mater.* 21, 1-16 (2009).
64. S. H. Park, A. Roy, S. Beaupré, S. Cho, N. Coates, J. S. Moon, D. Moses, M. Leclerc, K. Lee, A. J. Heeger. *Nat. Photonics.* 3, 297-303 (2009).
65. X. Yang, J. K. J. van Duren, R. A. J. Janssen, M. A. J. Michels, J. Loos. *Macromolecules.* 37, 2151-2158 (2004).
66. H. Hoppe, N. S. Sariciftci. *J. Mater. Chem.* 45, 45-61 (2006).
67. A. C. Mayer, S. R. Scully, B. E. Hardin, M. W. Rowell, M. D. McGehee. *Mater. Today.* 10, 28-33 (2007).
68. S. Günes, H. Neugebauer, N. S. Sariciftci. *Chem. Rev.* 107, 1324-1338 (2007).
69. R. Giridharagopal, D. S. Ginger. *J. Phys. Chem. Lett.* 1, 1160-1169 (2010).
70. X. Yang, J. Loos. *Macromolecules.* 40, 1353-1362 (2007).

71. L. Chen, Z. Hong, G. Li, Y. Yang. *Adv. Mater.* 21, 1434-1449 (2009).
72. J. S. Kim, Y. Lee, J. H. Lee, J. H. Park, J. K. Kim, K. Cho. *Adv. Mater.* 22, 1355-1360 (2010).
73. S. S. Sun, C. Zhang, A. Ledbetter, S. Choi, K. Seo, C. E. Bonner, M. Drees, N. S. Sariciftci. *Appl. Phys. Lett.* 90, 043117 (2007).
74. R. Q. Png, P. J. Chia, J. C. Tang, B. Liu, S. Sivaramakrishnan, M. Zhou, S. H. Khong, H. S. O. Chan, J. H. Burroughes, L. L. Chua, R. H. Friend, P. K. H. Ho. *Nat. Mater.* 9, 152-158 (2010).
75. F. S. Bates, G. H. Fredrickson. *Phys. Today.* 52, 32-38 (1999).
76. S. A. Jenekhe, S. Yi, *Appl. Phys. Lett.* 77, 2635-2637 (2000).
77. M. M. Mandoc, W. Veurman, J. Sweelssen, M. M. Koetse, P. W. M. Blom. *Appl. Phys. Lett.* 91, 073518 (2007).
78. C. R. McNeill, N. C. Greenham, *Adv. Mater.* 21, 3840-3850 (2009).
79. M. M. Koetse, J. Sweelssen, K. T. Hoekerd, H. F. M. Schoo, S. C. Veenstra, J. M. Kroon, X. Yang, J. Loos. *Appl. Phys. Lett.* 88, 083504 (2006).
80. C. R. McNeill, A. Abrusci, J. Zaumseil, R. Wilson, M. J. McKiernan, J. H. Burroughes, J. J. M. Halls, N. C. Greenham, R. H. Friend. *Appl. Phys. Lett.* 90, 193506 (2007).
81. C. R. McNeill, J. J. M. Halls, R. Wilson, G. L. Whiting, S. Berkebile, M. G. Ramsey, R. H. Friend, N. C. Greenham. *Adv. Funct. Mater.* 18, 2309-2321 (2008).
82. S. C. Veenstra, J. Loos, J. M. Kroon. *Prog. Photovoltaics Res. Appl.* 15, 727-740 (2007).
83. X. Zhan, Z. Tan, B. Domercq, Z. An, X. Zhang, S. Barlow, Y. Li, D. Zhu, B. Kippelen, S. R. Marder. *J. Am. Chem. Soc.* 129, 7246-7247 (2007).
84. R. Steyrlleuthner, S. Bange, D. Neher. *J. App. Phys.* 105, 064509 (2009).
85. H. Yan, Z. Chen, Y. Zhang, C. Newman, J. R. Quinn, F. Dotz, M. Kastler, A. Facchetti. *Nature.* 457, 679-686 (2009).
86. B. P. Rand, S. Schols, D. Cheyns, H. Gommans, C. Girotto, J. Genoe, P. Heremans, J. Poortmans. *Org. Electron.* 10, 1015-1019 (2009).
87. B. P. Rand, C. Girotto, A. Mityashin, A. Hadipour, J. Genoe, P. Heremans. *Appl. Phys. Lett.* 95, 173304 (2009).
88. K. Yang, M. Arif, M. Forster, U. Scherf, S. Guha. *Synth. Met.* 159, 2338-2341 (2009).
89. Y. Zhang, B. Gautam, T. Basel, D. Mascaro, Z. Vardeny. *Synth. Met.* 173, 2-9 (2013).
90. A. Rao, P. Chow, S. Gelinas, C. Schlenker, C.-Z. Li, H.-L. Yip, A. Jen, D. Ginger, R. Friend. *Nat. Lett.* 500, 435-440 (2013).
91. N. Giebink, G. Wiederrecht, M. Wasielewski, S. Forrest. *Phys. Rev. B.* 82, 155305 (2010).
92. D. Vithanage, A. Devizis, V. Abramavicius, Y. Infahsaeng, D. Abramavicius, R. MacKenzie, P. Keivanidis, A. Yartsev, D. Hertel, J. Nelson, V. Sundstrom, V. Gulbinas. *Nat. Comm.* 4, 1-6 (2013).

93. K. Vandewal, S. Albrecht, E. Hoke, K. Graham, J. Widmer, J. Douglas, M. Schubert, W. Mateker, J. Bloking, G. Burkhard, A. Sellinger, J. Frechet, A. Amassian, M. Riede, M. McGehee, D. Neher, A. Salleo. *Nat. Mater.* 13, 63-68 (2014).
94. X. Guo, N. Zhou, S. Lou, J. Smith, D. Tice, J. Hennek, R. Ortiz, J. Navarrete, S. Li, J. Strzalka, L. Chen, R. Chang, A. Facchetti, T. Marks. *Nat. Photonics.* 7, 825-833 (2013).
95. L. Yang, H. Zhou, W. You. *J. Phys. Chem. C.* 114, 16793-16800 (2010).
96. I. Meager, R. Ashraf, S. Mollinger, B. Schroeder, H. Bronstein, D. Beatrup, M. Vezie, T. Kirchartz, A. Salleo, J. Nelson, I. McCulloch. *J. Am. Chem. Soc.* 135 (31), 11537-11540 (2013).
97. Y. Li, J. Zhou, H. Yip, C. Li, Y. Zhang, C. Chueh, J. Intemann, Y. Xu, P. Liang, Y. Chen, A. Jen. *Macromolecules.* 46 (14), 5497-5503 (2013).
98. L. Dou, C. Chen, K. Yoshimura, K. Ohya, W. Chang, J. Gao, Y. Liu, E. Richard, Y. Yang. *Macromolecules.* 46, 3384-3390 (2013).
99. D. Bilby, B.-G. Kim, J. Kim, *Pure Appl. Chem.* 83, [1], 127 (2011).

## Chapter 2: Loss to the open circuit voltage and structure at the donor-acceptor interface

*Forenote: Much of the following text is used, with permission, from Bilby, et al., Appl. Phys. Lett. 103 203902 (2013).*

Organic photovoltaic (OPV) cells carry the promise of inexpensive renewable energy due to the potential for high throughput, roll-to-roll manufacturing [1-3]. Unfortunately, the low power conversion efficiency of these devices is a critical barrier which must be overcome before they can be widely adopted. Thus the development of novel materials, and design principles for making these materials, for highly efficient OPV cells is of premier importance [4-6]. Although the operating physics of these devices are slowly being elucidated, application of these ideas to performance enhancing molecular design is not yet clear [7-11].

Often falling short of its theoretical maximum value, the open circuit voltage ( $V_{oc}$ ) would benefit greatly from improved molecular design principles. This voltage has been described by many to be a function of the energy difference between the highest occupied molecular orbital (HOMO) of the electron donor and the lowest unoccupied molecular orbital (LUMO) of the electron acceptor [12-18]. More specifically, the  $V_{oc}$  is thought to be reduced in practical devices by a polaron pair binding energy and by polaron pair recombination at the donor-acceptor interface [7,19-23].

A statement of the relationship between material properties and the  $V_{oc}$  is a catalyst for the nascence of new design strategies. The simplest design parameter for improving the  $V_{oc}$  has been to tailor the active materials' energy levels [24-29]. However, this strategy is quickly curtailed by the energy level requirements for charge transfer and sunlight absorption. Alternative strategies involve changing a spatial property of the material (usually the length, location or bulkiness of molecular side groups) and observing a non-energy level related influence on the  $V_{oc}$  [30-35]. These studies are consistent with the idea that sterics may reduce the electronic interaction, and thus geminate polaron pair recombination, between molecules at

the donor-acceptor interface. While these results are promising, bulk material changes (and in some cases bulk heterojunction morphologies) in OPV cells do not provide clear insight into the influence of molecular design changes at the donor-acceptor interface on loss to the  $V_{oc}$ ; bulk material changes cannot precisely decouple effects from changes in absorption, mobility, or morphology from the changes in  $V_{oc}$  [35-38].

A straightforward investigation of the influence of material design on loss to the  $V_{oc}$  can be achieved by controlling the local molecular structure of the donor-acceptor interface in a planar heterojunction OPV. Indeed, many variations on this idea have been explored [39-49]. These experiments typically vary the effective energy of the geminate polaron pair via generation of a dipole or via introduction of a deep-HOMO spacer at the donor-acceptor interface. While some of these studies discuss how their interfacial change has influenced  $V_{oc}$  loss, most are difficult to apply as a concrete design principle which can be applied to a bulk material. Interchangeably, these studies do not de-convolute the dipole, absorption and spacing effects of their interlayer from the reduction in  $V_{oc}$  loss.

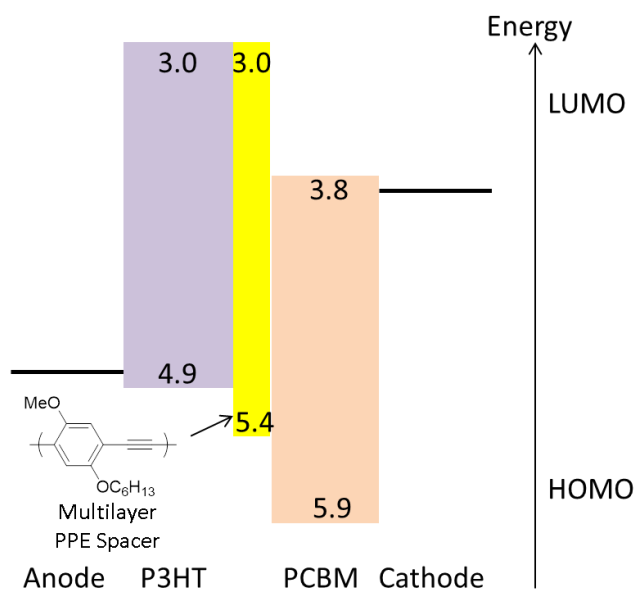


Figure 2.1: The energy levels (in eV) of the device stack show that an interlayer spacer can interfere with charge transport in a planar heterojunction OPV.

In this letter, we place interfacial layers in a polymer solar cell and increase  $V_{oc}$  by incrementally modifying the polaron energy and the dark diode current. As portrayed in Figure 2.1, we insert, via Langmuir Schaefer lifting, a controlled number of multilayers of a conjugated spacer into the donor-acceptor interface of a planar heterojunction OPV. The excellent molecular assembly control afforded by this technique allows us to distinguish the effects of spacing from the effects of energy level and absorption change.

## Section 2: Materials and synthesis

All materials are used as purchased. Poly (3-hexylthiophene) (P3HT), P100, is purchased from Rieke Metals, Phenyl C<sub>61</sub>- butyric acid methyl ester (PCBM), ADS61BFA, is purchased from American Dye Source, ITO-coated glass, CG-50IN-S107, is purchased from Delta technologies, Ltd., Poly(ethyleneimine) (PEI), 181978, is purchased from Sigma Aldrich, as are MoO<sub>3</sub> and the constituent materials for the Poly(phenylene ethynylene) (PPE) spacer, as depicted in Figure 2.2. Silver pellets are purchased from Kurt J. Lesker.

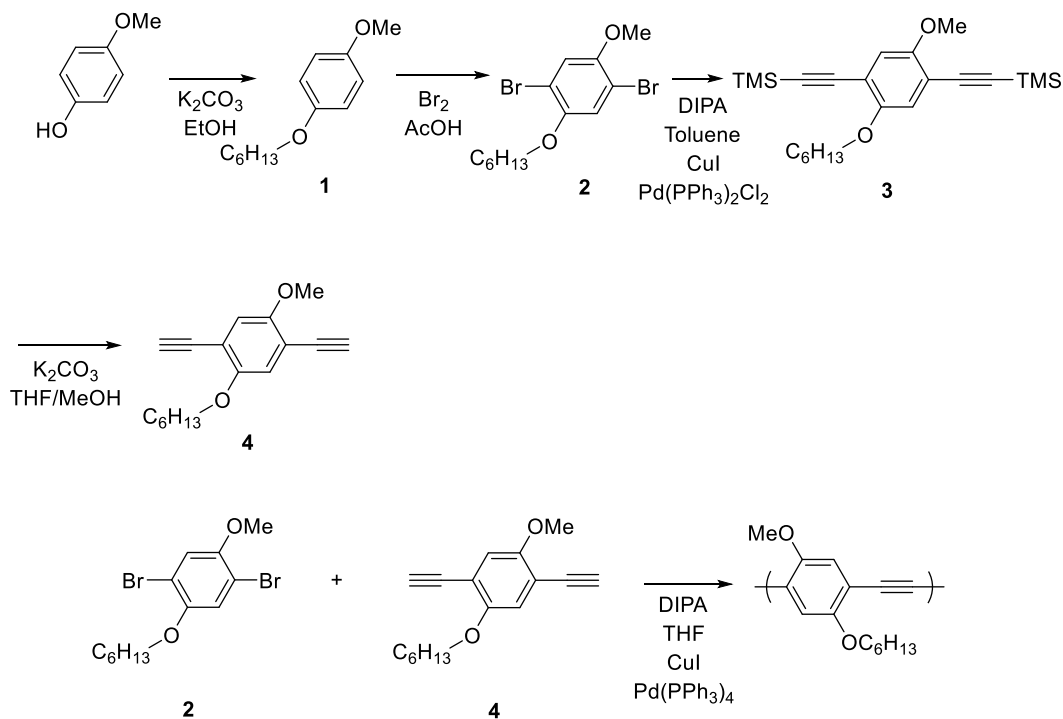


Figure 2.2: The synthetic route for producing the PPE spacer material.

**p-hexyloxyanisole (1):** 1-bromohexane (13.57 mL, 1.2 eq.) was added to p-methoxyphenol (10 g) and potassium carbonate (16.7 g, 1.5 eq.) in 100 mL ethanol under reflux. The mixture was stirred overnight, and then poured into water, extracted with diethyl ether and purified by column chromatography with 10% ethyl acetate in hexanes to get 14.8 g of **1** (99%). <sup>1</sup>H NMR (400 MHz, CDCl<sub>3</sub>, 25 °C): δ =0.82 (t, 3 H, CH<sub>3</sub>), 1.2-1.5 (m, 6 H, CH<sub>2</sub>), 1.75 (m, 2 H, CH<sub>2</sub>), 3.74 (s, 3 H, OCH<sub>3</sub>), 3.85 (t, 2 H, OCH<sub>2</sub>), 6.80 (s, 4 H, 2-H, 2'-H, 3-H, 3'-H).

**2,5-dibromo-4-hexyloxyanisole (2):** Bromine (1.35 mL, 2.2 eq.) is added drop-wise to p-hexyloxyanisole (2.5 g) in glacial acetic acid at 65° with a reflux condenser. The reaction is stirred for 45 minutes before refluxing for 1 hour. After cooling, the excess bromine is killed with a water solution of sodium sulfite (until the reaction color changes to clear). The reaction is then poured into water and the organic material is extracted with hexanes. The material is purified with column chromatography in hexanes to give 1.95 g (44%). <sup>1</sup>H NMR (400 MHz, CDCl<sub>3</sub>, 25 °C): δ =0.82 (t, 3 H, CH<sub>3</sub>), 1.2-1.6 (m, 6 H, CH<sub>2</sub>), 1.8 (m, 2 H, CH<sub>2</sub>), 3.82 (s, 3 H, OCH<sub>3</sub>), 3.92 (t, 2 H, OCH<sub>2</sub>), 7.07 (s, 2 H, 3-H, 6-H). We later found that the route given in Wang, et al., Polymer, **51** (2010) 75 gives better yields.

**2,5-di(trimethylsilyl)ethynyl-4-hexyloxyanisole (3):** 2,5-dibromo-4-hexyloxyanisole (1g), copper iodide (41.6 mg, 0.08 eq.), and PdCl<sub>2</sub>(PPh<sub>3</sub>)<sub>2</sub> (153 mg, 0.08 eq.) are stirred at 65° in a 20 mL of a 1:1 mix of diisopropylamine:toluene. Trimethylsilylacetylene (0.89 mL, 2.1 eq.) is added drop-wise to the mixture. The reaction is stirred for 16 hours, while monitoring by TLC (product gives a distinct blue emission on thin layer chromatography under 254 nm irradiation) and adding TMS-acetylene as needed, before cooling, filtering off precipitate and drying under vacuum. The material is purified with column chromatography with 5% EA in hexanes to give 1.04 g (95%). <sup>1</sup>H NMR (400 MHz, CDCl<sub>3</sub>, 25 °C): δ =0.23 (s, 18 H, TMS), 0.88 (t, 3 H, CH<sub>3</sub>), 1.31 (m, 4 H, CH<sub>2</sub>), 1.53 (m, 2 H, CH<sub>2</sub>), 1.76 (m, 2 H, CH<sub>2</sub>), 3.8 (s, 3 H, OCH<sub>3</sub>), 3.92 (t, 2 H, OCH<sub>2</sub>), 6.86, 6.88 (s, 2 H, 3-H, 6-H).

**2,5-diethynyl-4-hexyloxyanisole (4):** **(3)** (1.04g) is added to 17 mL of a 7:10 mix of methanol:tetrahydrofuran. Potassium carbonate (759 mg, 2.2 eq) is added and the reaction is stirred at room temperature for overnight. The reaction is then poured into water, extracted with

diethyl ether and dried en vacuo. The material is then purified via column chromatography with 5% EA in hexanes to give 473 mg (75%) of the desired product.  $^1\text{H}$  NMR (400 MHz,  $\text{CDCl}_3$ , 25  $^\circ\text{C}$ ):  $\delta$  = 0.88 (t, 3 H,  $\text{CH}_3$ ), 1.31 (m, 4 H,  $\text{CH}_2$ ), 1.44 (m, 2 H,  $\text{CH}_2$ ), 1.78 (m, 2 H,  $\text{CH}_2$ ), 3.32 (s, 1H,  $\text{C}\equiv\text{H}$ ), 3.36 (s, 1 H,  $\text{C}\equiv\text{H}$ ), 3.83 (s, 3 H,  $\text{OCH}_3$ ), 3.95 (t, 2 H,  $\text{OCH}_2$ ), 6.94 (2 s, 2 H, 3-H, 6-H).

**Poly(2-methoxy-5-hexyloxyphenylene ethynylene) (PPE)** : A conventional Sonogashira coupling polymerization reaction is used to create the PPE. In a glove box, 2,5-diethynyl-4-hexyloxyanisole (100 mg, 1 eq.) is added to a mixture of 2,5-dibromo-4-hexyloxyanisole (142.8 mg), copper iodide (5.9 mg, 0.08 eq.), and  $\text{Pd}(\text{PPh}_3)_4$  (36.1 mg, 0.08 eq.) with 12 mL of a 1:1 mix of diisopropylamine:tetrahydrofuran in a sealable schlenk flask. At 65  $^\circ\text{C}$  the reaction is then stirred for 12 hours under these near-reflux conditions. Finally, the reaction is cooled, then the solvent is removed with a rotary evaporator before re-dissolving into a THF/water/HCl mix and stirring for 30 minutes. The material is extracted with chloroform, filtered, then further purified with soxhlet extraction to give 24 mg of the desired polymer. GPC in chloroform using polystyrene standards revealed that the number average molecular weight is about 6 kDa with a PDI of 1.37. The molecular weight is not expected to affect film forming capability.

### Section 3: Characterization methods

Photovoltaic devices are characterized with an HP/Agilent semiconductor parameter analyzer while being illuminated with simulated AM 1.5G, 1 sun light from a Newport solar simulator. The device current is normalized to the electrode mask size.

External quantum efficiency measurements are taken on a custom setup using coupled light from a metal-halide lamp and a halogen lamp passed through an Oriel 1/8m monochromator. This light is then collimated to within 1 degree divergence and the sample is illuminated at normal incidence. The light was chopped with an optical chopper at 185 Hz and the photocurrent signal was measured using a Stanford Research Systems lock-in amplifier and compared to a calibrated silicon reference cell.

The light intensity and temperature dependent measurements are taken in a VPF100 cryostat from Janis (~1 mTorr) under illumination from a continuous diode-pump solid state laser (DL405-010 from Crystalaser) at 405 nm, 495 mW. The light intensity is varied with neutral density filters having optical densities between 0.1 and 3.

Cyclic voltammetry is measured with a CH instruments CHI600C potentiostat using 0.1 M tetrabutylammonium hexafluorophosphate in acetonitrile as the working electrolyte, silver nitrate as the reference electrode, and Pt wire as the counter electrode. The scans are taken at either 0.01 V/s or 0.1 V/s scan rates and are shifted using the onset of ferrocene oxidation (-4.80 eV). The working electrode is either glassy carbon or ITO, and HOMO and LUMO values are calculated using the onset of reduction or oxidation.

Absorption of the polymer films is measured using transmission mode in a Varian Cary 50 spectrometer. The quality of the monolayer films is observed macroscopically with an Olympus BX-51 fluorescence/optical microscope.

#### Section 4: Monolayer formation and material energy level characterization

Langmuir monolayers have been shown to provide excellent control, at the molecular level, of the conformation and interaction between polymeric materials [50]. This technique was adopted in order to exercise precise control over the molecular structure and orientation local to the donor-acceptor interface in an OSC, in this case by inserting layers of PPE. The PPE that we have chosen (structure in Figure 2.1) has a fair affinity for self-assembly at the air-water interface due to the relative difference in hydrophobicity of its methoxy and hexyloxy side chains. When PPE is spread at the air-water interface, it is compressible and shows pressure-area isotherms indicative of monolayer formation, as shown in Figure 2.3. When transferred onto a glass substrate this monolayer absorbs a small amount of light and is mostly surface covering, indicated by fluorescence microscopy (Figure 2.3), with pinholes of about 2-5 microns in diameter. These pinholes do not appear to drastically affect the character of the solar cell devices.

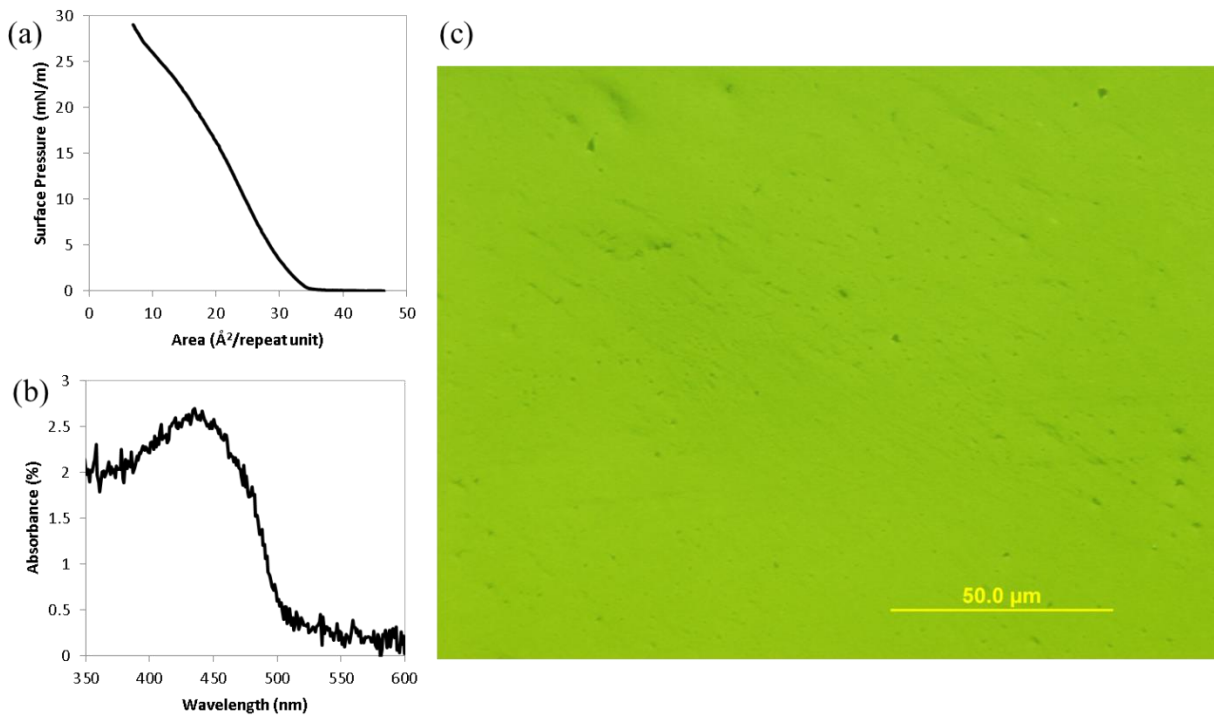


Figure 2.3: (a) The pressure-area isotherm for PPE shows compressibility and an area per repeat unit consistent with monolayer formation. (b) Langmuir-Schaefer lifting of the compressed monolayer at 15 mN/m creates a film with less than 3% absorption, again consistent with monolayer formation. (c) Luminescence microscope images indicate that the transferred monolayer is surface covering.

Films made of ten layers of the PPE spacer are measured to be  $7.90 \pm 0.52$  nm thick by AFM, giving an average of 0.79 nm per layer. Moreover, synthetic variation of the alkoxy length provides sub-nanometer control over the monolayer thickness. We synthesized a series of PPEs (just as above, but with different linear alkyl lengths in place of the hexyl chain) with varying alkyl lengths of 4, 6, 8, 10, 12, and 16 carbons in length. Although the PPE with a 4 carbon-length side chain aggregated at the air water interface (and didn't make fully surface-covering films), the rest of the PPEs made good, surface-covering films. After depositing 10 monolayers onto glass, AFM measurements indicated that each PPE creates a different spacing (Figure 2.4).

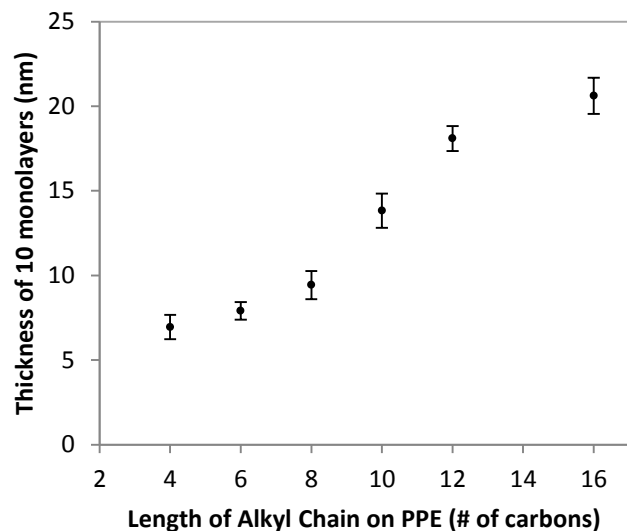


Figure 2.4: AFM measurements of ten monolayers of each PPE (deposited at 15 mN/m) show that the change in side chain length influences the film thickness.

Cyclic voltammetry is used to estimate the energy levels of the materials used in the photovoltaic devices, as shown in Figure 2.5. Note that there is a junk peak around -1.2 V; we know that this is a junk peak because it persists when the sample is removed (also when electrolyte and reference electrodes are refreshed) and because its intensity does not change depending on the amount of sample present.

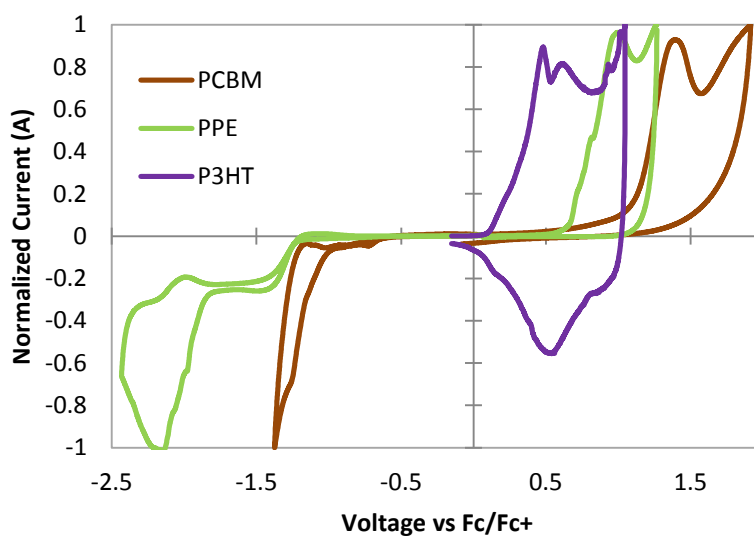


Figure 2.5: Cyclic voltammetry scans of the materials used in our devices.

The energy levels of the bulk PPE, as determined by cyclic voltammetry of dropcast samples, show that the HOMO and LUMO are about -5.4 eV and -3.0 eV. These values should provide a stepwise hole transfer from PCBM (HOMO: -5.9 eV, LUMO: -3.8 eV) to P3HT (HOMO: -4.9 eV, LUMO -3.0 eV from bandgap) but should block electron transfer from P3HT to PCBM. Accordingly, these surface covering PPE films should provide controllable spacing between P3HT and PCBM while interfering with electron transfer between them.

## Section 5: Device fabrication

Planar heterojunction polymer solar cells, with a structure of ITO/PEI(29 nm)/PCBM(85 nm)/spacer/P3HT(65 nm)/MoO<sub>3</sub>(10 nm)/Ag are fabricated using a contact film transfer technique [49]. ITO glass is sonicated in isopropanol and then acetone each for 10 minutes, followed by a 10 minute UV-ozone treatment. Next, PEI is spincoated in a nitrogen filled glove box from a 0.4 wt% in 2-methoxyethanol solution at 2000 rpm for 1 minute, accelerating at 1000 rpm/s to modify the electrode's work function [51]. After a 10 minute anneal at 100 °C, PCBM is spincoated from a 30 mg/mL chlorobenzene solution (filtered through 0.45 micron PTFE) at 1000 rpm for 1 minute and then annealed at 150 °C for 15 minutes. Then, a PPE multilayer spacer is deposited using Langmuir Schaefer lifting from a monolayer spread on an air-water interface at a surface pressure of 15 mN/m. Between each layer, the water drop that sticks to the film is dried off carefully using a lab tissue. A P3HT film is then transferred onto the stack from a sacrificial PSS/glass substrate (cleaned, UV-O treated glass with 10 wt% PSS in water spincoated at 4000 rpm for 30s; P3HT is spincoated next at 1000 rpm for 30 s from an 8.24 mg/mL solution, filtered through 0.45 micron PTFE, in chlorobenzene). The PCBM/spacer and P3HT films are clamped face to face (P3HT film staggered for easier water penetration) and the edge is exposed to deionized water which dissolves the PSS, allowing the sacrificial substrate to be removed. The film is then dipped in water to remove residual PSS. Finally, the top electrode is deposited at pressures below  $5 \times 10^{-7}$  Torr; after MoO<sub>3</sub>, Ag (either 100 nm for bottom illuminated devices, or 15 nm for top illuminated, temperature and intensity modulated measurement) is deposited through a circular shadow mask of either 1 mm or 3mm in diameter.

## Section 6: Characteristics of a donor-spacer-acceptor photovoltaic device

Photovoltaic devices are fabricated with PPE layers as spacers between the P3HT and PCBM films. Interestingly, no strong  $V_{oc}$  response is observed when varying the sub-nanometer donor-acceptor spacing, as shown in Figures 2.6, 2.7 and 2.8. The  $J_{sc}$  and fill factor (FF) are reduced in the presence of the spacer (more on this later), an indication that the spacer is fully surface covering, but they do not trend with alkyl length. Also, the spacer with an alkyl length of four carbons is not fully surface covering, so that sample shows how a hole-filled spacer behaves; a spacer which is not fully surface covering provides an intermediate reduction in FF and  $J_{sc}$ .

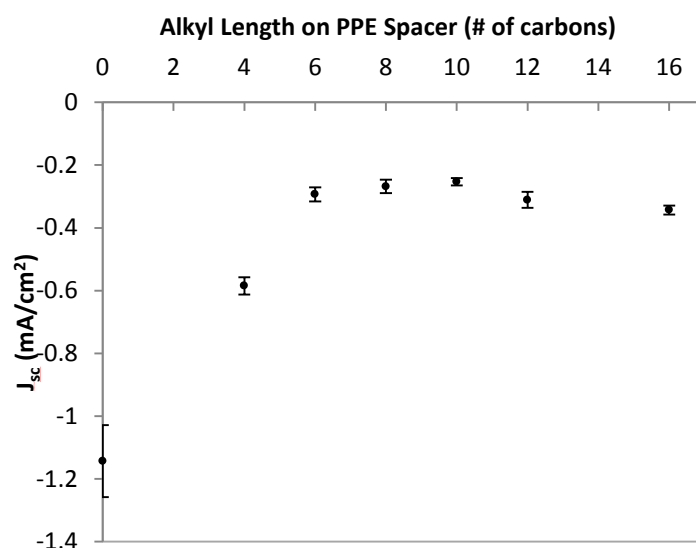


Figure 2.6:  $J_{sc}$  decreases when PPE is added at the donor acceptor interface because the energy levels of PPE prevent electron transfer from P3HT to PCBM. However, there is no appreciable trend in alkyl length on the PPE spacer (note that the PPE with a 4 carbon side chain does not form fully surface-covering films).

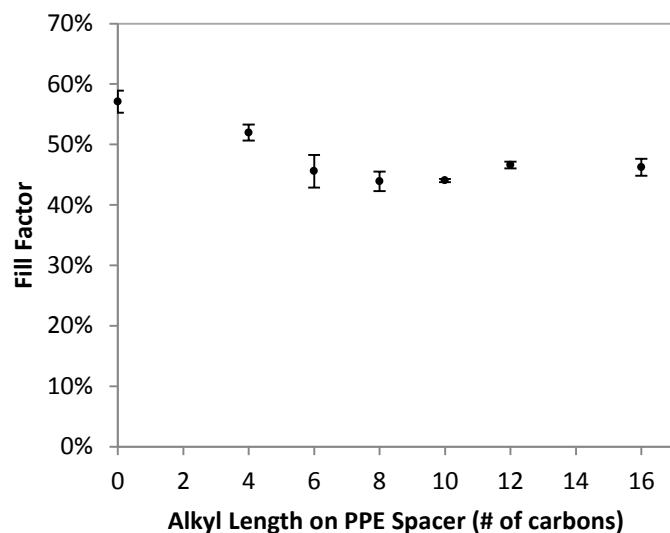


Figure 2.7: FF decreases when PPE is added at the donor acceptor interface. Again, there is no appreciable trend in alkyl length on the PPE spacer (note that the PPE with a 4 carbon side chain does not form fully surface-covering films).

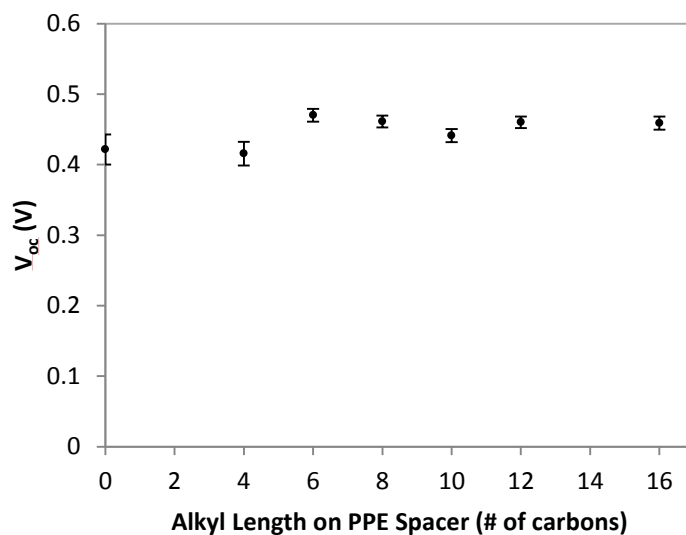


Figure 2.8:  $V_{oc}$  is nearly unchanged when PPE is added at the donor acceptor interface. Notably, in spite of the length control implied by the AFM measurements, there is no appreciable trend in  $V_{oc}$  change with alkyl length on the PPE spacer (note that the PPE with a 4 carbon side chain does not form fully surface-covering films).

The alkyl-length modulated monolayer spacer devices appeared to have no influence upon recombinative loss to the  $V_{oc}$ . This is in great contrast to the many studies which have correlated the bulkiness of donor side chains (and thus the molecular spacing at the donor-acceptor interface, which we claim to have directly controlled here) to reduced geminate recombination. It was not until multilayers were placed at the donor acceptor interface that we observed thickness dependent trends. Although the multilayer PPE films with six carbon side chains (multiples of 0.79 nm, used in the rest of this study) pass through the same spacing-thickness regimes as the monolayer films (0.79 to 2.06 nm thick), the same device trends were not observed, likely because the spacer energy levels (forming a conjugated bridge/barrier in the multilayer) have a stronger impact than aliphatic side chain spacing.

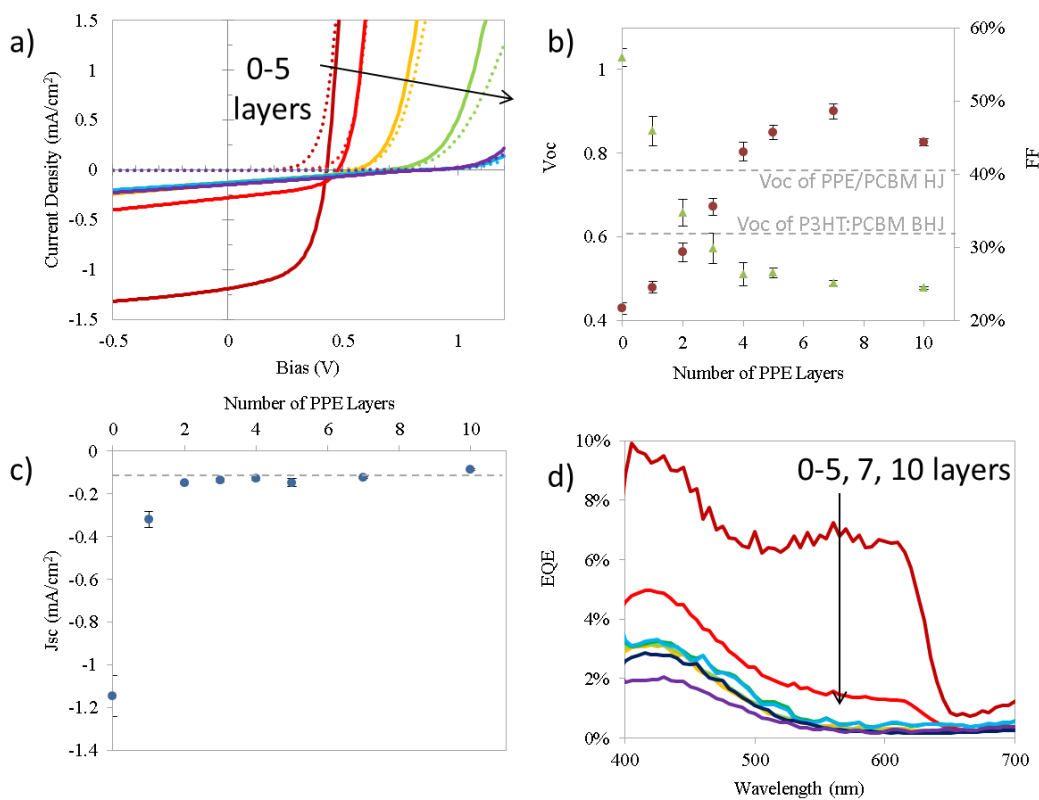


Figure 2.9: (a) J-V curves for devices with an increasing number of PPE spacer layers at the donor-acceptor junction show a decreasing  $J_{sc}$  and an increasing  $V_{oc}$ . The  $J_{sc}$  falls off after two layers (c) and the  $V_{oc}$  rises over seven layers at the expense of fill factor (b). (d) The EQE of OPV cells with different thicknesses of PPE spacers.

The insertion of multilayers of PPE causes the photocurrent to fall off rapidly and the  $V_{oc}$  to gradually rise at the expense of fill factor, as can be seen in Figure 2.9. This results in a reduced power conversion efficiency. Notably, the planar heterojunction has a lower  $V_{oc}$  than a BHJ device ( $V_{oc}$  of 0.57-0.6 V) [49,52]. This may be due to increased recombination or due to the lower interface area; when fewer excitons reach and are separated at the interface, analogous to reduced illumination, the  $V_{oc}$  is diminished [7]. Additionally, the maximum  $V_{oc}$  obtained in the spacer devices remains lower than the energy gap of the P3HT/PCBM junction (about 1.1 eV). The peak  $V_{oc}$  of the spacer devices also exceeds that of devices without P3HT (PPE/PCBM junctions), as shown below and indicated in Figure 2.9. This evidence suggests that the spacer is active in affecting the  $V_{oc}$ .

A set of control devices were fabricated and measurements were taken to show the influence of water and the PPE/PCBM junction on the device. First, although all of the devices are exposed to water during Langmuir-Schaefer film transfer, the water does not account for the change in  $V_{oc}$  and the cut-off of P3HTs contribution to photocurrent (more on this topic below), as shown in Figures 2.10 and 2.11 and in Table 2.1. The sample which had the donor-acceptor interface exposed to water displays diminished  $V_{oc}$ ,  $J_{sc}$  and fill factor, possibly due to molecular reorientation upon water exposure. The PPE spacer device interfaces are likely protected from the water by the PPE.

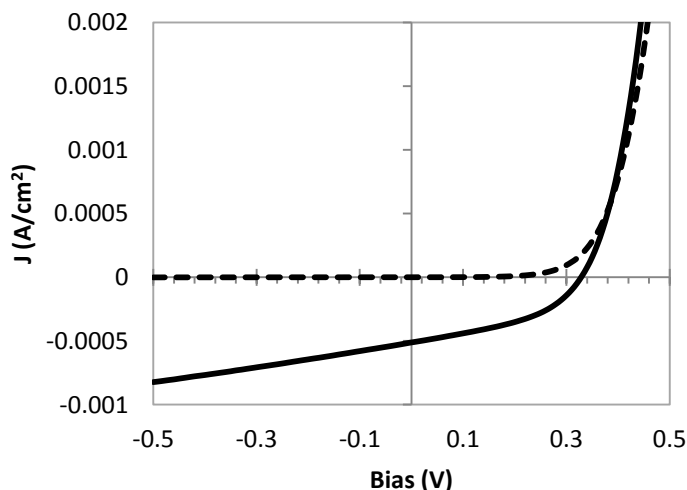


Figure 2.10: The J-V characteristics of a device where PCBM was dipped into water 5 times before P3HT was transferred onto it shows that the  $V_{oc}$  does not increase due to water dipping.

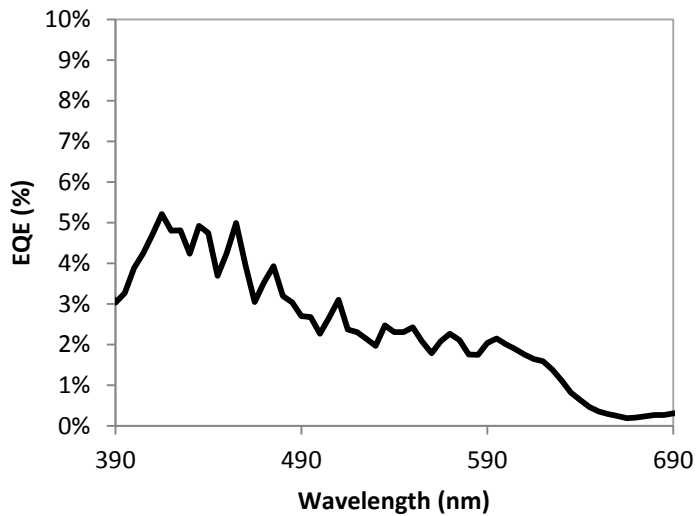


Figure 2.11 The EQE of a device where the PCBM film was dipped into water 5 times before P3HT was transferred onto it shows that P3HT (photocurrent from wavelengths 550-650 nm) still contributes to photocurrent.

Table 2.1: The device parameters for control devices. ITO/PEI/PCBM/(Control)/MoO<sub>3</sub>/Ag. All of these deviations are for devices within a single substrate

	5x water dip	PCBM only	PPEx3	PPEx5	PPE (5mg/mL)	PPE (10mg/mL)	PPE (20mg/mL)
V <sub>oc</sub> (V)	0.32±0.01	0.01	0.75±0.02	0.76±0.01	0.35±0.08	0.4±0.1	0.5±0.1
J <sub>sc</sub> (mA/cm <sup>2</sup> )	0.48±0.03	0.35±0.01	0.11±0.02	0.19±0.01	0.02±0.01	0.03±0.02	0.04±0.02
FF (%)	43.5±0.4	16±10	21±1	31.6±0.6	22±3	35±2	38±3
PCE (%)	0.07±0.01	0	0.02	0.05	0	0.01	0.01±0.01

Next, Figure 2.12 shows the character of devices with the structure ITO/PEI/PCBM/layer/MoO<sub>3</sub>/Ag where the layer is nothing, 3 layers PPE or 5 layers PPE.

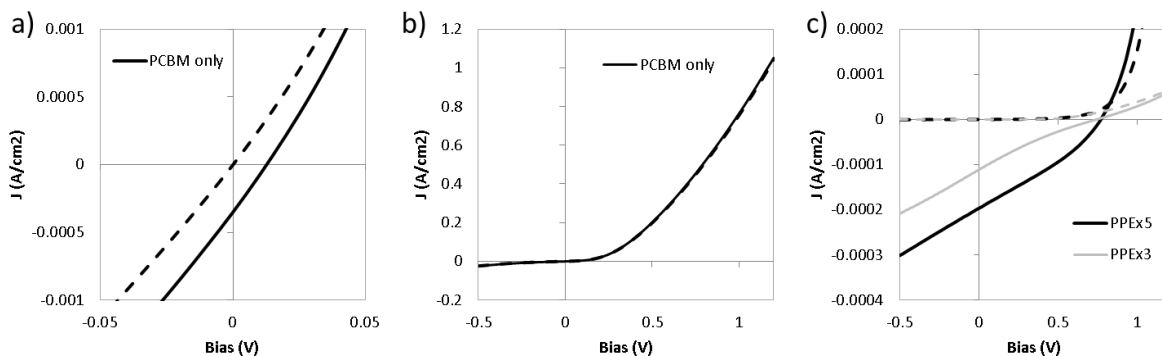


Figure 2.12: (a) and (b): PCBM only. (c): PCBM/PPE where PPE is either 3 or 5 monolayers thick. These plots show that PCBM can produce photocurrent without a strongly absorbing donor, and that thin films of PPE do not make efficient devices.

It is notable that the  $V_{oc}$  does not vary with the thickness of the very thin PPE film devices. When the PPE layer is made much thicker, as in Figure 2.13, by transferring a film spincast at 1000 rpm for 30s from chlorobenzene solution, the  $J_{sc}$  and  $V_{oc}$  are further reduced (although they seem to be increasing as the PPE gets thicker). The devices likely suffered from the low molecular weight of the PPE both in film transfer (the films cracked) and in semiconducting character. These control devices show that PPE does not independently reach the high  $V_{oc}$  which is present in the spacer devices and that it does not strongly produce photocurrent.

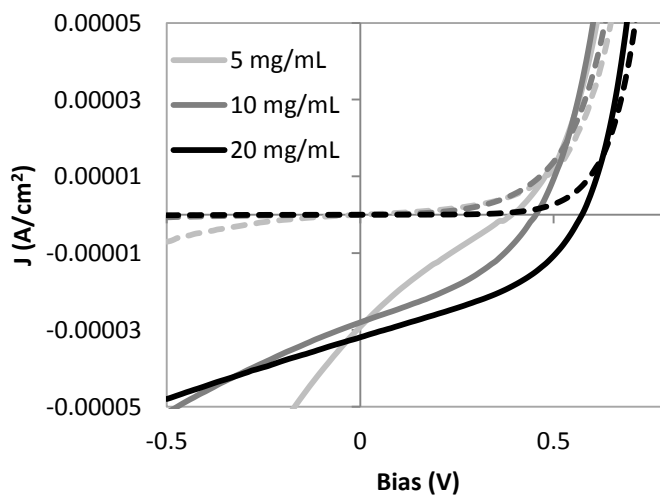


Figure 2.13: Some J-V curves from devices with thick PPE donor layers.

The external quantum efficiency (EQE) of the OPV cells shows how absorption, charge transfer, extraction, and collection influence current density. We assume that the EQE plots, with respect to the number of spacer layers, primarily represent changes in charge transfer because we hold the electrode contacts constant and because PPE absorption does not contribute appreciably to photocurrent production. We argue that the PPE does not appreciably contribute to the photocurrent in the devices based on four bits of data: 1) PPE's contribution to the overall device absorption (Figure 2.14) is small; 2) PPE's contribution to the absorption increases with its thickness; 3) the EQE, Figure 2.9, does not increase where PPE absorbs in spite of increasing thickness; 4) the photocurrent in PCBM/PPE devices is quite small despite probing large differences in PPE thickness (Figure 2.15, Table 2.1). Since the absorption strength of the PPE is low, its potential photocurrent production is miniscule compared to that from absorption in PCBM and in P3HT. Further, the PPE absorption increases with thickness- if PPE contributed to photocurrent, we'd expect to see an increase in EQE where it was absorbing (this is not the case). Also, if PPE were effective at separating and conducting charge, we'd see an optimum PPE thickness for photocurrent production in PPE/PCBM devices. Since the addition of PPE only seems to decrease photocurrent below that of the PCBM only device, we argue that it does not effectively contribute to the operation of the device except as a spacer.

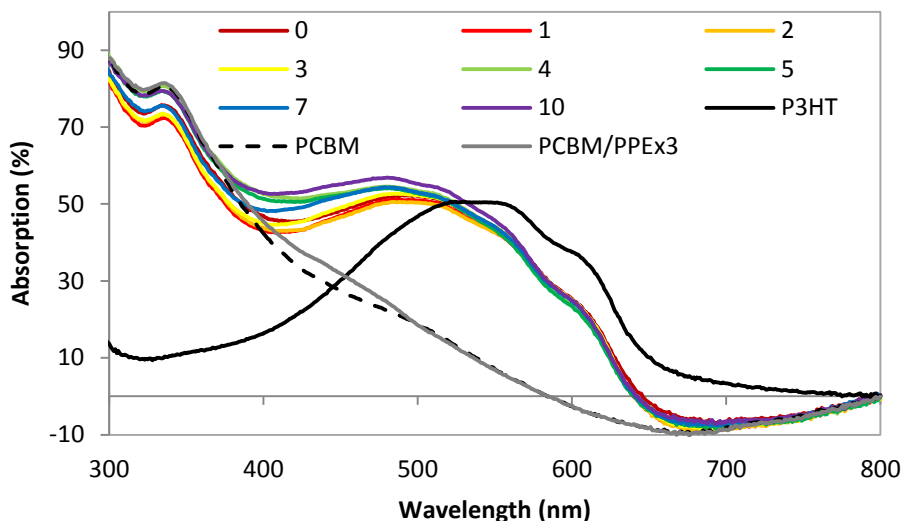


Figure 2.14: Absorption plots for devices show that as the number PPE layers increases, so does its contribution to absorption.

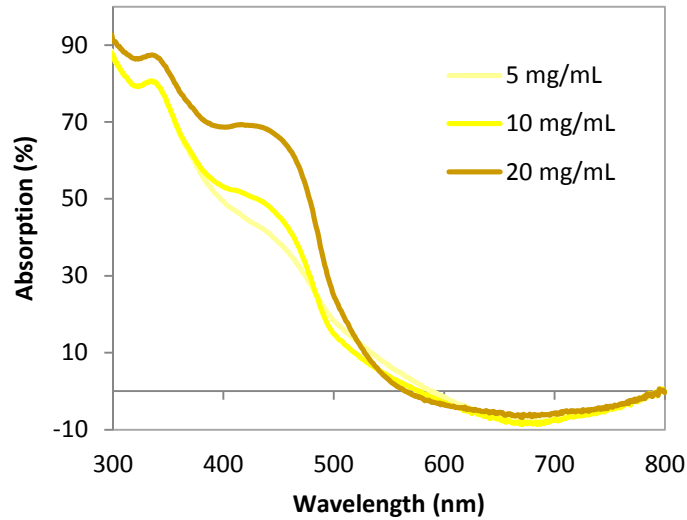


Figure 2.15: Absorption plots for PPE/PCBM devices film transferred devices.

As can be seen in Figure 2.9, the EQE of the multilayer spacer devices rapidly drops over the first two spacer layers. Then, the EQE stays fairly constant until seven or more layers are present, when it begins to drop again. This drop may account for the decreased  $V_{oc}$  with ten spacer layers, as decreased charge separation at the interface should decrease both  $J_{sc}$  and  $V_{oc}$  [7]. Importantly, the EQE response for wavelengths over 550 nm, corresponding solely to the contribution from P3HT, is completely cut off with increasing spacing. This change is in contrast to a water-dipped sample (no spacer was deposited, but PCBM was exposed multiple times to water, Figure 2.11) where P3HT still contributes to photocurrent after multiple exposures to water. The spacer likely presents an energy barrier which suppresses charge transfer from P3HT. After P3HT's contribution is cut out, the remaining photocurrent comes from absorption and charge transfer from PCBM.

The fill factor is a characterization of the efficacy of charge extraction and charge injection into a photovoltaic device. Defined as the ratio between the maximum power point and the  $V_{oc}$ - $J_{sc}$  product, the fill factor is an inappropriate characterization metric for devices where typical device charge carrier pathways are being modified. For instance, FF falls off with increasing spacing, but this is not an indication of a suffering device. After P3HT's contribution

to photocurrent is cut off, the devices have a spacer-independent maximum power. Thus, as the  $V_{oc}$  (in the denominator of FF) rises, the FF falls accordingly.

### Section 7: Temperature dependence of the open circuit voltage

The  $V_{oc}$  of organic photovoltaic devices is predicted to have both material and device property and environmental dependencies. Many descriptions of the  $V_{oc}$  of OPVs have been made, each taking a slightly different form, but generally containing a constant dependence upon the donor-HOMO to acceptor LUMO energy gap (less a binding energy), a linear dependence upon temperature and a logarithmic dependence upon illumination intensity [7,19-23]. The description by Giebink, et al., clearly indicates these dependencies:

$$qV_{OC} = \Delta E_{D-A} - E_B - nkT \cdot \ln\left(\frac{A}{J_x}\right)$$

where  $\Delta E_{D-A}$  and  $E_B$  are the energy dependencies,  $n$  is an ideality factor,  $k$  is the Boltzmann constant,  $A$  is a constant depending upon recombination, and  $J_x$  is the illumination intensity dependent factor. In order to help extricate the origin of the change in  $V_{oc}$  when spacers are included in the OPVs, one set of devices were subjected to measurement under temperature and light intensity variation. As expected, the  $V_{oc}$  increases with the logarithm of light intensity and increases with decreasing temperature, as in Figure 2.16 (more plots are in Appendix 1).

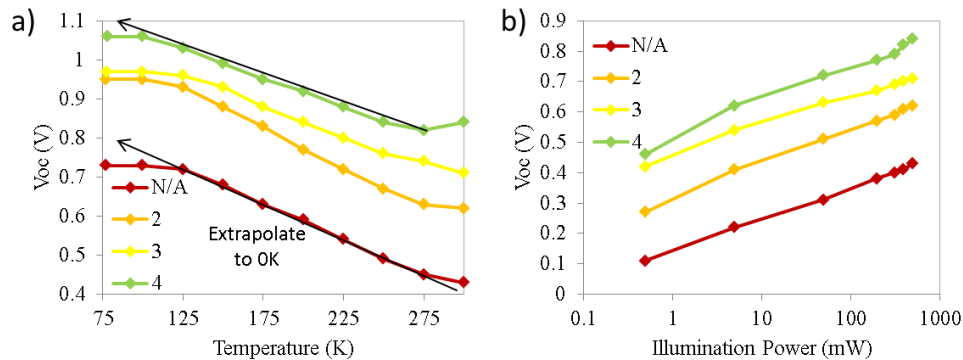


Figure 2.16: The illumination intensity (b) and temperature (a) dependence of the  $V_{oc}$  of OPVs with PPE spacers at the donor-acceptor interface.

The effective energy of the polaron pair ( $\Delta E_{D-A} - E_B$ ), an upper bound for the  $V_{oc}$ , is approximated by extrapolating the linear region of the  $V_{oc}$  vs. temperature plot to the y-axis intercept (0 K) where recombination would be suppressed, Figure 2.17 [7]. Our analysis suggests that the insertion of the spacer incrementally increases the energy available to create voltage, from 0.95 to about 1.25 eV. This gain in potential is less than the 0.5 eV difference between donor and spacer HOMO levels, but it puts the energy above the 1.1 eV P3HT/PCBM junction gap (as estimated via cyclic voltammetry). Nevertheless, this increase does not likely originate from mixing between the HOMO levels of the PPE spacer and P3HT. Although it is plausible that some PCBM has diffused through the spacer to come into contact with P3HT, the rapid drop in P3HT photocurrent as spacing increases indicates that no strong connections between P3HT and PCBM are present. We instead postulate that the energy drop at the PPE/P3HT interface separates the geminate polaron pair into free charges (removing the P3HT/PCBM junction energy constraint) and that the distance dependence is due to a change in binding energy as charge accumulates at the spacer interface.

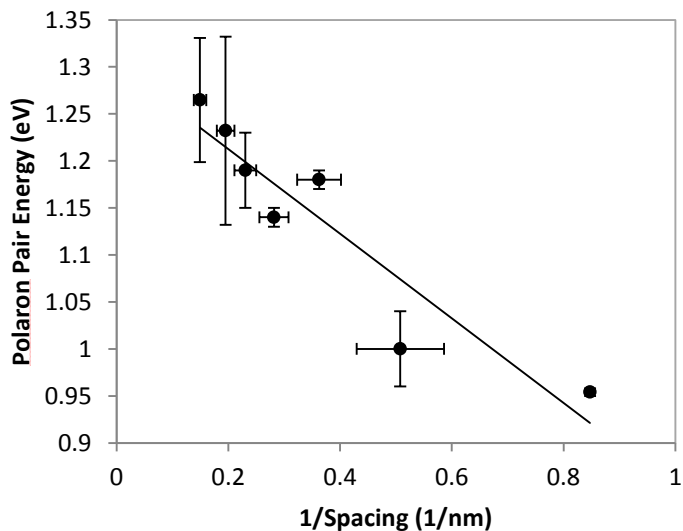


Figure 2.17: The spacer thickness dependence of the polaron pair energy value extracted from the y-axis intercept of the  $V_{oc}$ -temperature dependence is plotted.

The charge binding energy takes the form of a coulombic attraction, where  $r_0$  is the innate separation of charges at the donor-acceptor interface,  $r$  is the separation added by the spacer,  $q$  is the electron charge, and  $\varepsilon$  is the dielectric constant:

$$E_B = \frac{q^2}{4\pi\varepsilon_0\varepsilon_r} \frac{1}{r_0 + r}.$$

In order to see if our postulation is plausible, we assume that the dielectric constant of the interface is similar to that of P3HT ( $\varepsilon_r = 3.2$ ) and fit an inverse dependence upon the measured spacer thickness to extract  $r_0$ , as in Figure 2.17 [53]. The increase in polaron energy with increasing spacing trends well with a decrease in coulomb binding. The fitted value for the innate interface charge separation, 1.2 nm, is a large, but plausible number. This interpretation of evidence suggests that a reduction in charge pair binding with increasing spacing is a reasonable explanation for an increase in the polaron pair energy. This gain, however, does not account fully for the increase in  $V_{oc}$ .

## Section 8: Spacer limited diode injection current

The dark condition J-V characteristics of OPV cells carry information about the nature of their transport. As seen in Figure 2.18, increasing the thickness of the spacer suppresses the dark current as the series resistance increases and the low-bias kink, defined by the intercept of lines drawn by the two low-bias slopes, shifts to the right.

We assume that the shape of the dark current is dominated by the slowest conduction or fastest recombination pathway available at an applied bias. Therefore, the motion of the kink represents a spacer dependent change in the current-limiting processes in the device. We postulate that the spacer's energy barriers prevent anode-injected carriers from easily reaching and recombining at the spacer-acceptor interface, limiting the dark current [54]. Since  $V_{oc}$  occurs at a bias where photocurrent and injected current effectively balance each other, if the photocurrent is constant but the rise in injected, dark current is decreased, the  $V_{oc}$  is raised. Although the shift in kink bias serves as an indirect indication of reduced recombination, its

correlation with  $V_{oc}$  is clear; as the polaron pair energy and the kink bias increase, each with respect to the number of spacer layers, the  $V_{oc}$  also rises, Figure 2.18.

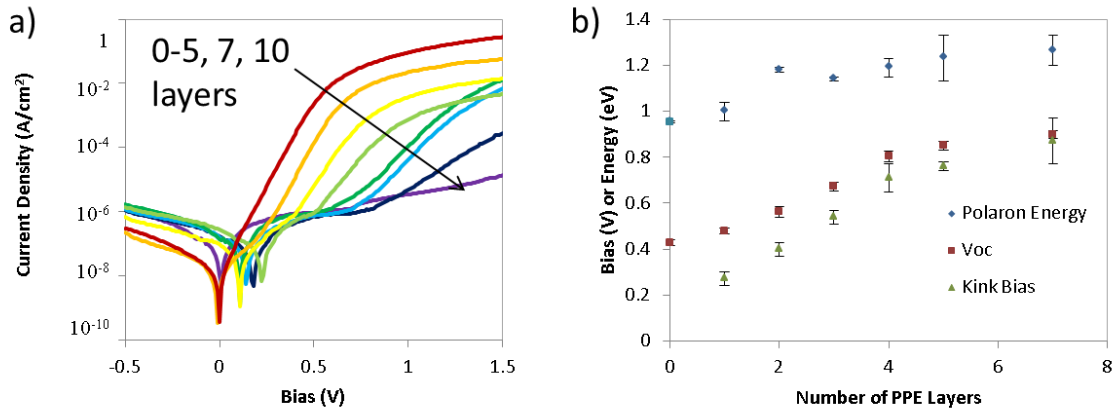


Figure 2.18: (a) Semi-logarithmic dark J-V characteristics and (b) a comparison between the dark current kink bias, the polaron pair energy, and the  $V_{oc}$ .

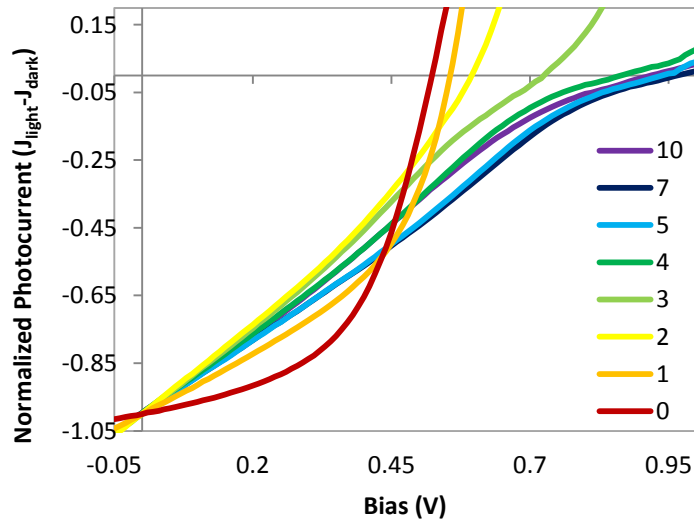


Figure 2.19. The normalized photocurrent characteristics of OPVs with an increasing number of PPE layers at the donor-acceptor interface.

The subtraction of the dark condition, diode curve from the curve taken under illumination (normalized by  $J_{sc}$ ), as in Figure 2.19, shows that the reduced dark current leads to

an increase in photocurrent at a given applied bias, ultimately resulting in a higher  $V_{oc}$ . While this does not imply causation, it is reasonable to state that the spacer-controlled, current-limiting process which shifts the dark curve kink to the right accounts for the difference between the change in polaron pair energy and the change in  $V_{oc}$ . The spacer layer interferes with charge transport through the diode, reducing the dark current and leading to an increase in the  $V_{oc}$ .

## Section 9: Contrasting the molecular spacing dependence of charge transfer and recombination

This experiment presents an interesting picture about molecular design for reducing loss to the  $V_{oc}$ . The disparity in distances over which charge transfer and dark current are shut down is notable; it takes only two monolayers to suppress charge transfer, but the injected dark current, presumably sustained by recombination at the charge-separating interface, is still falling at five monolayers (although it does decrease by about an order of magnitude per layer) [55,56]. This is in stark contrast to studies where a bulk material is given a small change in alkyl side chain length or bulkiness and a large change in  $V_{oc}$ , attributed to increased donor-acceptor interfacial spacing and reduced recombination, is observed. The thickness trends that appear in the multilayer devices indicate that our interfacial changes are not as effective as bulk material change in reducing  $V_{oc}$  loss. Alternately, this may imply that material changes not local to the donor-acceptor interface affect  $V_{oc}$  loss. Our results uphold the notion that reduction of  $V_{oc}$  loss is complicated.

The development of molecular design principles for reducing loss to the  $V_{oc}$  of OPV cells is an important endeavor which is complicated by the coupling between device parameters and material properties. We have introduced a change to the molecular structure of a planar heterojunction OPV local to the donor-acceptor interface via insertion of self-assembled Langmuir- Schaefer monolayers. This small change introduced a decrease in  $J_{sc}$ , due to reduced charge transfer from P3HT, and an increase in  $V_{oc}$ , due to incremental increases in polaron pair energy as well as a reduction in dark current. This experiment has de-coupled the effects of absorption and energy level change from reduction in loss to the  $V_{oc}$  and has implications for appropriate design of high  $V_{oc}$  molecules.

## Section 10: References

1. C. Deibel and V. Dyakonov, *Rep. Prog. Phys.* **73**, 096401 (2010).
2. F. Krebs, J. Fyenbo and M. Jørgensen, *J. Mater. Chem.* **20**, 8994 (2010).
3. H. J. Park, M.-G. Kang, S. H. Ahn and L. J. Guo, *Adv. Mater.* **22**, E247 (2010).
4. H. Zhou, L. Yang and W. You, *Macromolecules* **45**, 607 (2012).
5. H. J. Son, F. He, B. Carsten and L. Yu, *J. Mater. Chem.* **21**, 18934 (2011).
6. Y. Li, *Acc. Chem. Res.* **45**, 723 (2012).
7. N. Giebink, G. Wiederrecht, M. Wasielewski and S. Forrest, *Phys. Rev. B* **82**, 155305 (2010).
8. H. Nicolai, M. Kuik, G. Wetzelaer, B. de Boer, C. Campbell, C. Risko, J. Bredas and P. Blom, *Nat. Mater.* **11**, 882 (2012).
9. A. Bakulin, A. Rao, V. Pavelyev, P. van Loosdrecht, M. Pshenichnikov, D. Niedzialek, J. Cornil, D. Beljonne and R. Friend, *Science* **355**, 1340 (2012).
10. D. Wehenkel, L. Koster, M. Wienk and R. Janssen, *Phys. Rev. B* **85**, 125203 (2012).
11. C. Renshaw, J. Zimmerman, B. Lassiter and S. Forrest, *Phys. Rev. B* **86**, 085324 (2012).
12. B. Rand, D. Burk and S. Forrest, *Phys. Rev. B* **75**, 115327 (2007).
13. S. Yamamoto, A. Orimo, H. Benten and S. Ito, *Adv. Energy Mater.* **2**, 229 (2012).
14. V. Mihailetschi, P. Blom, J. Hummelen and M. Rispens, *J. App. Phys.* **94** 6849 (2003).
15. K. Vandewal, A. Gadisa, W. Oosterbaan, S. Bertho, F. Banishoeib, I. Van Severen, L. Lutsen, T. Cleij, D. Vanderzande and J. Manca, *Adv. Funct. Mater.* **18**, 2064 (2008).
16. T. Yamanari, T. Taima, J. Sakai and K. Saito, *Sol. Energy Mater. Sol. Cells* **93**, 759 (2009).
17. A. Gadisa, M. Svensson, M. Andersson and O. Inganäs, *App. Phys. Lett.* **84**, 1609 (2004).
18. M. Hallermann, E. Da Como, J. Feldmann, M. Izquierdo, S. Filippone, N. Martín, S. Jüchter and E. von Hauff, *App. Phys. Lett.* **97**, 023301 (2010).
19. K. Vandewal, K. Tvingstedt, A. Gadisa, O. Inganäs and J. Manca, *Nat. Mater.* **8**, 904 (2009).
20. K. Vandewal, K. Tvingstedt, J. Manca and O. Inganäs, *IEEE J. Sel. Top. Quantum Electron.* **16**, 1676 (2010).
21. M. Perez, C. Borek, S. Forrest and M. Thompson, *J. Am. Chem. Soc.* **131**, 9281 (2009).
22. N. Giebink, B. Lassiter, G. Wiederrecht, M. Wasielewski and S. Forrest, *Phys. Rev. B* **82** 155306 (2010).
23. D. Veldman, S. Meskers and R. Janssen, *Adv. Funct. Mater.* **19** 1939 (2009).
24. L. Huo, J. Hou, S. Zhang, H.-Y. Chen and Y. Yang, *Angew. Chem.* **122**, 1542 (2010).
25. S. Xiao, A. Stuart, S. Liu and W. You, *ACS Appl. Mater. Interfaces* **1**, 1613 (2009).
26. H.-Y. Chen, J. Hou, S. Zhang, Y. Liang, G. Yang, Y. Yang, Y. Wu and G. Li, *Nat. Photonics* **3**, 649 (2009).
27. Y.-J. Cheng, S.-W. Cheng, C.-Y. Chang, W.-S. Kao, M.-H. Liao and C.-S. Hsu, *Chem. Commun.* **48**, 3203 (2012).
28. D. Lee, S. Stone and J. Ferraris, *Chem. Commun.* **47**, 10987 (2011).

29. J. Hou, T. Chen, S. Zhang, L. Huo, S. Sista and Y. Yang, *Macromolecules* **42**, 9217 (2009).
30. Z. Li, Y. Zhang, S.-W. Tsang, X. Du, J. Zhou, Y. Tao and J. Ding, *J. Phys. Chem. C* **115**, 18002 (2011).
31. D. Stevens, J. Speros, M. Hillmyer and D. Frisbie, *J. Phys. Chem. C* **115**, 20806 (2011).
32. E. Wang, L. Hou, Z. Wang, Z. Ma, S. Hellström, W. Zhuang, F. Zhang, O. Inganäs and M. Andersson, *Macromolecules* **44**, 2067 (2011).
33. B.-G. Kim, M.-S. Kim, J. Kim, *ACS Nano* **4**, 2160 (2010).
34. B.-G. Kim, E. J. Jeong, H. J. Park, D. Bilby, L. J. Guo, J. Kim, *ACS Appl. Mater. Interfaces* **3**, 674 (2011).
35. L. Yang, H. Zhou and W. You, *J. Phys. Chem. C* **114**, 16793 (2010).
36. W. Oosterbaan, J.-C. Bolsée, A. Gadisa, V. Vrindts, S. Bertho, J. D'Haen, T. Cleij, L. Lutsen, C. McNeill, L. Thomsen, J. Manca and D. Vanderzande, *Adv. Funct. Mater.* **20**, 792 (2010).
37. Y. Li, Y. Chen, X. Liu, Z. Wang, X. Yang, Y. Tu and X. Zhu, *Macromolecules* **44**, 6370 (2011).
38. A. Zoombelt, M. Leenen, M. Fonrodona, Y. Nicolas, M. Wienk and R. Janssen, *Polymer* **50**, 4564 (2009).
39. S. Lai, M. Lo, M. Chan, C. Lee and S. Lee, *App. Phys. Lett.* **95**, 153303 (2009).
40. C. Goh, S. Scully and M. McGehee, *J. App. Phys.* **101**, 114503 (2007).
41. Z. Liu, M. Lo, H. Wang, T. Ng, V. Roy, T. Lee and S. Lee, *App. Phys. Lett.* **95**, 093307 (2009).
42. T. Ng, M. Lo, Y. Zhou, Z. Liu, C. Lee, O. Kwon and S. Lee, *App. Phys. Lett.* **94**, 193304 (2009).
43. B. Yang, Y. Yuan, P. Sharma, S. Poddar, R. Korlacki, S. Ducharme, A. Gruverman, R. Saraf and J. Huang, *Adv. Mater.* **24**, 1455 (2012).
44. T. Heidel, D. Hochbaum, J. Sussman, V. Singh, M. Bahlke, I. Hiromi, J. Lee and M. Baldo, *J. App. Phys.* **109**, 104502 (2011).
45. J. Huang, J. Yu, W. Wang and Y. Jiang, *App. Phys. Lett.* **98**, 023301 (2011).
46. M. Lloyd, Y.-F. Lim and G. Malliaras, *App. Phys. Lett.* **92**, 143308 (2008).
47. W. Luhman and R. Holmes, *Adv. Funct. Mater.* **21**, 764 (2011).
48. Y. Liu, M. Summers, C. Edder, J. Fréchet and M. McGehee, *Adv. Mater.* **17**, 2960 (2005).
49. A. Tada, Y. Geng, Q. Wei, K. Hashimoto and K. Tajima, *Nat. Mater.* **10**, 450 (2011).
50. J. Kim and T. Swager, *Nature* **411**, 1030 (2001).
51. Y. Zhou, C. Fuentes-Hernandez, J. Shim, J. Meyer, A. Giordano, H. Li, P. Winget, T. Papadopoulos, H. Cheun, J. Kim, M. Fenoll, A. Dindar, W. Haske, E. Najafabadi, T. M. Khan, H. Sojoudi, S. Barlow, S. Graham, J.-L. Brédas, S. Marder, A. Kahn and B. Kippelen, *Science* **336**, 327 (2012).

52. J. Kim, Z.-L. Guan, S. Lee, E. Pavlopoulou, M. Tonay, A. Kahn, Y.-L. Loo, *Org. Electron.* **12**, 1963 (2011).
53. S. Scheinert, W. Schliepke, *Synth. Metals.* **139**, 501-509 (2003).
54. W. Tress, K. Leo, M. Riede, *Adv. Funct. Mater.* **21**, 2140 (2011).
55. G. Wetzelaer, M. Kuik, P. Blom, *Adv. Energy Mater.* **2** 1232 (2012).
56. R. Street, M. Schoendorf, A. Roy, J. Lee, *Phys. Rev. B* **81** 205307 (2010).
57. D. Bilby, J. Amonoo, M. Sykes, B. Frieberg, B. Huang, J. Hungerford, M. Shtein, P. Green, J. Kim, *Appl. Phys. Lett.* **103** 203902 (2013).

### Chapter 3: Desirable characteristics for electrode buffer layer structure

Organic photovoltaic cells (OPVs) have been a fascinating research topic due to their readily adjustable material and device properties [1-3]. Organic synthesis has provided tools for tuning molecular energy levels, band gaps, miscibility and to some extent crystallinity, while device structure variation has allowed for the study of interfaces, energy level alignment and charge and exciton transport in thin films [4-12]. The various tuning parameters available in OPVs provide a fertile basis for illuminating the still mysterious loss processes which have limited device efficiencies and have prevented their practical application [13-16]. Once the device physics have been sufficiently explored, the lightweight materials and compatibility with high throughput manufacturing, such as roll-to-roll processing on flexible substrates, will potentially enable OPVs to occupy niche installation venues [17-20]. These devices, however, require fairly complicated structures with multiple layers and controlled mixing of materials in order to function properly.

A simplistic description of OPV device operation provides motivation for device structure. OPV devices can be viewed as diodes which produce power under illumination, however their photocurrent production and diode characteristics, while linked, are not often described with distinction. Most commonly wrote is the photocurrent production mechanism. Light is absorbed by an electron donor material, creating an exciton. This exciton is separated into an electron and hole after diffusing to the interface with an electron accepting material [21-24]. Finally, the charges are conducted to electrodes to provide current in an external circuit. This process is pivotal upon the proximity (due to the interface's importance in charge separation) and percolation (in order to conduct charge to an electrode) of the donor and acceptor materials' phases (the film morphology). Photocurrent production also requires that light with an appropriate wavelength passes through the electrodes into the absorbing material. This seems to dictate that a bulk heterojunction (BHJ) morphology on a transparent electrode, with a reflecting opposite electrode (to gain absorption via interference) is necessary for device function [25,26].

The organic material based diode that constitutes an OPV platform has a seemingly simple objective: block charge injection under one bias (reverse) direction and allow it in the other. More subtly, in a solar cell the diode must not allow injection of charge under forward bias until some fairly large positive bias has been reached (if the diode let maximum current through under very small positive bias, although it would be a good diode, the photocurrent would be cut off prematurely since it flows opposite to the injection). Diode-like character can be easily obtained in semiconducting materials by selectively contacting the highest occupied molecular orbital (HOMO) energy level with one contact and the lowest unoccupied molecular orbital (LUMO) energy level with the other electrode. With appropriate device contact energy levels, current cannot easily be injected into the device under reverse bias, but it can pass under forward bias, as in Figure 3.1. In OPVs, the forward bias diode character is tempered by the barrier from the LUMO of the acceptor to the LUMO of the donor (same for the HOMO barrier); electrons injected onto the LUMO of the acceptor material reach the interface with the donor and then recombine with a hole trapped at the same interface on the HOMO of the donor. This leads to a more gradual turn on of diode current. Thus the device structure required for good injection hinges upon the concept of “good electrical contact.”

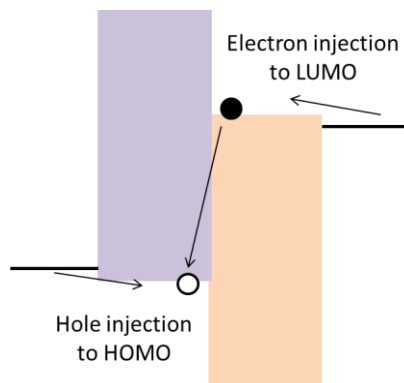


Figure 3.1: Photovoltaic diode injection under forward bias. Electrons are injected onto the LUMO of the acceptor (orange) and holes onto the HOMO of the donor (purple). Charge carriers are conducted to the interface between the materials where they recombine and allow for charge flow.

The shape of the current-voltage curve obtained when characterizing OPVs can be illustratively predicted based upon simplistic device structure drawings, including consideration of the requirements for photocurrent extraction and charge injection. When device has a BHJ

morphology with very finely phase separated domains on a length scale comparable to the exciton diffusion length (about 5-10 nm), but also has very well connected phases, as depicted in Figure 3.2 a), good device behavior is expected [27,28]. Since an exciton splitting interface is always nearby, and since there is a clear and direct conduction pathway for each charge carrier (the circles in the drawing) to its appropriate electrode, the device will create a high photocurrent even under small forward bias. Then as bias is increased, the charge selective (due to the grey layer at the surface) electrodes allow for the injection of holes onto the donor and electrons on to the acceptor; charge injection suddenly rises at a certain threshold bias, creating the traditional “J” shaped curve with a sharp rise and a high fill factor (FF).

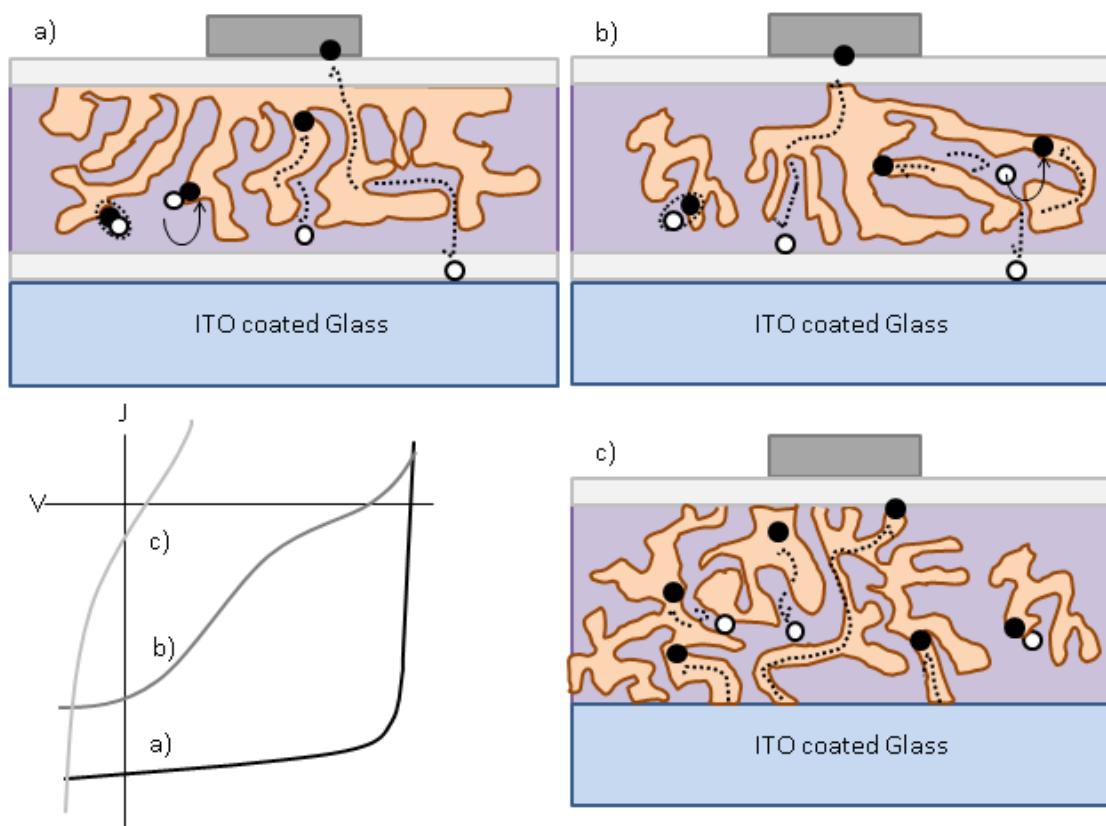


Figure 3.2: Idealized drawings of OPVs with bulk heterojunction morphologies with excellent (a), mediocre (b), and poor (c) structure and the predicted current-bias curve which would come from that device under illumination. Open circles represent holes and filled circles represent electrons.

When the morphology of a device does not have well connected domains and electrodes, even if there is a high surface area, as in Figure 3.2 b), the device character will suffer. Since the charge conduction pathways are disconnected or long, there is a greater chance for charge to

recombine, leading to a decreased short circuit current density ( $J_{sc}$ ) and a decreased open circuit voltage ( $V_{oc}$ ). Further, since there is poor connectivity to the charge selective electrodes, it is difficult to inject and extract charge. This means that increasing bias leads to a drop off of photocurrent before injection can begin and results in a curve with a kink.

If a device is made with overly percolated BHJ morphology and non-charge selective electrodes, as in Figure 3.2 c), the device fails to operate as a diode or a photovoltaic cell. The long tortuous pathways encourage recombination of the photogenerated charge instead of extraction. Further, since there is connectivity between both electrodes on a single phase, charge injection from the non-selective electrodes leads to a failure of the diode as charge can enter the device at any bias (leakage current which bypasses the OPV diode). Thus high levels of charge injection overpower the photocurrent at any bias and lead to a very small FF. The increase in charge carriers in the device due to non-selective injection further exacerbates the recombination problem too, so there is very little  $J_{sc}$  and  $V_{oc}$ . Poor device structure can result in short-circuit like J-V behavior.

The BHJ morphology seems to be a primary driver for the efficacy of a device, but even a good BHJ morphology cannot function without properly designed electrical contacts. The characteristics of a good contact include transparency to visible light, selectivity of electrical charge and compatibility with device fabrication and morphology control routes (i.e. intermixing or reactivity of the electrical contact with the active material can create charge trapping sites). There are few materials available which satisfy all of these requirements. For instance, although indium-tin oxide (ITO) is conductive, transparent and insoluble in the solvents that the OPV is processed with, its work function (between 4.5-4.7 eV) is not near the transport energy levels of materials (2.5 – 4.3 eV LUMOs, 4.9 - 6.5 eV HOMOs) used in OPVs so it cannot easily inject charge carriers [29-33]. Another common electrode material, PEDOT:PSS, meets most of the electrode requirements, but suffers from poor conductivity. Further modification of the device structure must be made in order to have good contacts.

Electrode buffer materials are used in OPVs to modify the properties of an electrode such that a good electrical contact is formed with the device. Buffer materials are commonly alkali metal compound, oxide, organic, or composite organic-oxide, or metal-oxide based and are deposited with solution or vacuum thermal evaporation methods [34-41]. These materials

typically embody many of the characteristics of an ideal electrode and serve to modify or replace the poor characteristic of the outermost electrode. For example, since ITO has poor energy alignment with the transport levels of the active material, a buffer which has an appropriate energy level ( $\text{MoO}_3$ , PEDOT:PSS, etc.) or which modifies the work function of ITO (PEIE, self-assembled monolayer, etc.) is chosen [41,42]. Many effective buffer materials are available, but since their effects on device performance reach beyond energy level alignment, few have been fully characterized [43-45].

Organic polymer based buffer materials are particularly interesting due to the flexibility afforded to their chemical structure by synthesis. By including charged or polar moieties into their side chains, polymeric buffer materials have been able to either increase or decrease the work function of the electrode onto which they are coated [35,41,45,46]. These materials have widely varying chemical structures- some have conjugated backbones with thiophene or fluorene, or mixes of monomers, and others are entirely aliphatic. These materials also have varying effects on OPV devices; some polymer buffer materials provide great improvements in device performance while others do not [35,45]. Finally, some studies identify characteristics of the buffer structure which aid device performance, however no concrete design principles for effective buffer materials have been outlined [41,47].

Herein, we study the behavior of OPV devices in the presence or absence of different buffer layers in order to identify properties of the buffer layers which are beneficial to device operation. We investigate poor OPV device behavior evidenced by shunting or kinked current-voltage curves and present target properties for chemical design which overcome these limitations. The influences of insulating buffer thickness, of the buffer layer-active layer interaction, and of chemical control over work function modification are briefly studied. The design factors which are suggested will enable the design of future buffer materials which will be applied in high efficiency and flexible OPV devices.

## Section 2: Materials synthesis and device fabrication

All materials are used as purchased. Poly (3-hexylthiophene) (P3HT), P100 or RMI-001EE, is purchased from Rieke Metals, Poly[N-9'-heptadecanyl-2,7-carbazole-alt-5,5-(4',7'-di-

2-thienyl-2',1',3'-benzothiadiazole] (PCDTBT), SOL4280, is purchased from Solaris Chem Inc. Phenyl C<sub>61</sub>- butyric acid methyl ester (PCBM), ADS61BFA, is purchased from American Dye Source, and Phenyl C<sub>71</sub>- butyric acid methyl ester (PC70BM), 910-1500, is purchased from SES Research. ITO-coated glass, CG-50IN-S107, is purchased from Delta technologies, Ltd., All of the polymer buffer materials are purchased from Sigma Aldrich, as are MoO<sub>3</sub> and the constituent materials for the Poly(phenylene ethynylene) (PPE) buffer, as depicted in Figure 3.3. Silver pellets are purchased from Kurt J. Lesker.

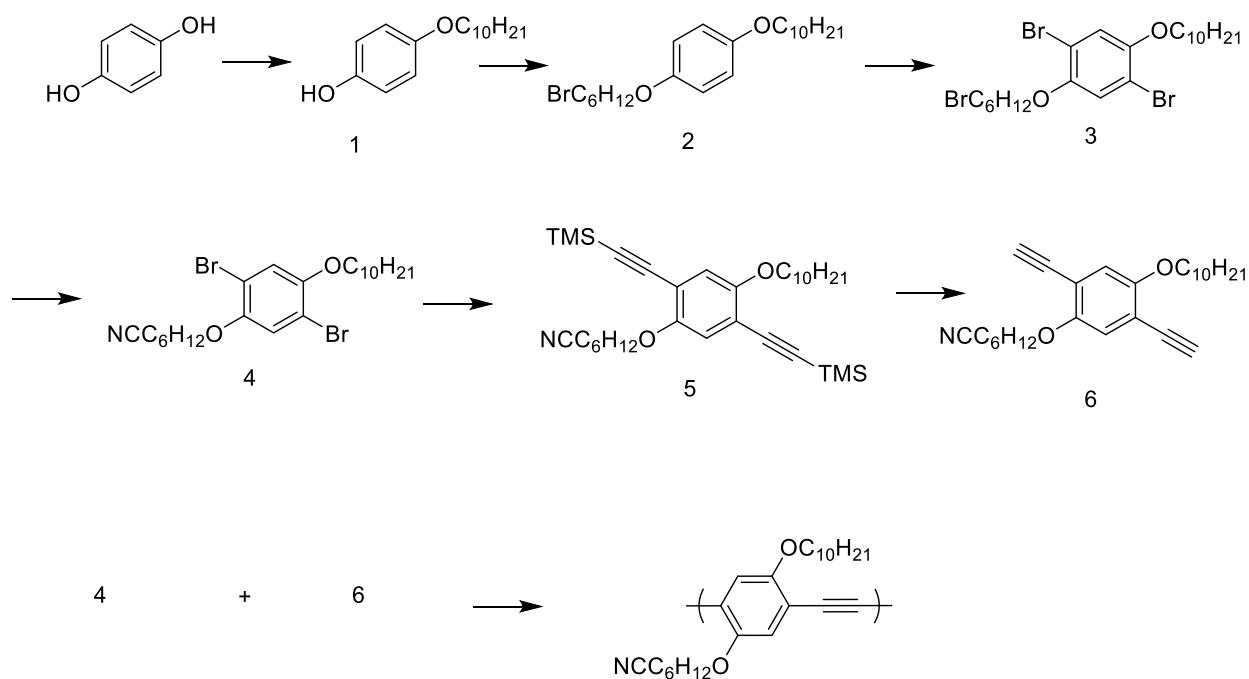


Figure 3.3: The synthetic route for producing the PPE buffer material.

**p-decyloxyphenol (1)**: Similar to Wang, et al. [48]: 1-bromodecane (8.65 mL, 0.3 eq.) was added to hydroquinone (15 g) and potassium carbonate (18.83 g, 1 eq.) in 60 mL DMF under reflux. The mixture was stirred for 2 hours, and then poured into water, extracted with diethyl ether and purified by column chromatography with 10% ethyl acetate in hexanes to get 7.4 g of **1** (73%). <sup>1</sup>H NMR (400 MHz, CDCl<sub>3</sub>, 25 °C): δ = 0.85 (t, 3 H, CH<sub>3</sub>), 1.25 (m, 12 H, CH<sub>2</sub>), 1.4 (m, 2

H, CH<sub>2</sub>), 1.75 (m, 2 H, CH<sub>2</sub>), 3.86 (t, 2 H, OCH<sub>2</sub>), 4.4 (s, 1 H, OH), 6.73 (m, 4 H, 2-H, 2'-H, 3-H, 3'-H).

**1-((6-bromohexyl)oxy)-4-decyloxybenzene (2):** Similar to He, et al. [49]: 1,6-dibromohexane (11.2 mL, 5 eq.) was added to p-decyloxyphenol (3.5 g) with potassium carbonate (3.86 g, 2 eq.) and catalytic amounts of 18-crown-6 in 85 mL acetone. The mixture was vigorously refluxed (75 °C) with stirring for 4 days. The reaction is allowed to cool, then the solvent is evaporated and the material is extracted with diethyl ether over water. Finally the product is purified by column chromatography with 10% ethyl acetate in hexanes followed by precipitation from methanol to get 5.15 g of **1** (89%). <sup>1</sup>H NMR (400 MHz, CDCl<sub>3</sub>, 25 °C): δ = 0.90 (t, 3 H, CH<sub>3</sub>), 1.29 (m, 12 H, CH<sub>2</sub>), 1.45 (m, 2 H, CH<sub>2</sub>), 1.52 (m, 4 H, CH<sub>2</sub>) 1.75 (m, 4 H, CH<sub>2</sub>), 1.9 (m, 2 H, CH<sub>2</sub>), 3.42 (t, 2 H, BrCH<sub>2</sub>), 3.91 (m, 4 H, OCH<sub>2</sub>), 6.83 (m, 4 H, 2-H, 2'-H, 3-H, 3'-H).

**1,4-dibromo-2-((6-bromohexyl)oxy)-5-decyloxybenzene (3):** Similar to Wang, et al. [48]: Bromine (1.04 mL, 2.1 eq.) is added drop-wise to compound **2** (4 g) in 30 mL dichloromethane while stirring. The reaction is stirred for 24 hours at room temperature. The excess bromine is killed with a water solution of sodium sulfite (until the reaction color changes to clear). The reaction is then poured into water and the organic material is extracted with dichloromethane. The material is purified with column chromatography to give 5.5 g (100%). <sup>1</sup>H NMR (400 MHz, CDCl<sub>3</sub>, 25 °C): δ = 0.90 (t, 3 H, CH<sub>3</sub>), 1.3 (m, 12 H, CH<sub>2</sub>), 1.45 (m, 2 H, CH<sub>2</sub>), 1.52 (m, 4 H, CH<sub>2</sub>) 1.8 (m, 4 H, CH<sub>2</sub>), 1.9 (m, 2 H, CH<sub>2</sub>), 3.42 (t, 2 H, BrCH<sub>2</sub>), 3.96 (m, 4 H, OCH<sub>2</sub>), 7.08 (m, 2 H, 2-H, 3'-H).

**7-(2,5-dibromo-4-(decyloxy)phenoxy)heptanenitrile (4):** Similar to Marshall, et al. [50]: Compound **3** (2 g) and sodium cyanide (189 mg, 1.1 eq.) are added to 30 mL DMF. The reaction is stirred for 18 hours at 60 °C. The solvent is evaporated and the reaction is washed with 0.1 N HCl followed by extraction with dichloromethane. The material is purified with column chromatography (1:1 dichloromethane in hexanes) to give 1.7 g (93%). <sup>1</sup>H NMR (400 MHz, CDCl<sub>3</sub>, 25 °C): δ = 0.85 (t, 3 H, CH<sub>3</sub>), 1.26 (m, 12 H, CH<sub>2</sub>), 1.45 (m, 2 H, CH<sub>2</sub>), 1.52 (m, 4 H, CH<sub>2</sub>) 1.7 (m, 2 H, CH<sub>2</sub>), 1.8 (m, 4 H, CH<sub>2</sub>), 2.34 (t, 2 H, NCCH<sub>2</sub>), 3.92 (m, 4 H, OCH<sub>2</sub>), 7.05 (m, 2 H, 2-H, 3'-H).

**7-(4-(decyloxy)-2,5-bis(trimethylsilyl)ethynylphenoxy)heptanenitrile (5):** Compound **4** (0.8 g), copper iodide (24 mg, 0.08 eq.), and PdCl<sub>2</sub>(PPh<sub>3</sub>)<sub>2</sub> (87 mg, 0.08 eq.) are stirred at 75° in a 25 mL of a 1:1 mix of diisopropylamine:toluene. Trimethylsilylacetylene (0.47 mL, 2.1 eq.) is added drop-wise to the mixture. The reaction is stirred for 48 hours, while monitoring by TLC (product gives a distinct blue emission on thin layer chromatography under 254 nm irradiation) and adding TMS-acetylene as needed, before cooling, filtering off precipitate and drying under vacuum. The material is purified twice with column chromatography with 10% EA in hexanes to give 0.72 g (85%). <sup>1</sup>H NMR (400 MHz, CDCl<sub>3</sub>, 25 °C): δ =0.23 (s, 18 H, TMS), 0.85 (t, 3 H, CH<sub>3</sub>), 1.25 (m, 12 H, CH<sub>2</sub>), 1.52 (m, 6 H, CH<sub>2</sub>) 1.66 (m, 2 H, CH<sub>2</sub>), 1.76 (m, 4 H, CH<sub>2</sub>), 2.34 (t, 2 H, NCCH<sub>2</sub>), 3.92 (m, 4 H, OCH<sub>2</sub>), 6.86 (m, 2 H, 2-H, 3'-H).

**7-(4-(decyloxy)-2,5-diethynylphenoxy)heptanenitrile (6):** Compound **5** (0.72 g) is added to 17 mL of a 7:10 mix of methanol:tetrahydrofuran. Potassium carbonate (457 mg, 2.5 eq) is added and the reaction is stirred at room temperature overnight. The reaction is then poured into water, extracted with diethyl ether and dried en vacuo. The material is then purified via column chromatography with 20% EA in hexanes to give 482 mg (90%) of the desired product. <sup>1</sup>H NMR (400 MHz, CDCl<sub>3</sub>, 25 °C): δ =0.88 (t, 3 H, CH<sub>3</sub>), 1.25 (m, 12 H, CH<sub>2</sub>), 1.45 (m, 2 H, CH<sub>2</sub>), 1.52 (m, 4 H, CH<sub>2</sub>) 1.68 (m, 2 H, CH<sub>2</sub>), 1.8 (m, 4 H, CH<sub>2</sub>), 2.34 (t, 2 H, NCCH<sub>2</sub>), 3.32 (s, 2 H, C≡H), 3.95 (m, 4 H, OCH<sub>2</sub>), 6.92 (m, 2 H, 2-H, 3'-H).

**Poly(2-((6-cyanoethyl)oxy)-5-decyloxyphenylene ethynylene) (PPECN) :** A conventional Sonogashira coupling polymerization reaction is used to create the PPE. In a nitrogen filled glove box, compound **4** (200 mg), compound **6** (157.6 mg, 1 eq.), copper iodide (6 mg, 0.08 eq.), and Pd(PPh<sub>3</sub>)<sub>2</sub>Cl<sub>2</sub> (21.7 mg, 0.08 eq.) are added with 10 mL of a 1:1 mix of diisopropylamine:toluene in a sealable schlenk flask. At 75 °C the reaction is then stirred for 33 hours. Finally, the reaction is cooled, filtered, and then the solvent is removed with a rotary evaporator before re-dissolving rinsing with hexanes to solidify. The material purified with soxhlet extraction to give 55 mg of the desired polymer (red solid, yellow solution with green luminescence, NMR resembles the monomers, but broadened). The molecular weight is not checked, nor is it expected to affect film forming capability.

Bulk heterojunction polymer solar cells, with a structure of ITO/buffer 1/PCBM:Polymer/buffer 2/Ag are fabricated by spincoating and vacuum thermal evaporation.

ITO glass is sonicated in isopropanol and then acetone each for 10 minutes, followed by a 10 minute UV-ozone treatment. Next, buffer 1 is spincoated in a nitrogen filled glove box to modify the electrode's work function. ITO covering buffers are commonly cast from 2 mg/mL solutions at 3000 rpm/30s and annealed at 100 °C/10 minutes, excepting PEIE which is cast from a 0.4 wt% in 2-methoxyethanol solution at 3000 rpm for 1 minute, accelerating at 1000 rpm/s [41]. The active layer is then spincoated and annealed (either P3HT:PCBM, 1:1 by weight, 10 mg polymer/mL chlorobenzene, 1000 rpm/30s, 150 °C/15 minutes or PCDTBT:PC70BM, 1:4 by weight, 1.75 wt% in 1:3 chlorobenzene:1,2-dichlorobenzene by volume, 1500 rpm/30s, 70 °C/15 minutes) [51]. Finally, the top electrode is deposited at pressures below  $5 \times 10^{-7}$  Torr; after buffer 2 (commonly 10 nm of MoO<sub>3</sub>), Ag (100 nm) is deposited through a circular shadow mask of either 1 mm in diameter.

### Section 3: Characterization methods

Photovoltaic devices are characterized with an HP/Agilent semiconductor parameter analyzer while being illuminated with simulated AM 1.5G, 1 sun light from a Newport solar simulator. The device current is normalized to the electrode mask size.

Absorption of the polymer films is measured using transmission mode in a Varian Cary 50 spectrometer. The quality of the monolayer films is observed macroscopically with an Olympus BX-51 fluorescence/optical microscope.

Work function shifts are measured using a homemade kelvin probe with an ITO reference electrode (see Appendix 1 for more details).

Cyclic voltammetry is measured with a CH instruments CHI600C potentiostat using 0.1 M tetrabutylammonium hexafluorophosphate in acetonitrile as the working electrolyte, silver nitrate as the reference electrode, and Pt wire as the counter electrode. The scans are taken at 0.1 V/s scan rates and are shifted using the onset of ferrocene oxidation (-4.80 eV). The working electrode is glassy carbon, and HOMO and LUMO values are calculated using the onset of reduction or oxidation.

X-ray photoelectron spectroscopy is measured with a Kratos Axis Ultra XPS. Scans are collected using monochromated Al  $K\alpha$  radiation at pressures below  $1E-9$  torr, using charge neutralization. Survey scans are taken with 1 eV step size and a 160 eV analyzer pass energy while fine scans are taken with 0.1 eV step size and a 20 eV analyzer pass energy.

#### Section 4: Shunting conduction pathways and electrically insulating buffer layers

Solar cells fabricated with the structure ITO/PEIE/P3HT:PCBM/MoO<sub>3</sub>/Ag provide excellent inverted device behavior. Their diode current under dark conditions (Figure 3.4) shows suppression of reverse bias leakage and good injection under forward bias. However, if either the anode (MoO<sub>3</sub>) or the cathode (PEIE) buffer layer is omitted from the device, the solar cell loses its rectifying behavior. These buffers are crucial not only to operation of the diode, but also to the power conversion process; injection under reverse and small forward bias when a buffer layer is left out overpowers photocurrent extraction (not shown).

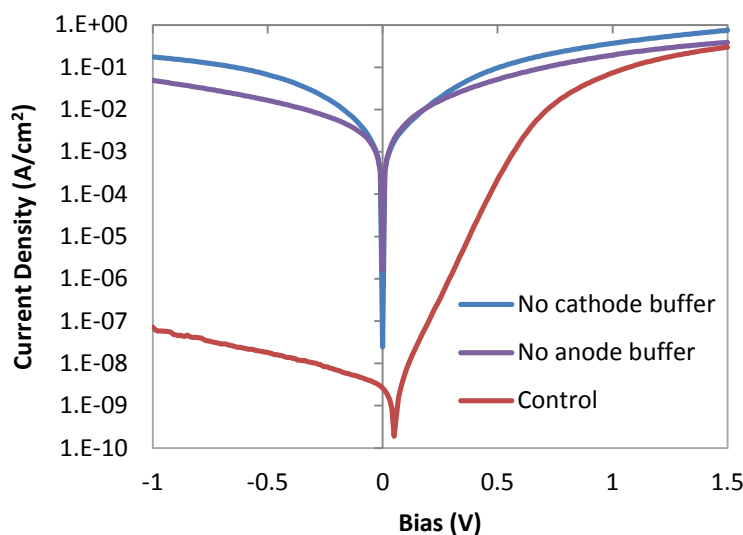


Figure 3.4: Solar cells with the structure ITO/PEIE/P3HT:PCBM/MoO<sub>3</sub>/Ag have poor dark diode curves when either buffer layer is omitted.

Reverse bias leakage current has few possible origins. Although recombination of charge carriers with electrode interface trap states (caused by a chemical reaction between the electrode

and active materials) is a plausible explanation for shunting behavior in illuminated devices, this explanation does not make sense in dark conditions when there are very few free charge carriers in the device [52]. Alternately, electrode penetration through the active materials to make short-like conduction pathways should not be possible since the active layer thickness has not changed. The most likely cause for the loss of current rectification under dark conditions is the non-selective injection of charge carriers into and through the OPV. Since a BHJ morphology allows both materials to have percolated contact between the top and bottom electrodes, non-selective injection into either material can allow charge to flow unobstructed through the device, bypassing the semiconducting diode. A planar heterojunction device, which breaks the inter-electrode contact, should not display this character.

Inverted, planar heterojunction devices can be fabricated with the structure ITO/PEIE/PCBM/P3HT/MoO<sub>3</sub>/Ag by using a contact film transfer process [10,53]. These devices prevent percolative contact of a single material in an OPV with both electrodes, but still display effective diode and photovoltaic characteristics, as shown in Figure 3.5 and Table 3.1.

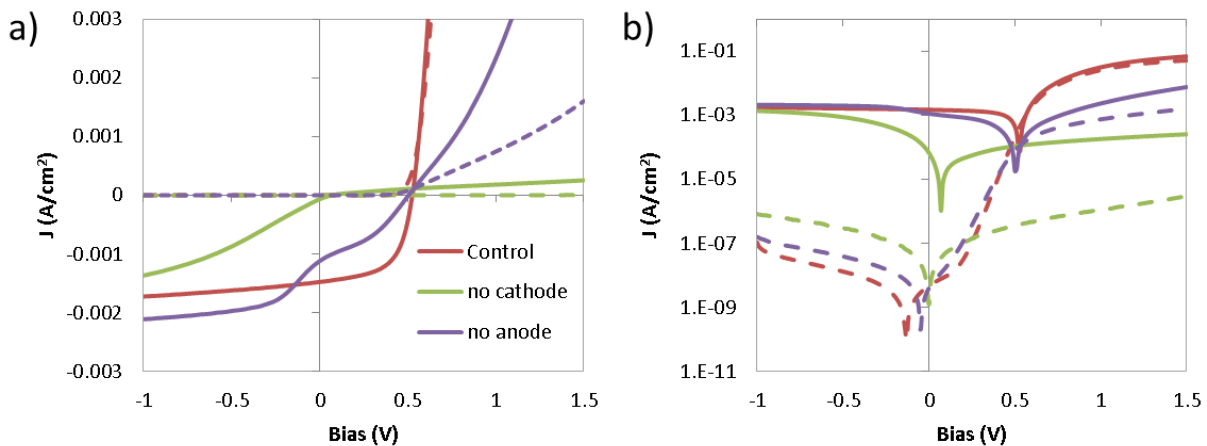


Figure 3.5: Characteristics of planar heterojunction P3HT/PCBM OPVs under illumination (solid lines) and in the dark (dashed lines) when fabricated with or without cathode or anode buffer layers. The semi-log plot, (b), shows the dark condition curves more clearly.

Table 3.1: Photovoltaic characteristics of planar heterojunction OPVs fabricated with or without buffer layers

	Control	no cathode buffer	no anode buffer
V	0.528±0.004	0.06±0.02	0.495±0.006
J (mA/cm <sup>2</sup> )	1.45±0.06	0.06±0.02	0.9±0.2
FF	54±2%	23±2%	35±2%
PCE	0.42±0.02%	0%	0.16±0.05%

The planar heterojunction device J-V curves begin to take on strange shapes once either of the buffers is removed. When the cathode buffer is removed, the dark condition curve displays an increased series resistance, in comparison to the control device, and does not have a low bias kink while the photocurrent takes on a strange double kinked shape and has an increase in reverse bias photocurrent extraction. When the anode buffer is removed, the dark condition curve displays an even greater increase in series resistance which is also evident under illumination where photocurrent can only be extracted under reverse bias. These changes in curve shape can be explained when one considers the role of the buffer in energy level alignment and its impact on carrier injection [54,55]. When a buffer layer is removed, if the innate work function of the electrode is not appropriate for injection (i.e. it presents an injection barrier), then potential is dropped as charges which cannot be injected pile up at the electrode-active layer interface. This results in strange photocurrent behavior as the electric field within the device strays from that applied externally (photocurrent falls faster than applied bias due to the faster drop of internal electric field). Differing injection barrier heights also will temper the turn-on bias of injection leading to the curve displaying a kink (no anode buffer) or not displaying a rise of injection at all (no cathode buffer, much higher barrier).

The reverse-bias dark condition curves do not greatly increase in current flow when either buffer layer is removed from the planar heterojunction device. That is to say, in spite of direct contact between an electrode and one of the active materials, and in contrast to BHJ

devices, shunting conduction pathways are not introduced. This evidence supports the idea that the buffer prevents percolative contact between the two electrodes through one of the BHJ components and thus suppresses leakage current flow.

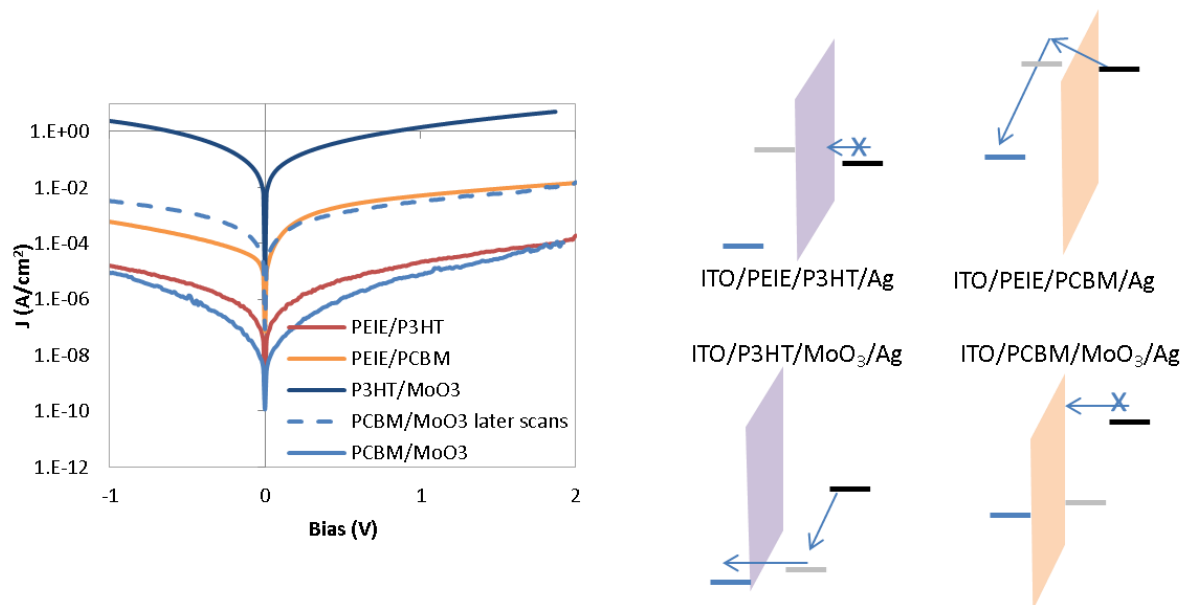


Figure 3.6: Current-voltage characteristics of single materials devices, schematically depicted to the right under reverse bias [29,32,41,56].

Direct conduction across one of the materials within a BHJ device is tested by fabricating single material devices using layer thicknesses matching the planar heterojunction devices. Four devices are fabricated; the devices structured ITO/PEIE/P3HT/Ag or ITO/PEIE/PCBM/Ag will test electron injection through the materials while the devices ITO/P3HT/MoO<sub>3</sub>/Ag and ITO/PCBM/MoO<sub>3</sub>/Ag will test hole injection. As shown in Figure 3.6, the charge conduction behavior of single material devices differs greatly depending upon the material and upon the presence and type of buffer material. Additionally, these devices do not show strongly rectifying current-voltage character. When P3HT is contacted with a relatively high work function buffer, MoO<sub>3</sub>, current can easily pass (likely hole conduction across P3HT's HOMO), but when it is contacted with PEIE, which modifies ITO to have a low work function, current is suppressed. Similarly, PCBM gives a fair amount of current when contacted with PEIE (again, likely electron conduction across its LUMO), but it does not give much current flow initially when contacted with MoO<sub>3</sub>. Although PCBM does show an increase in current after later scans when contacted

with MoO<sub>3</sub> (device burn-in likely aids the contact), this experiment shows that charge selective electrodes are needed or else charge can be carried across a device at any bias through the percolation pathways of a single material.

The main shunting conduction pathway in BHJ OPVs can be suppressed by using charge selective electrodes. Although it is well known that charge selectivity results from appropriate energy level alignment, tests with planar heterojunction devices suggest that a simple interruption of material percolation will produce charge selectivity in OPVs. Devices with the structure ITO/PEIE/P3HT:PCBM/polystyrene (PS)/Ag are fabricated by transferring PS films of different thicknesses (spincast between 750-6000 rpm from 2 mg/mL toluene solution) onto BHJ devices using a contact film transfer process. Polystyrene is a wide band gap insulator without any potential to modify the electrode work function or to carry charge. Devices made with PS anode buffer layers show a high series resistance and suppressed reverse-bias dark current, as shown in Figure 3.7.

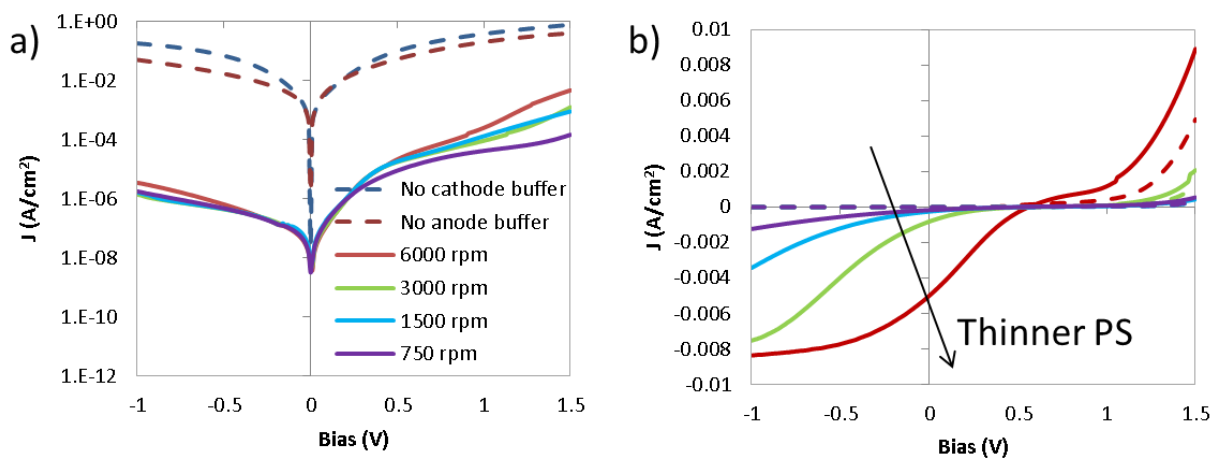


Figure 3.7: Characteristics of ITO/PEIE/P3HT:PCBM/PS/Ag devices in the dark (a) and under illumination (b). The thickness of the PS is controlled through spincasting speed variation between 750-6000 rpm.

It is notable that the dark current in reverse bias does not vary much between the different thicknesses of PS while the photocurrent varies greatly. The insulating buffer has suppressed photocurrent extraction, acting as a barrier to charge conduction, but this effect is reduced with

the thickness of the PS. Thinner PS allows for more photocurrent to pass, and a slight recovery of the normal J-V character of an OPV. However, the injection barrier presented by the PS and the poor energy alignment of the Ag electrode with the active layer prevent an easy onset of injection, leading to a kinked curve with a low fill factor. In all thicknesses probed, the insulating buffer layer suppresses the reverse bias leakage by simply breaking the direct contact of the BHJ materials with the electrode.

It is plausible to suggest that the inclusion of an insulating buffer leads to the recovery of photovoltaic behavior by simply acting as a resistor, suppressing injection under any bias, so devices with thinner insulating anode buffer layers are fabricated. Devices with the structure ITO/PEIE/P3HT:PCBM/PPECN/Ag are fabricated by transferring monolayer films of PPECN onto the active materials. Monolayers of PPECN are spread at the air-water interface and compressed to 25mN/m and films are transferred using Langmuir-Schaefer or Langmuir-Blodgett lifting. By lifting multiple monolayers, the thickness of the buffer can be controlled with finesse. Although PPECN has a conjugated backbone, its conductivity is very poor and its HOMO level (~5.6 eV) is too deep to easily inject charge onto P3HT. Finally, PPECN does not appear to affect electrode work function, so it is treated as an insulating buffer material.

Photovoltaic devices fabricated with very thin PPECN insulating buffer layers show a decrease in reverse bias leakage current and an increase in series resistance, similar to PS, and as shown in Figure 3.8.

The dependence of the OPV characteristics upon anode buffer layer thickness shows multiple trends. First, the choice of technique (LS or LB) used to increasing the thickness of the PPECN layer does not appear to influence the device behavior. As the PPECN thickness is increased to two layers, the reverse bias leakage current drops and saturates. There is also a recovery of  $J_{sc}$ ,  $V_{oc}$  and FF. At the same time, the series resistance continues to rise over the addition of six layers of PPECN and there is a drop in FF and  $J_{sc}$ ; the increase in series resistance is likely the cause for the drop in  $J_{sc}$  and FF at higher insulating buffer thicknesses. Also, just as with PS, the PPECN buffer is not work function modifying, so the poor electrode energy level alignment with the active materials leads to a later onset of injection, a kinked J-V curve (not shown) and a reduced FF, even at optimal buffer thickness.

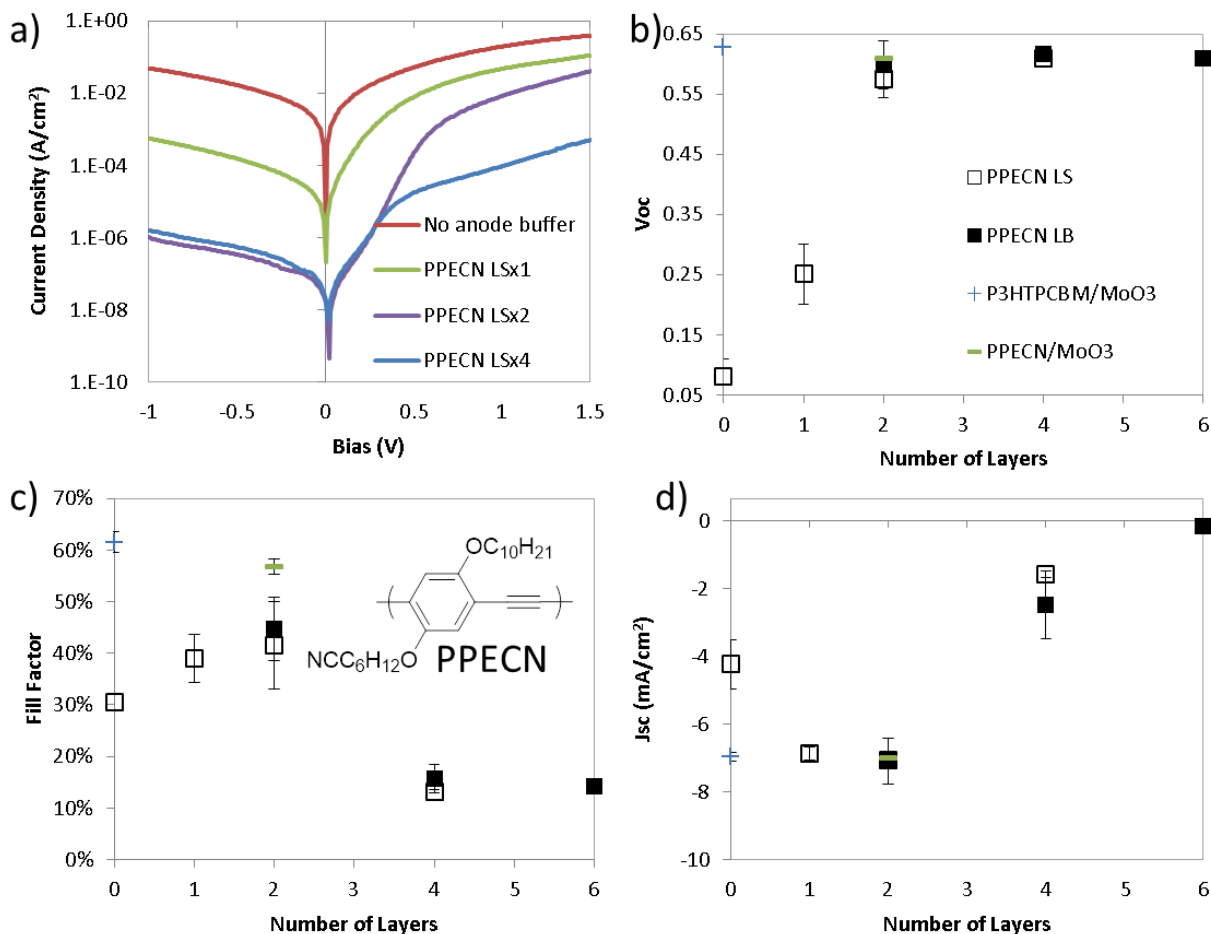


Figure 3.8: The photovoltaic behavior of ITO/PEIE/P3HT:PCBM/PPECN/Ag OPVs with multilayer PPECN insulating anode buffer layers. Dark condition current-voltage characteristics (a) dramatically change as up to six PPECN layers are added via Langmuir Schaefer (LS) lifting or Langmuir Blodgett (LB) transfer. Photocurrent behavior including  $V_{oc}$  (b) fill factor (c) and  $J_{sc}$  (d) also change.

The initial recovery of the diode rectification,  $V_{oc}$  and  $J_{sc}$  is interesting; a simple resistor which is not charge selective would suppress photocurrent extraction as well as reverse and forward bias injection. This parameter recovery suggests that the insulating buffer is likely imparting charge selectivity; as the PPECN buffer layer thickness increases and imparts charge selectivity to the electrodes, the shunting, reverse bias and low forward bias injection process is shut down. Since this shunting pathway lead to the injection of many extra carriers into the device which overpowered photocurrent production, suppression of the dark current leads to a

recovery of  $J_{sc}$  (photocurrent is now the dominant source of charge in the device at low positive and reverse bias) and  $V_{oc}$  (the point where photocurrent and injection current balance). The decrease in reverse and low forward bias dark current by five orders of magnitude, while the injection (higher positive bias dark) current only drops by about one order of magnitude is also evidence for the recovery of charge selectivity at the anode.

The design of new buffer layer materials for high performance OPVs requires that the loss routes in the device which the buffer improves are known and that the role of the buffer in mitigating this loss is understood in terms of the chemical structure of the buffer. We have shown that shunting conduction pathways, caused by non-selective charge injection and conduction across one of the components of the active material of a BHJ OPV, leads to loss of diode rectification and photovoltaic power conversion behavior. This shunting loss route is avoided by imparting charge selectivity to the electrode. Further, charge selectivity is imparted to Ag anodes by placing a thin, polymeric insulating buffer layer between the electrode and active layer. The incorporation of an insulating buffer layer seemingly provides charge selectivity by breaking the direct contact between the electrode and percolated BHJ morphology of the active layer. This finding helps justify future design of insulating electrode buffer materials for OPVs.

## Section 5: Influence of interactions between the active layer and buffer layer on device performance

Inverted OPV devices with the structure ITO/PEIE/P3HT:PCBM/MoO<sub>3</sub>/Ag have exemplary device characteristics. The PEIE and MoO<sub>3</sub> buffer layers prevent contact between the electrode and active layers and they modify the electrode work function, providing excellent charge selectivity and easy charge injection and extraction [41]. However, when the same buffer layers are applied to PCDTBT devices, as shown in Figure 3.9, the photovoltaic character is damaged and a kink appears in the current-voltage curve.

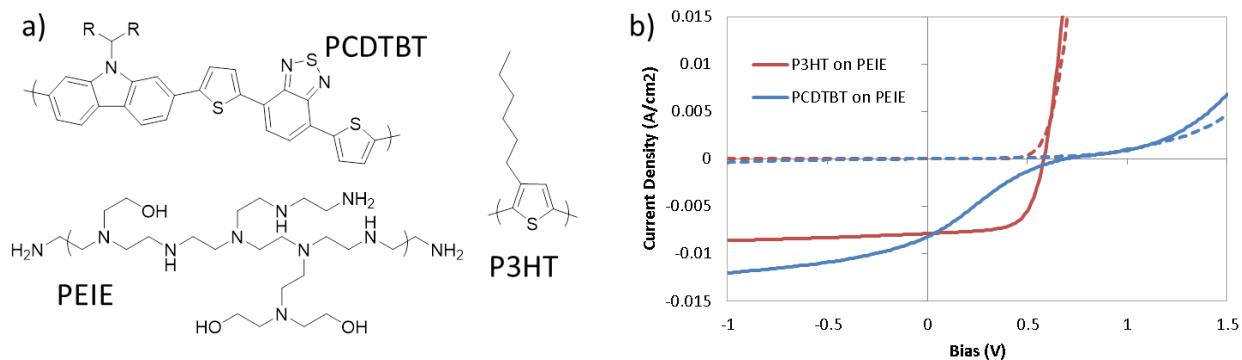


Figure 3.9: The chemical structure of PCDTBT, P3HT and PEIE (a) and the OPV characteristics of inverted P3HT and PCDTBT devices where PEIE is the cathode buffer layer (b).

Improper device morphology can critically limit photovoltaic performance. For instance, if the components of the BHJ are poorly miscible due to a mismatch in surface energy, then massive phase segregation can prevent easy exciton dissociation and charge extraction. Water contact angle is considered as a pseudo-characterization of surface energy and, as shown in Table 3.2, the values for P3HT, PCDTBT and the two PCBM's are compared.

Table 3.2: Water contact angles of P3HT, PCDTBT, PC60BM, PC70BM and PEIE

	P3HT	PCDTBT	PC60BM	PC70BM	PEIE
Water contact angle	90±4	92±2	63±2	64.6±0.6	9±1

The water contact angles of the conjugated polymers in Table 3.2 are very similar to each other (as are the fullerenes). Although the make-up of the active layer of each device contains a different mass fraction of fullerene, the similarity between the constituent material water contact angles suggests that there is not some massive chemical incompatibility within the active layer

which is causing device limiting phase separation. Indeed, many others have optimized devices and morphologies with the same active layer materials and blending ratios which are used here [51]. The difference between P3HT and PCDTBT inverted device characteristics is likely due to the buffer layer-active layer interface.

The impact of morphology on device behavior can be ruled out by making planar heterojunction devices. In this case, by making planar heterojunction PCDTBT devices the interface with the PEIE buffer is forced to be entirely PCBM. Thus, the planar device is expected to show which component of the BHJ at the buffer interface is responsible for the poor device behavior. As shown in Figure 3.10, PCDTBT and P3HT planar heterojunction devices on PEIE both have non-kinked current-voltage characteristics.

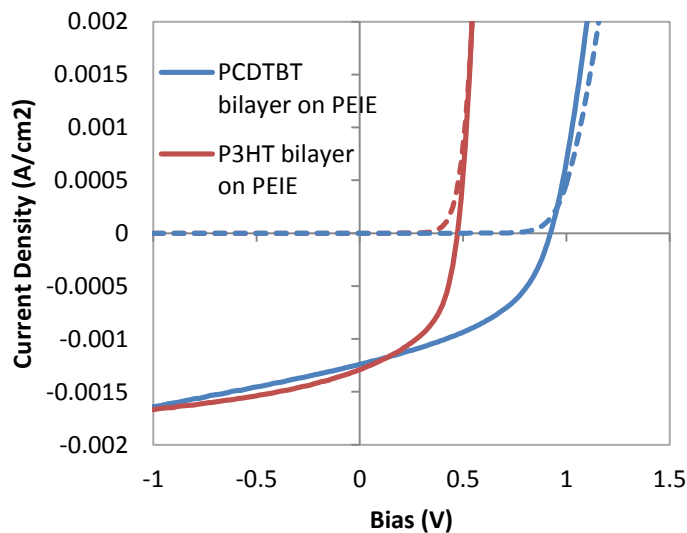


Figure 3.10: Current-voltage characteristics of planar heterojunction PCDTBT and P3HT devices.

The planar heterojunction PCDTBT devices on PEIE show that the PEIE/PCBM interface is not responsible for kinked J-V curves. This is not surprising since the P3HT planar and BHJ devices each have this same interface and they function well. Instead, it appears that the interface between PCDTBT and PEIE is responsible for the kink in the device curve. Further,

since BHJ OPVs with other conjugated polymers, such as P3HT, do not show this character and since it is known that injection barriers lead to kinked device curves we hypothesize that there is some interaction which preferentially pulls PCDTBT to the cathode buffer interface [54,55]. This vertical segregation of polymer acts as a charge extraction and injection barrier for electrons on PCBM, as shown in Figure 3.11.

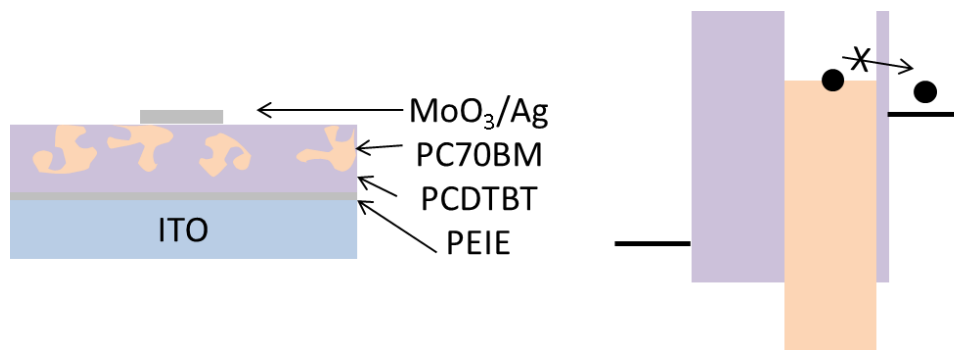


Figure 3.11: Depictions of the PCDTBT:PC70BM device structure (left) and energy level diagram (right) when PEIE is used as a cathode buffer. There is an interaction with PEIE which segregates PCDTBT to the cathode creating an electron (black circles) collection and injection barrier.

Variable angle spectroscopic ellipsometry is used to check our suspicion; by fitting ellipsometric data from a film of glass/PEIE/PCDTBT:PC70BM using previously measured optical constants for glass, PEIE, PCDTBT and PC70BM, we are able to see the surface segregation. A Cauchy model is used, along with an effective medium approximation, to fit the thickness and PCBM concentration of the film. Then, the film is modeled as two consecutive PCDTBT:PC70BM layers on glass/PEIE. This fitting method is used to approximate the thickness, if any, of a surface segregated PCDTBT layer (see Appendix 1). The PCDTBT:PC70BM film is found to be about 56 nm thick, with a PC70BM concentration of 82%, which is appropriate for the 1:4 mixing ratio. Further, fitting the thickness of a PCDTBT region of the film with 0% PC70BM near the PEIE layer gives 1.38 nm. Although this method may not quantitatively prove pure interface separation of PCDTBT, it does support our hypothesis that the interface is PCDTBT rich.

The evidence that PCDTBT is segregated to the PEIE interface is suggestive of a chemical interaction between the two materials. During spincoating, as the PCDTBT:PCBM film dries on top of the buffer, the interaction between PCDTBT and the buffer drives the formation of the morphology of the film.

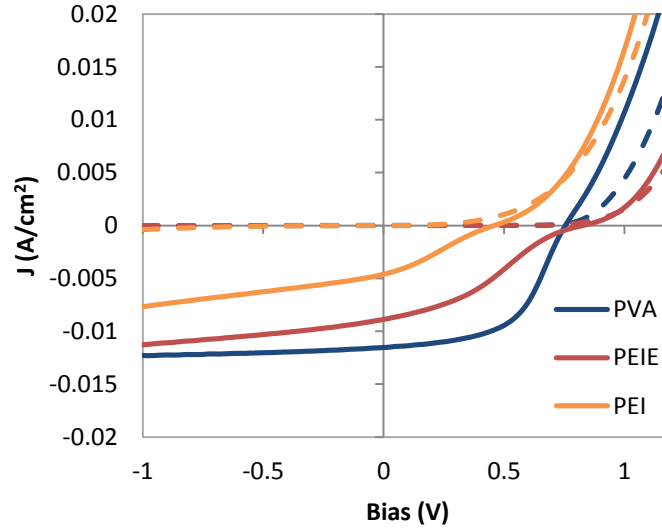


Figure 3.12: The kink in the OPV current-voltage sweep changes with changing cathode buffer in ITO/Cathode Buffer/PCDTBT:PC70BM/MoO<sub>3</sub>/Ag devices.

Table 3.3: The photovoltaic properties of PCDTBT devices with different cathode buffer layers

Cathode buffer	PEI	PEIE	PVA
V <sub>oc</sub>	0.43±0.02	0.79±0.06	0.72±0.02
J <sub>sc</sub> (mA/cm <sup>2</sup> )	4.3±0.3	8.7±0.2	11.2±0.1
FF	27±1%	32±1%	54±1%
PCE	0.51±0.06%	2.2±0.1%	4.3±0.3%

Since this interaction manifests as vertical phase separation which is detrimental to OPV function, changing the chemical character of the cathode buffer layer should lead to a change in device operation. For instance, by reducing the amount of amine functionality within the buffer by switching from poly(ethylenimine) (PEI, all amine), to poly(ethylenimine, ethoxylated) (PEIE, some of the amines have been ethoxylated and are hydroxyl terminated) to 80% hydrolyzed poly(vinyl alcohol) (PVA, no amine, mostly hydroxyl) the influence of buffer chemical structure on the PCDTBT OPV device operation can be monitored. This change alludes to changes in the active layer-buffer interaction. As shown in Figure 3.12 and Table 3.3, changing the cathode buffer from PEI to PEIE or to PVA drastically changes device performance.

As the amount of amine functionality in the cathode buffer is reduced, the kink in the J-V curve of PCDTBT devices is reduced, and the FF,  $J_{sc}$  and power conversion efficiency (PCE) all increase. Although the thickness of these insulating buffer layers is not explicitly controlled, the concentration (0.4 wt%) and spincoating rates (3000 rpm) for PEIE and PEI are held the same, and PVA (2 mg/mL) is also similar. Since the series resistances of these devices are also all very similar, we expect that buffer thickness is not limiting the performance of these devices. Rather, the differences between these devices likely stem from differences in buffer-PCDTBT interaction strength that leads to differences in vertical segregation of the active layer materials.

It appears that amine functionality has an interaction with PCDTBT. In order to characterize the interaction strength between buffers with particular functionality and PCDTBT, dissolution studies are performed. PCDTBT is spincoated upon different buffer materials, and the whole film is immersed in 1,2-dichlorobenzene (a good solvent for PCDTBT) for 10 minutes. If there is a strong buffer-PCDTBT interaction, some PCDTBT will not dissolve. The change in peak PCDTBT absorption (575 nm) strength after the solvent soak, as shown in Table 3.4, is used as a pseudo-measurement of interaction strength.

Table 3.4: Dissolution studies provide an indication of buffer-PCDTBT interaction strength—stronger interactions lead to less dissolution and greater remaining absorption strength. PEO and PVAc have some solubility in 1,2-dichlorobenzene, but this does not seem to dictate the measured dissolution

Buffer	Remaining Absorption at 575 nm
PEO	66±9%*
PEI	61±5%
Glass	58±5%
PEIE	40±8%
PEDOT:PSS	36±4%
PVA100	33±6%
PVA80	24±1%
PVAc	15±4%*

The dissolution studies corroborate the OPV device characteristics in light of the hypothesis of interaction-driven interface segregation. There is an increase in remaining PCDTBT absorption as the hydrophilicity (from poly(vinylacetate), PVAc, to 100% hydrolyzed PVA) and amount of amine functionality (from PVA to PEI) increase. This trend mirrors the device characteristics, and suggests that control over the interaction strength, through control over chemical structure of the buffer layer, leads to control over the level of interface segregation of PCDTBT in BHJ OPVs. This control can ultimately lead to control over the shape of the J-V curve.

Photovoltaic devices are fabricated with compound cathode buffer layers in order to tune the strength of the buffer-PCDTBT interaction. As shown in Figure 3.13 and Table 3.5,

PCDTBT OPVs with PVAc cathode buffer layers do not show kinked J-V curves. PVAc is spincoated at 3000 rpm from 1 mg/mL solution in DMF and, in spite of its dilution, it makes a noticeable difference on device performance in comparison to a device with no cathode buffer.

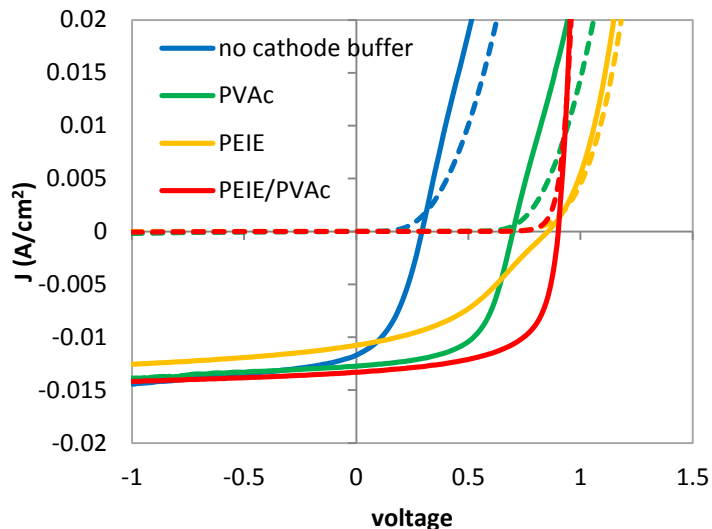


Figure 3.13: PCDTBT devices with different cathode buffer layers.

Table 3.5: Device properties of PCDTBT OPVs with different cathode buffer layers

	no cathode buffer	PVAc	PEIE	PEIE/PVAc
$V_{oc}$	$0.28 \pm 0.05$	$0.64 \pm 0.09$	$0.83 \pm 0.02$	$0.88 \pm 0.02$
$J_{sc}$ (mA/cm <sup>2</sup> )	$-11.4 \pm 0.7$	$-12.5 \pm 0.3$	$-11.0 \pm 0.8$	$-13.1 \pm 0.4$
FF	$42 \pm 2\%$	$58 \pm 3\%$	$40 \pm 1\%$	$62.7 \pm 0.7\%$
PCE	$1.4 \pm 0.4\%$	$4.6 \pm 1\%$	$3.6 \pm 0.3\%$	$7.2 \pm 0.2\%$

The inclusion of a cathode buffer layer which does not have a strong interaction with PCDTBT does not lead to unfavorable vertical phase separation in OPV devices. By placing the insulating cathode buffer, PVAc, into PCDTBT devices, the  $V_{oc}$  and  $J_{sc}$  increase, relative to a

device with no cathode buffer layer, as the onset of injection current is suppressed (see section 4). More so, since PVAc does not pull PCDTBT to the cathode interface, charge extraction is not reduced and the  $J_{sc}$  is greater than devices with PEIE cathode buffer layers. However, since PVAc does not reduce the work function of ITO the  $V_{oc}$  is limited by the built in potential (the work function difference between the electrodes is a lower potential than the active layer  $V_{oc}$ ) [57]. Previous devices with PEIE do not show a limited  $V_{oc}$ , however the interaction strength with PCDTBT is device limiting. Thus, we fabricate devices with a compound buffer layer where PVAc is spincoated on top of the PEIE, acting as a morphology directing layer which tempers the interface with PCDTBT. The compound cathode buffer layer devices show excellent behavior, displaying all of the positive characteristics of each buffer; a high  $V_{oc}$ ,  $J_{sc}$  and FF result when the cathode buffer-active layer interaction strength is appropriately controlled and its work function is appropriate for good electrical contact.

The work function of the compound buffer layer is compared to its constituent materials through kelvin probe measurements relative to ITO. As shown in Table 3.6, the work function shift caused by the compound buffer layer is similar to that of PEIE, in spite of the insulating, non-work function modifying PVAc layer on top. The work function shift measured for PEIE is similar to literature values [41].

Table 3.6: The work function change of ITO coated with different polymers, measured via kelvin probe relative to ITO. The work function of gold is taken as a calibration [58]

$\Delta$ Work Function vs. ITO	
PVAc	0
UV-O	$0.63 \pm 0.03$
PEIE	$-0.71 \pm 0.03$
PEIE/PVAc	$-0.60 \pm 0.03$
Gold	0

The design of effective buffer materials for high efficiency OPVs requires knowledge of the role of the buffer in device morphology development. We have shown that a strong interaction between a cathode buffer material (PEIE) and the hole conducting conjugated polymer (PCDTBT) in the active layer of a BHJ OPV leads to device harming segregation of the polymer to the buffer interface. This interaction appears to originate from interaction with the hydrophilic, amine functionality of PEIE, and manifests in devices as kinked current-voltage behavior due to the interfacial electron injection/extraction barrier that the polymer becomes. By placing non-interacting materials between PEIE and PCDTBT, the negative device character is repaired resulting in a high PCE. This finding helps direct the design of the chemical functionality of buffers upon which active layers for OPVs are spincoated; the choice of non-interacting buffer materials reduces the development of buffer-directed deleterious vertical phase separation.

## Section 6: Chemical structure of buffer materials for ITO work function modification

Electrode buffer materials are added to OPVs to ensure good electrical contact. Charge selective injection can be partly achieved by choosing contacts with appropriate work function alignment with the energy levels of the active materials (see Appendix 1, section 3 for some example data). Beyond charge selectivity, having appropriate work function electrodes is important because the difference in work function between the two electrodes is the built in potential of the OPV, a factor which can limit the  $V_{oc}$  if it is too small [57].

Work function is the property of the surface of a material, thus thin polymeric layers can be used to modify the work function. It has been well understood that the work function of a conducting material can be modified by the presence of a surface or interface dipole [59]. This dipole may be the result of a self-assembled monolayer, of a tightly adsorbed surface layer, or of some kind of chemical reaction with the surface [59]. Many work function modifying polymers have been synthesized, usually with acid-like, base-like or electrolyte functionality, and applied to OPVs, giving mild to significant improvement in PCE. In spite of this, identification and explanation of the functionality and mechanism which enables polymers to modify the work function of a conductor are not clear. Many different polymers are potential work function

modifiers, as shown in Figure 3.14, including anionic and cationic polyelectrolytes, neutral polymers with polar functionality, acid like-polymers and base-like polymers.

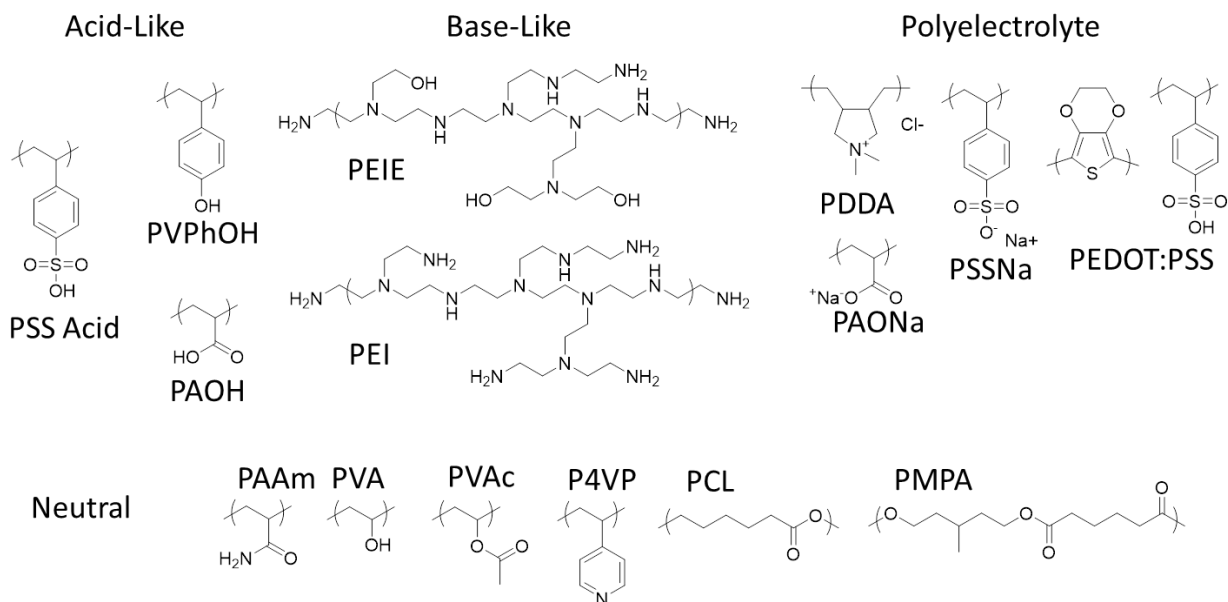


Figure 3.14: Chemical structures of candidate buffer materials for ITO work function modification include poly(styrenesulfonic acid) (PSS Acid), poly(vinylphenol) (PVPPhOH), poly(acrylic acid) (PAOH), PEIE, PEI, poly(diallyldimethyl ammonium chloride) (PDDA), poly(acrylic acid) sodium salt (PAONa), poly(4-sodium styrenesulfonate) (PSSNa), PEDOT:PSS, poly(acrylamide) (PAAm), PVA, PVAc, poly(4-vinylpyridine) (P4VP), poly(caprolactone) (PCL), and poly(3-methyl-1,5-pentanediol adipate) (PMPA).

The shift in ITO work function is measured relative to an ITO reference using a homebuilt kelvin probe (see appendix 1, section 4). In comparison to literature results, some modifiers have predictable work function shifts: base like functionality seems to reduce the work function while acid like functionality seems to increase the work function, as listed in Table 3.7. Polymers which have neutral polar moieties do not induce changes in the ITO work function (not shown in the table). Unlike literature results, no polyelectrolytes show a change in the work function of ITO, even the commonly cited PEDOT:PSS blend [41, 47]. More surprisingly, PVA, which is not expected to be greatly charged in solution, shows a work function reduction if cast from DMF, as do many neutral, ester containing polymers when cast onto base (NaOH). Finally, acidic or basic moieties which are outside of an active pKa range when cast, such as PAA or

P4VP, cannot easily be induced to produce a work function shift, even when cast from solution of different pH, or when cast onto acid or base.

Table 3.7: Work function shift of ITO due to polymer modifier

$\Delta$ WF relative to ITO			
Base-like		Neutral	
PEI	-0.82±0.01	PVA80 (from DMF)	-0.23±0.01
PEIE	-0.72±0.03		
Neutral cast on Base			
Acid-like		NaOH/PVAc	-0.42±0.01
PAOH	0.30±0.02	NaOH/PCL	-0.54±0.03
PVPhOH	0.27±0.05	NaOH/PMPA	-0.46±0.02
PSS Acid	0.36±0.01	NaOH/PVA80	-0.63±0.02

Literature explanations of the origin of spincoated polymer-based ITO work function shifts usually rely on models where a charge on the polymer sets up a dipole with the substrate [35,47,60,61]. In this explanation, it is reasonable that polyelectrolytes do not produce work function shifts: the presence of a counterion provides a charge-neutral character to the film. It is even possible to explain the difference in work function due to conjugated polyelectrolyte films as originating from Fermi level alignment instead of charging based dipole formation [62]. However, literature models usually rely on an acid or base reaction with substrate surface hydroxyl groups, which results in an interface dipole which modifies the ITO work function

[41,47]. This description, while plausible for base-like polymers (which should de-protonate the surface hydroxyl), is not an entirely intuitive explanation for work function modification by acid-like or ester containing polymers.

The role of surface functionality in work function modification is investigated by alkylsilane modifying the ITO surface. Vapor-based deposition of n-dodecyltrimethoxy silane provides monolayer, inert alkyl functionalized blocking of the surface hydroxyl groups of ITO. If work function modification of ITO relies upon chemistry with surface hydroxyl groups, then we expect to see no work function shift in the silane treated samples. When acid- or base-like polymers (PAOH and PEIE) are spincoated onto the treated ITO surface, the work function still displays a shift, as listed in Table 3.8.

Table 3.8: The work function shift of ITO, relative to ITO, when treated with an alkylsilane (C12) and subsequent polymer deposition

ITO Substrate	$\Delta WF$ vs ITO
C12	0.19±0.03
C12/PEIE	-0.37±0.02
C12/PAOH	0.28±0.01

Silane treating the surface of ITO results in work function modification. The increase in work function which occurs after silane treatment may be due to the formation of the SiO-like oxide surface since an oxidized material is expected to have more tightly bound electrons. Spincoating onto the hydrophobic alkylsilane surface is a challenge: the methoxyethanol and water from which PEIE and PAOH are cast do not wet the surface well, nevertheless, the work function shift after casting indicates that some material was deposited. When PEIE is cast onto the silane treated ITO, the work function is reduced by about 0.56 eV relative to the silane treated surface. This number is in line with the 0.7 eV work function reduction that PEIE

produces on ITO. Further, when PAOH is cast onto silane treated ITO, it provides a small work function increase of about 0.09 eV, possibly due to the poor film quality. This means that reaction with the surface hydroxyls is not the sole source of work function modification.

The mechanism for polymer mediated work function modification, as proposed by Schlapak, et al., potentially involves a dipole between a spincoated polymer with a net charge and the resulting counter-charge which accumulates in the conducting substrate [63]. This picture is counterintuitive on two counts. First, it is not clear how a polymer which is charged in solution would maintain its charge upon spincoating. Proton exchange with a high dielectric constant (20-80), protic solvent can easily provide a net charge to a solvated polymer, however, during drying the polymer and solvent counter ion should recover their original charge neutral state as the dielectric constant of the medium (1-10) becomes dominant in the mix [64-66]. Second, even if a charged polymer is deposited, it is not clear that the substrate will respond with an accumulation of charge that results in a work function modifying dipole.

The impact of charged polymer deposition on work function modification of ITO is investigated via electrophoretic deposition of polyelectrolytes. Solutions containing 2 mg polymer per mL water of PEIE, PDDA and PSS are introduced to an electrochemical reactor with an ITO working electrode, a Pt wire counter electrode and a Ag/AgCl reference electrode. A steady state potential is applied for 5 minutes to allow the charged polymer separate from its counterion, migrate through the solution and deposit onto the oppositely charged ITO substrate, as shown in Figure 3.15. In spite of being unable to produce work function shifts from spincoating, PSS and PDDA films are able to produce large shifts in the ITO work function when electrophoretically deposited.

PSS, PDDA and PEIE films deposited under different electrophoretic potentials show differences in the work function shift relative to ITO. It is expected that the charged substrate during electrophoretic deposition attracts charged polymer, which maintains this state after drying. Different applied potentials likely attract different amounts of charged polymer, resulting in films with different thickness and different polymer-to-substrate dipoles. These dipoles are the proposed origin of the work function shift of the electrophoretically deposited films. When PSS and PDDA films are spincoated at different thicknesses, however, the counterion is deposited along with the polymer resulting in no net dipole. Further, the charge used to attract the film only

produces work function shifts when it is large and opposite that of the functionality of the polymer in solution. This is consistent with the model that the polymer is depositing due to substrate charge, and that it is remaining charged after drying.

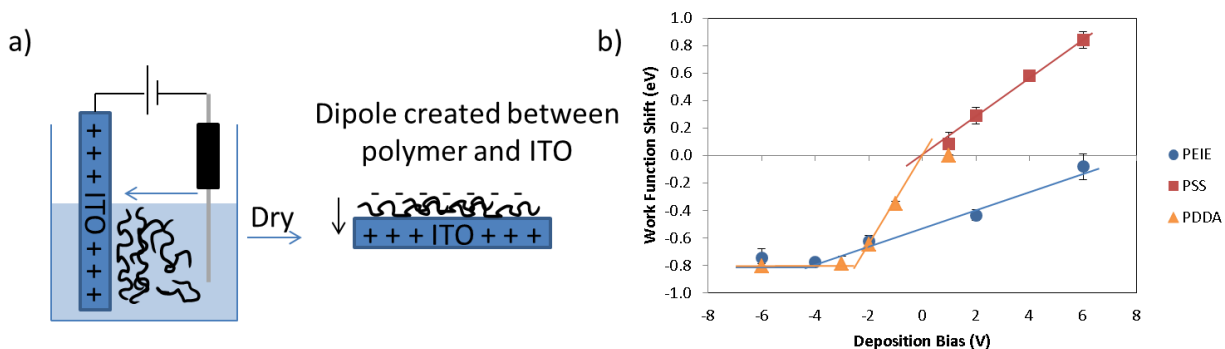


Figure 3.15: Depiction of electrophoretic deposition, (a), of PDDA, PSS and PEIE onto ITO. The charged films produce shifts in the ITO work function (b).

Electrophoretic deposition of PEIE is very different from that of PSS and PDDA. PEIE has been reported to have strong adsorption strength with substrates [41]. Thus, at large negative bias, PEIE (cationic in solution due to its amine functionality) predictably deposits thick charged films which produce large reductions in work function shifts. As the potential is increased, however, the work function reduction is not cut off very quickly; PEIE deposits films even under a repelling positive bias, likely due to the strong tendency for surface adsorption. After all, PEIE is capable of depositing charged films under spincoating conditions to give work function reductions [41]. These findings support the hypothesis that polymer films act as work function modifiers by maintaining charge after deposition onto substrates.

Next, changes in substrate character are observed via x-ray photoelectron spectroscopy. As shown in Figure 3.16 and in Appendix 1, section 5, the XPS spectra of ITO, UV-ozone treated ITO (24 hours prior to measurement) and PAOH and PEIE coated ITO are different. First, each of the chemical species of PEIE and PAOH can be assigned to peaks fitted to the carbon and oxygen XPS spectra. Also, the polymer films are thin enough that the oxygen and indium peaks of ITO show through. It is notable that the structure of PEIE is drawn with ether

bonds in Figure 3.16; this change is made in order to assign the extra oxygen and carbon XPS peaks and is consistent with the unselective ethoxylation of chain ends.

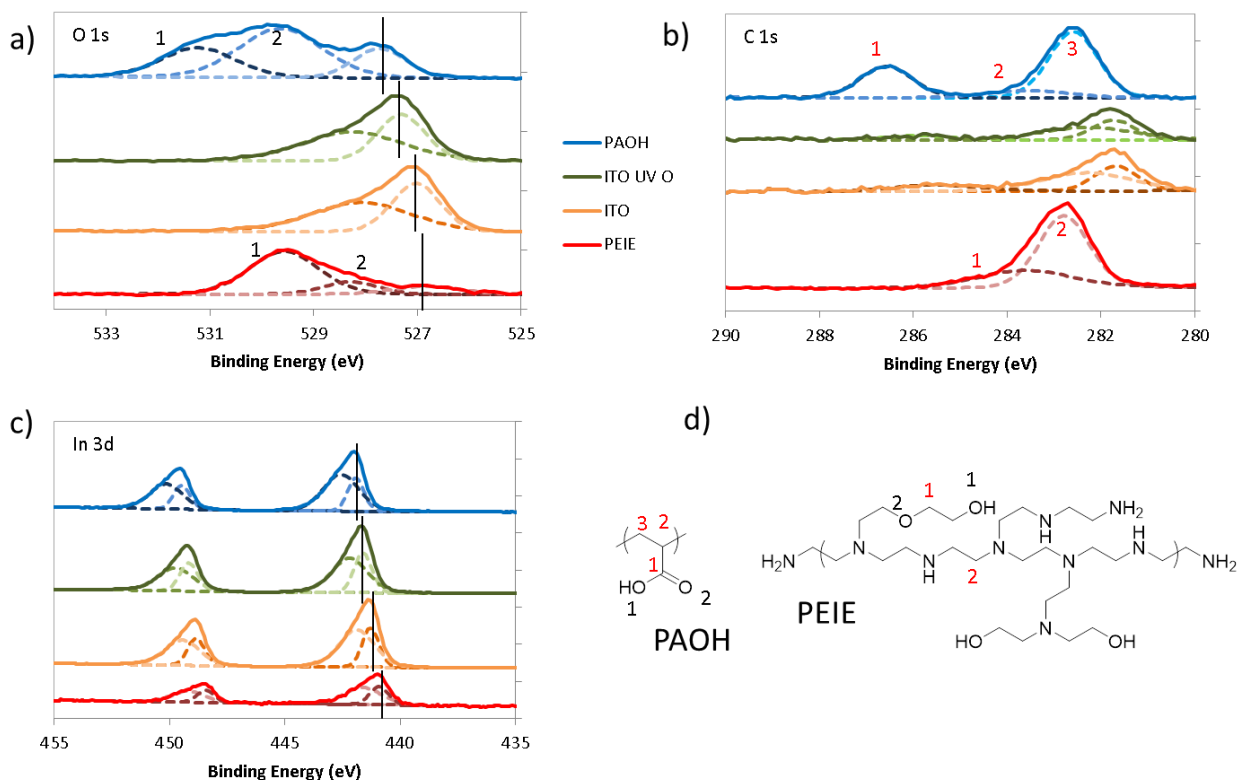


Figure 3.16: XPS spectra of oxygen (a), indium (c), and carbon (b) binding energy regions of work function modifying polymers, PAOH and PEIE (d), cast onto ITO.

The shifts in the oxygen and indium peaks in the XPS spectra of PEIE and PAOH coated ITO are consistent with substrate charging in response to the polymer film. When PAOH is cast onto ITO (or when ITO is UV-ozone treated), there is a shift to higher binding energy of the indium and oxygen peaks, oppositely, PEIE gives a shift to lower binding energy. This is in contrast to the carbon contamination peaks on ITO and UV-ozone treated ITO which do not shift relative to each other, suggesting that the indium and oxygen peak shifts are indicative of a material change rather than an instrumentation or measurement error. The work function shifts are explained with the following model: when work function modifying polymer is deposited onto the substrate, its charge induces a redistribution of charge in the ITO. This redistribution of charge produces work function shifts. For instance, negatively charged PAOH produces a

positive charge (reduction in electron density) near the surface of ITO. This reduction in electron density leaves remaining electrons more tightly bound to the atomic cores, producing a shift in the XPS signal. PEIE is similar (but opposite), and UV-ozone treated ITO gives a similar shift due to surface cleaning and oxidation [59,67]. Thus, the XPS data is also consistent with the model where charged polymers create a dipole with an oppositely charged substrate resulting in work function modification.

More work is still required in order to fully explain how polymers act as work function modifiers. For instance, it is still not intuitive that a spincoated polymer, charged in solution, can lose its counterion during drying to maintain charge. Also, it is not clear why ester containing polymers are able to reduce the work function of ITO when cast onto NaOH. However, it is clear that work function modification can be achieved through the deposition of charged polymers, enabled by acid- or base-like functionality, which induces a counter charge in the substrate and sets up a surface-normal oriented dipole. This work motivates the design of insulating polymer-based electrode buffer layers with polar functionality for work function modification.

## Section 7: Design rules for electrode buffer layers

Electrode buffer layers are necessary for highly efficient OPVs. These layers provide charge selectivity to devices with BHJ morphologies by acting as a physical barrier between the active layer and the electrode, preventing the formation of shunting conduction pathways. Buffer materials also provide charge selectivity by modifying the electrode work function, through charged acid- or base-like moiety-to-charged substrate dipoles, to provide good alignment with the charge carrier transport energy levels of the active layer materials. Charge selective electrodes enable effective charge injection and extraction from the devices, helping devices maintain rectifying behavior and helping achieve high fill factor,  $V_{oc}$  and  $J_{sc}$ . Further, effective electrode buffer materials do not interfere with morphology development, through control over the buffer-active material interaction strength, further enabling high fill factor and PCE. These design rules will help enable the design of electrode buffer layers for high efficiency OPVs.

## Section 8: References

1. G. Li, R. Zhu, Y. Yang, *Nat. Photonics*, 6 153-161 (2012).
2. D. Qian, W. Ma, Z. Li, X. Guo, S. Zhang, L. Ye, H. Ade, Z. Tan, J. Hou, *J. Am. Chem. Soc.*, 135, 8464-8467 (2013).
3. Z. Henson, K. Mullen, G. Bazan, *Nat. Chem.*, 4 699-704 (2012).
4. H. Zhou, L. Yang, W. You, *Macromolecules*, 45 607-632 (2012).
5. L. Dou, J. Gao, E. Richard, J. You, C. Chen, K. Cha, Y. He, G. Li, Y. Yang, *J. Am. Chem. Soc.*, 134 10071-10079 (2012).
6. E. Zhou, K. Tajima, C. Yang, K. Hashimoto, *J. Mater. Chem.*, 20 2362-2368 (2010).
7. C. Cabanetos, A. Labban, J. Bartelt, J. Douglas, W. Mateker, J. Frechet, M. McGehee, P. Beaujuge, *J. Am. Chem. Soc.*, 135 4656-4669 (2013).
8. K. Vandewal, W. Oosterbaan, S. Bertho, V. Vrindts, A. Gadisa, L. Lutsen, D. Vanderzande, J. Manca, *App. Phys. Lett.*, 95 123303 (2009).
9. C. Chu, H. Yang, W. Hou, J. Huang, G. Li, Y. Yang, *App. Phys. Lett.*, 92 103306 (2008).
10. A. Tada, Y. Geng, Q. Wei, K. Hashimoto and K. Tajima, *Nat. Mater.* 10, 450 (2011).
11. S. Menke, W. Luhman, R. Holmes, *Nat. Mater.*, 12 152-157 (2013).
12. H. Tseng, H. Phan, C. Luo, M. Wang, L. Perez, S. Patel, L. Ying, E. Kramer, T. Nguyen, G. Bazan, A. Heeger, *Adv. Mater.*, DOI: 10.1002/adma.201305084 (2014).
13. D. Credginton, F. Jamieson, B. Walker, T. Nguyen, J. Durrant, *Adv. Mater.*, 24 2135-2141 (2012).
14. K. Vandewal, Z. Ma, J. Berqvist, Z. Tang, E. Wang, P. Henriksson, K. Tvingstedt, M. Andersson, F. Zhang, O. Inganas, *Adv. Funct. Mater.*, 22 3480-3490 (2012).
15. D. Di Nuzzo, G. Wetzelaer, R. Bouwer, V. Gevaerts, S. Meskers, J. Hummelen, P. Blom, R. Janssen, *Adv. Energy Mater.*, 3 85-94 (2013).
16. N. Giebink, B. Lassiter, G. Wiederrecht, M. Wasielewski and S. Forrest, *Phys. Rev. B* **82** 155306 (2010).
17. F. Krebs, J. Fyenbo and M. Jørgensen, *J. Mater. Chem.* 20, 8994 (2010).
18. E. Bundgaard, O. Hagemann, M. Manceau, M. Jorgensen, F. Krebs, *Macromolecules*, 43 8115-8120 (2010).
19. H. J. Park, M.-G. Kang, S. H. Ahn and L. J. Guo, *Adv. Mater.* 22, E247 (2010).
20. M. Kim, J. Kim, J. Cho, M. Shtein, L. Guo, J. Kim, *App. Phys. Lett.*, 90 123113 (2007).
21. C. Tang, *App. Phys. Lett.*, 48 183-185 (1986).
22. J. Lee, K. Vandewal, S. Yost, M. Bahlke, L. Goris, M. Baldo, J. Manca, T. Voorhis, *J. Am. Chem. Soc. Comm.*, 132 11878-11880 (2010).
23. D. Coffey, B. Larson, A. Hains, J. Whitaker, N. Kopidakis, O. Boltalina, S. Strauss, G. Rumbles, *J. Phys. Chem. C*, 116 8916-8923 (2012).
24. B. Rolczynski, J. Szarko, H. Son, Y. Liang, L. Yu, L. Chen, *J. Am. Chem. Soc.*, 134 4142-4152 (2012).
25. G. Yu, J. Gao, J. C. Hummelen, F. Wudl, A. J. Heeger. *Science*. 270, 1789-1791 (1995).

26. D. Vithanage, A. Devizis, V. Abramavicius, Y. Infahsaeng, D. Abramavicius, R. C. I. MacKenzie, P. Keivanidis, A. Yartsev, D. Hertel, J. Nelson, V. Sundstrom, V. Gulbinas, *Nat. Comm.*, 4 2334 (2013).
27. P. E. Shaw, A. Ruseckas, I. D. W. Samuel. *Adv. Mater.* 20, 3516-3520 (2008).
28. R. Lunt, J. Benziger, S. Forrest, *Adv. Mater.*, 22 1233-1236 (2010).
29. Y. Park, V. Choong, Y. Gao, B. Hsieh, C. Tang, *App. Phys. Lett.*, 68 2699-2710 (1996).
30. M. C. Scharber, D. Mühlbacher, M. Koppe, P. Denk, C. Waldauf, A. J. Heeger, C. J. Brabec. *Adv. Mater.* 18, 789-794 (2006).
31. Y. He, H. Chen, J. Hou, Y. Li, *J. Am. Chem. Soc.*, 132 1377-1382 (2010).
32. B. Rand, D. Burk, S. Forrest, *Phys. Rev. B*, 75 115327 (2007).
33. E. Ratcliff, B. Zacher, N. Armstrong, *J. Phys. Chem. Lett.*, 2 1337-1350 (2011).
34. R. Po, C. Carbonera, A. Bernardi, N. Camaioni, *Energy Environ. Sci.*, 4 285-310 (2011).
30. V. Shrotriya, G. Li, Y. Yao, C. Chu, Y. Yang, *App. Phys. Lett.*, 88 073508 (2006).
31. Z. Liang, Q. Zhang, O. Wiranwetchayan, J. Xi, Z. Yang, K. Park, C. Li, G. Cao, *Adv. Funct. Mater.*, 22 2194-2201 (2012).
32. J. Liu, S. Shao, G. Fang, B. Meng, Z. Xie, L. Wang, *Adv. Mater.*, 24 2774-2770 (2012).
33. S. H. Park, A. Roy, S. Beaupré, S. Cho, N. Coates, J. S. Moon, D. Moses, M. Leclerc, K. Lee, A. J. Heeger. *Nat. Photonics*. 3, 297-303 (2009).
34. Y. Zhou, H. Cheun, W. Potscavage, C. Fuentes-Hernandez, S. Kim, B. Kippelen, *J. Mater. Chem.*, 20 6189-6194 (2010).
35. L. Chen, C. Xie, Y. Chen, *Org. Elect.*, 14 1551-1561 (2013).
36. Z. He, C. Zhang, X. Xu, L. Zhang, L. Huang, J. Chen, H. Wu, Y. Cao, *Adv. Mater.*, 23 3086-3089 (2011).
37. K. O'Malley, C. Li, H. Yip, A. Jen, *Adv. Energy Mater.*, 2 82-86 (2012).
38. J. Sun, Y. Zhu, X. Xu, L. Lan, L. Zhang, P. Cai, J. Chen, J. Peng, Y. Cao, *J. Phys. Chem. C*, 116 14188-14198 (2012).
39. K. Zilberberg, A. Behrendt, M. Kraft, U. Scherf, T. Riedl, *Org. Electronics*, 14 951-957 (2013).
40. S. Liu, K Zhang, J. Lu, J. Zhang, H. Yip, F. Huang, Y. Cao, *J. Am. Chem. Soc.*, 135 15326–15329 (2013).
41. Y. Zhou, C. Fuentes-Hernandez, J. Shim, J. Meyer, A. Giordano, H. Li, P. Winget, T. Papadopoulos, H. Cheun, J. Kim, M. Fenoll, A. Dindar, W. Haske, E. Najafabadi, T. M. Khan, H. Sojoudi, S. Barlow, S. Graham, J.-L. Brédas, S. Marder, A. Kahn and B. Kippelen, *Science* 336, 327 (2012).
42. S. Khodabakhsh, B. Sanderson, J. Nelson, T. Jones, *Adv. Funct. Mater.*, 16 95-100 (2006).
43. X. Guo, N. Zhou, S. Lou, J. Smith, D. Tice, J. Hennek, R. Ortiz, J. Navarrete, S. Li, J. Strzalka, L. Chen, R. Chang, A. Facchetti, T. Marks, *Nat. Photonics*, 7 825-833 (2013).
44. R. Xia, D. Leem, T. Kircharts, S. Spencer, C. Murphy, Z. He, H. Wu, S. Su, Y. Cao, J. Kim, J. deMello, D. Bradley, J. Nelson, *Adv. Energy Mater.*, 3 718-723 (2013).

45. Z. He, C. Zhong, X. Huang, W. Wong, H. Wu, L. Chen, S. Su, Y. Cao, *Adv. Mater.*, 23 4636-4643 (2011).
46. Z. Tang, M. Andersson, Z. George, K. Vandewal, K. Tvingstedt, P. Heriksson, R. Kroon, M. Andersson, O. Inganäs, *Adv. Mater.*, 24 554-558 (2012).
47. J. Lee, H. Kang, K. Lee, *Adv. Energy Mater.*, DOI: 10.1002/aenm.201301226, (2014).
48. L. Wang, K. Li, H. Lin, *Polymer*, 51 75-83 (2010).
49. F. He, Y. Tang, M. Yu, S. Wang, Y. Li, D. Zhu, *Adv. Funct. Mater.* 17 996-1002 (2007).
50. W. Marshall, T. Goodson, G. Cullinan, D. Swanson-Bean, K. Haisch, L. Rinkema, J. Fleisch, *J. Med. Chem.* 30 682-689 (1987).
51. J. Moon, J. Jo, A. Heeger, *Adv. Energy Mater.*, 2 304-308 (2012).
52. J. Kim, Z. Guan, A. Shu, A. Kahn, Y. Loo, *Langmuir*, 27 11265-11271 (2011).
53. D. Bilby, J. Amonoo, M. Sykes, B. Frieberg, B. Huang, J. Hungerford, M. Shtein, P. Green, J. Kim, *Appl. Phys. Lett.* **103** 203902 (2013).
54. W. Tress, K. Leo, M. Riede, *Adv. Funct. Mater.*, 21 2140-2149 (2011).
55. W. Tress, O. Inganäs, *Sol. Energy Mater. & Sol. Cells*, 117 599-603 (2013).
56. K. Sugiyama, H. Ishii, Y. Ouchi, K. Seki, *J. App. Phys.* 87 295-298 (2000).
57. M. Lo, T. Ng, T. Liu, V. Roy, S. Lai, M. Fung, C. Lee, S. Lee, *App. Phys. Lett.* 96 113303 (2010).
58. W. Osikowicz, M. de Jong, S. Braun, C. Tengstedt, M. Fahlman, W. Salaneck, *App. Phys. Lett.*, 88 193504 (2006).
59. S. Braun, W. Salaneck, M. Fahlman, *Adv. Mater.*, 21 1450-1472 (2009).
60. W. Lee, J. Seo, H. Woo, *Polymer*, 54 5104-5121 (2013).
61. B. Lee, I. Jung, H. Woo, H. Shim, G. Kim, K. Lee, *Adv. Funct. Mater.*, 24 1100-1108 (2014).
62. P. Chia, S. Sivaramakrishnan, M. Zhou, R. Png, L. Chua, R. Friend, P. Ho, *Phys. Rev. Lett.*, 102 096602 (2009).
63. R. Schlapak, D. Armitage, N. Saucedo-Zeni, G. Latini, H. Gruber, P. Mesquida, Y. Samotskaya, M. Hohage, F. Cacialli, S. Howorka, *Langmuir* 23 8916-8924 (2007).
64. R. Sengwa, K. Kaur, *Polym. Int.*, 49 1314-1320 (2000).
65. K. Singh, P. Gupta, *Eur. Polym. J.*, 34 1023-1029 (1998).
66. O. Yano, Y. Wada, *J. Polym. Sci.*, 9 669-686 (1971).
67. W. Song, S. So, D. Wang, Y. Qiu, *App. Surface Sci.*, 177 158-164 (2001).

## Chapter 4: Conjugated polymer alignment in photovoltaic devices

Organic electronic devices continue to attract research attention due to their constituents' tunable properties and their promise of flexible electronics [1-7]. Conducting polymers, for instance, are strongly absorbing, semiconducting materials which are solution processable. Although these materials do not provide devices with high enough efficiencies for commercialization, their chemical and processing dependent properties continue to advance towards practicality [8].

The charge carrier mobility of conducting polymers is believed to be a device limiting property in polymer solar cells (PSCs) and in polymer thin film transistors (TFTs). In PSCs, the relatively low charge carrier mobility leads to a compromise between device absorption and charge collection as the film thickness is optimized near 100 nm [9,10]. Furthermore, precise thickness control on the 100 nm scale during mass production could be challenging. There are, however, a few examples of high mobility polymers used in PSCs where simultaneously good film morphology allowed the device to take on a much thicker dimension without suffering. For instance, Peet, et al., Li, et al., and Murphy, et al., have applied polymers with hole mobilities around  $10^{-2}$  to  $10^{-1}$   $\text{cm}^2\text{V}^{-1}\text{s}^{-1}$  and were able to have well-functioning devices with thicknesses in the range of 370-600 nm [11-13]. While the peak efficiency of the aforementioned devices was not achieved in the thickest films, these results provide motivation for the development of high mobility conducting polymers for PSCs.

Routes to fabricate conjugated polymer films with high charge carrier mobility may be readily accessible through morphology control. Conducting polymers are highly anisotropic since their structure potentially has three unique packing dimensions. As shown in Figure 4.1, the plane-like strand that is a conjugated polymer backbone will have different molecular orbital overlap along the different packing dimensions associated with the structure. This difference in orbital overlap acts as the decisive factor in determining connectivity between chains and can

ultimately rule the transport properties of the film. First, conducting polymers are necessarily solution processable so they are synthesized with bulky side chains which limit contact between polymer backbones near the side chain. This side chain inhibited distance is usually 1-3 nm, and is the largest of the packing dimensions [14-16]. Second, these side chains may have a bulky presence outside of the plane of the polymer backbone, limiting plane to plane packing; the  $\pi$ - $\pi$  stacking distance, usually 0.3-0.4 nm, may still present a barrier to transport [14-16]. Third,  $\pi$ -conjugated covalent bonds along the backbone of the polymer provide great interconnectivity between orbitals and present a relatively smaller transport barrier. This anisotropy means that polymer orientation and morphology can greatly influence charge carrier mobility.

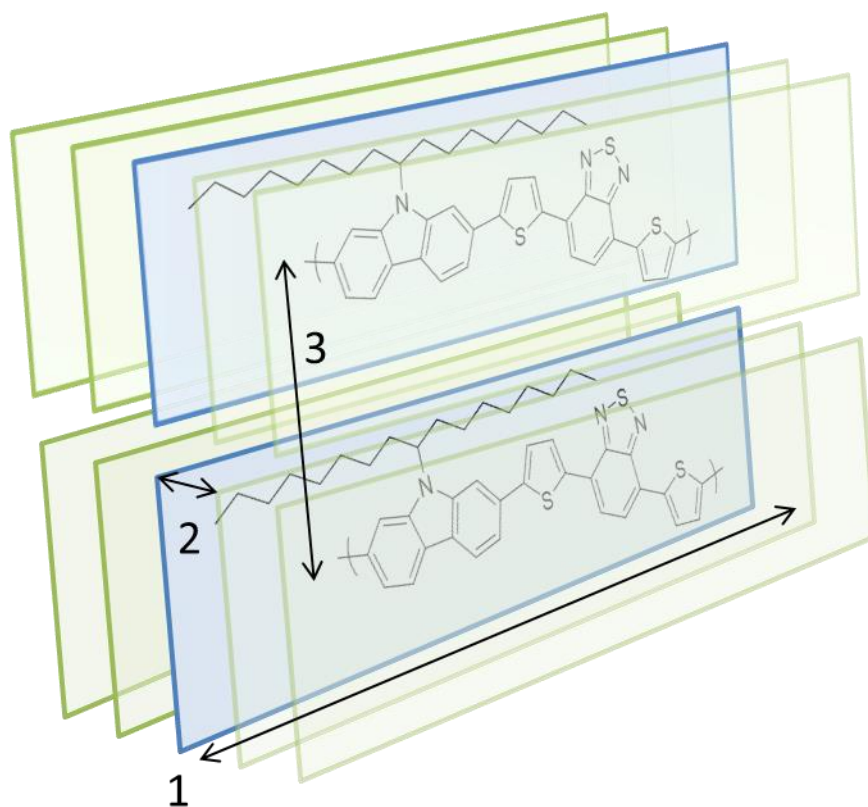


Figure 4.1: Depiction of the inter-polymer packing in an idealized semicrystalline conjugated polymer. The conjugated polymer is idealized as a planar, ribbon like rectangle where the polymer backbone lies in the rectangle's longest planar direction. Charge carrier mobility is faster along the directions with greater pi orbital overlap, increasing from directions  $3 < 2 < 1$ .

Control over conjugated polymer orientation, and therefore charge carrier mobility, is difficult. Substrate interactions may rule the morphology of a conjugated polymer film, and the charge carrier mobility is thusly thickness dependent. For instance, Huang et al., found that thin (80 nm) poly(3-hexylthiophene) (P3HT) films have primarily edge on polymer stacking relative to the substrate, providing an out-of-plane hole mobility of  $10^{-4} \text{ cm}^2\text{V}^{-1}\text{s}^{-1}$  which is limited by the large inter-chain distance [17]. However, as the film was increased to 1000 nm in thickness, the fraction of polymer chains with face-on orientation relative to the substrate increased, and since this orientation has greater pi-orbital overlap within the out-of-plane transport direction, the hole mobility increased to  $10^{-3} \text{ cm}^2\text{V}^{-1}\text{s}^{-1}$  [17]. The substrate-interaction can be used advantageously in PSC fabrication. Kim, et al., found that if P3HT was stamped with an AAO membrane, the substrate interaction between the AAO walls and P3HT caused the polymer to take an edge-on orientation relative to the AAO walls and a face-on orientation relative to the substrate [18]. This resulted in an increased hole mobility in the primary transport direction in the PSC, and an increase in efficiency relative to the non-imprinted device. These devices, however, still perform worse than conventional bulk heterojunction (BHJ) PSCs.

Control over polymer orientation and spacing offer routes for manipulation of the in-plane charge carrier mobility. For instance, by synthetically changing the length and branching point of semiconducting polymer side chains, the pi-pi stacking distance may be changed affecting the hole mobility in TFTs [19]. Alternately, synthetically controlling the interplay between planarization, entanglement and aggregation via molecular design enables control over morphology during film drying. If an appropriately designed conjugated polymer is sheared during drying, the polymer can align with the shear, leading to significant increases in mobility (by two orders of magnitude compared to an unaligned film) [20]. Finally, processing routes, such as capillary confinement into a microchannel or spincoating control over shear force can lead to molecular ordering in plane which gives very high charge carrier mobility in TFTs [21,22].

In-plane alignment is not ideal for PSCs because their primary carrier transport direction is out of plane. Also, although there have been some reports of improved PSC efficiency due to increased charge carrier mobility, there are too many other factors associated with BHJ morphology to directly tie the improvements to mobility. Since polymer alignment is a direct

route to enhance the charge carrier mobility of PSCs, but out of plane alignment is not easily accessible, in-plane planar heterojunctions are candidate device architectures with which to investigate the influence of polymer mobility on device behavior. As shown in Figure 4.2, in-plane planar heterojunction devices rely upon both in- and out of plane charge carrier transport and do not have a complicated BHJ morphology which will convolute device data interpretation.

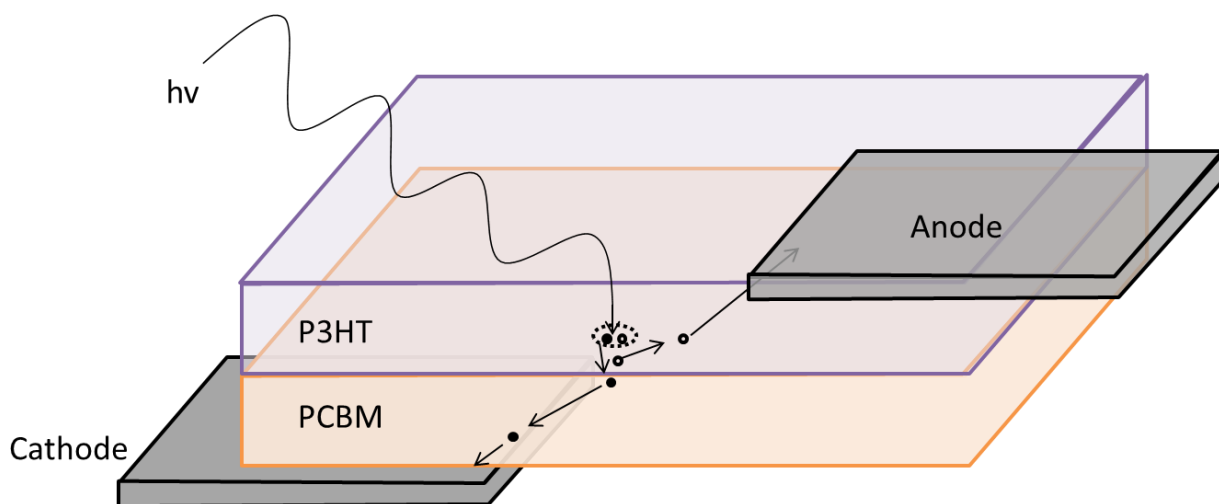


Figure 4.2: A cutaway schematic of an in-plane planar heterojunction PSC. The charge transport pathways are significantly more dependent upon in-plane mobility than traditional thru-plane devices. Holes are represented by open circles on P3HT and electrons on PCBM by closed circles.

In-plane planar heterojunction devices will allow for direct observation of the influence of molecular orientation and charge carrier mobility on PSC efficiency. The bilayer device provides a planar heterojunction with a well-defined interface between the electron donor and acceptor materials, independent of changes to the polymer alignment and mobility (although it may be dependent upon polymer orientation relative to the acceptor). Therefore the exciton splitting dynamics are controlled separately from film morphology. Also, the in-plane electrodes require charge to be transported in-plane in order to be extracted, exacerbating the influence of charge carrier mobility in devices.

In this chapter, the alignment of P3HT films is optimized via spincoating with an epitaxially directing additive. The optical and photoluminescent characteristics are measured, and the films are applied as donor layers in planar heterojunction PSCs. The early device results

show unintuitive dependencies upon polymer orientation relative to the transport direction and provide motivation for further investigation.

## Section 2: Device fabrication and characterization.

In-plane planar heterojunction devices are fabricated using a combination of previously-developed methods. The planar heterojunction is fabricated using a contact film transfer (CFT) method [23]. Briefly, rectangular Al electrodes of 2 mm x 5 mm x 30 nm are deposited using vacuum thermal evaporation. A cathode modifying buffer, PEIE, is spincoated at 3000 rpm for 60s from 0.4 wt% methoxyethanol solution [24]. Then, PCBM (30 mg/mL chlorobenzene) is spincoated at 1000 rpm for 60s followed by a 15 minute anneal at 150 °C. A P3HT film is then transferred onto the PCBM from a sacrificial glass/PSS (10 wt% H<sub>2</sub>O, 4000 rpm for 30s) substrate by placing the two films cofacial and dissolving away the PSS with water. Finally, a staggered upper crossbar electrode is deposited as MoO<sub>3</sub> (10 nm)/Ag (100 nm). The P3HT films are cast from chlorobenzene (8.24 mg/mL, 1000 rpm for 30s) or chlorobenzene, 1,3,5-trichlorobenzene (TCB) mixes at differing rates in order to direct alignment epitaxially [25]. As shown in Figure 4.3, an off-center spincoating technique is adopted in order to get macroscopic alignment of the epitaxially aligned polymer films [22]. Transfer of the aligned P3HT films onto devices allows for direct control over the orientation of the polymer relative to the direction of carrier transport between the electrodes.

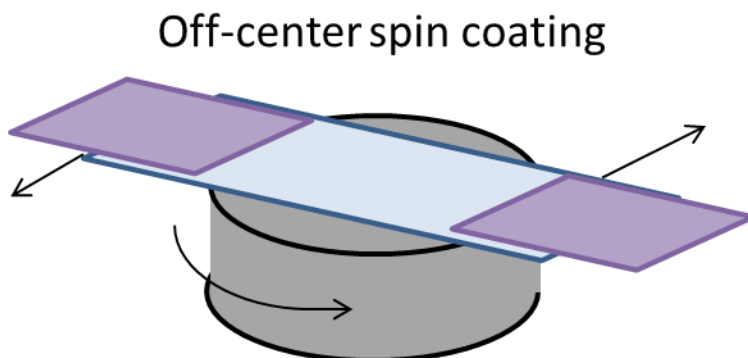


Figure 4.3: A depiction of off-center spincoating: by placing solution covered substrates (purple) away from the axis of rotation, the shear force on the liquid at constant spin speed is more uniaxial (normal to the spin axis) than if the substrate was on center.

Polarized optical microscopy (Olympus BX-51) is used to observe alignment, morphology and device size. ImageJ software is used to measure the transport length between the electrodes. Photoluminescence anisotropy is observed with steady state, monochromated illumination from a halogen lamp in a PTI QuantaMaster photoluminescence spectrophotometer. Excitation of P3HT films at 470 nm with polarized light produces emission between 550-900 nm, measured with a photodetector and monochromator. The anisotropy of emission is observed after turning the sample relative to the excitation so that polarization effects of the reflection-type monochromators are unimportant. Absorption anisotropy is observed with a Varian Cary 50-bio spectrophotometer in transmission mode. Samples are held at constant location while polarized light is shined upon them. By taking a new baseline for each polarizer orientation, the influence of instrument polarization is accounted for.

Photovoltaic devices are characterized with an HP/Agilent semiconductor parameter analyzer while being illuminated with simulated AM 1.5G, 1 sun light from a Newport solar simulator. The device current is not normalized to the electrode mask size, since the in-plane device current is not necessarily proportional to the electrode size.

### Section 3: Bulk heterojunction control devices

The in-plane planar heterojunction PSC architecture is quite novel, and so is the use of long-scale aligned conjugated polymers in PSCs. In order to learn about the influence of epitaxially aligned P3HT on device performance, BHJ, thru-plane transport PSCs are fabricated. Devices with the structure ITO/PEIE/P3HT:PCBM/MoO<sub>3</sub>/Ag are fabricated by spincoating P3HT:PCBM (1:1, 10 mg P3HT/mL CB, 10 vol% TCB) solutions at 400 rpm for 30s, then 1000 rpm for 30 seconds followed by a 15 minute anneal at 150 °C. The absorption of the PSCs, as shown in Figure 4.4, shows that the samples spun with TCB have optical anisotropy.

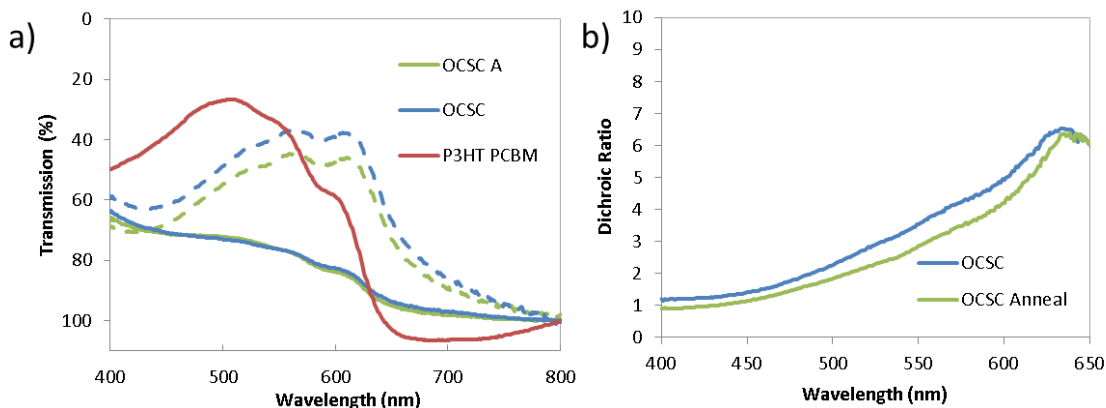


Figure 4.4: Absorption characteristics of P3HT:PCBM BHJ PSCs cast with TCB (under differing light polarization) or without TCB (a). The samples with TCB are spin casted off center (OCSC), and annealed afterwards. The dichroic ratio, (b), is the ratio of the absorption under differing polarizer orientations- a characterization of alignment.

The optical anisotropy, and dichroic ratio of about 5 decreases to about 4.5 upon annealing, however the sample remains aligned. It is notable that in the aligned direction, the absorption near 610 nm, corresponding to the inter-chain absorption of P3HT, is relatively stronger than that of the regular film, indicating better ordering [26-28].

Photovoltaic devices fabricated with epitaxially aligned P3HT:PCBM film morphologies do not function well, as shown in Figure 4.5.

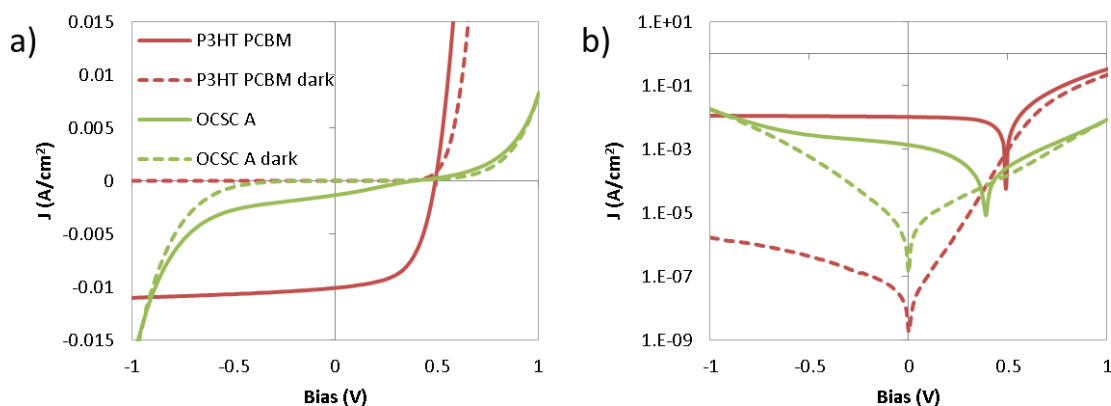


Figure 4.5: Thru-plane PSC current-voltage curves (a) for off-center spin cast P3HT:PCBM blends aligned with TCB. The OCSC devices perform much worse than the control, with non-rectifying dark current shown in the semi-log plot (b).

When the aligned P3HT:PCBM blend is applied in PSCs, the rectifying behavior of the diode is lost. The annealed film, however, is better than the non-annealed film which acted as a short circuited device. Additionally, there appears to be a problem extracting charge, since the photocurrent is large under negative bias but begins to fall well before injection, which also has a late onset, begins. The alignment results in devices with significantly lower open circuit voltage ( $V_{oc}$ ), short circuit current density ( $J_{sc}$ ), fill factor (FF) and power conversion efficiency (PCE). However, the anisotropic absorption imparted by the alignment allows the OCSC device to give different  $J_{sc}$  under aligned ( $0.40 \pm 0.04 \text{ mA/cm}^2$ ) and anti-aligned illumination ( $0.30 \pm 0.05 \text{ mA/cm}^2$ ) whereas the control device provides no difference ( $2.96 \pm 0.14$  vs  $2.89 \pm 0.17 \text{ mA/cm}^2$ ).

Tapping mode AFM images, as in Figure 4.6, reveal that the aligned P3HT:PCBM film has a very fibrous, very rough morphology.

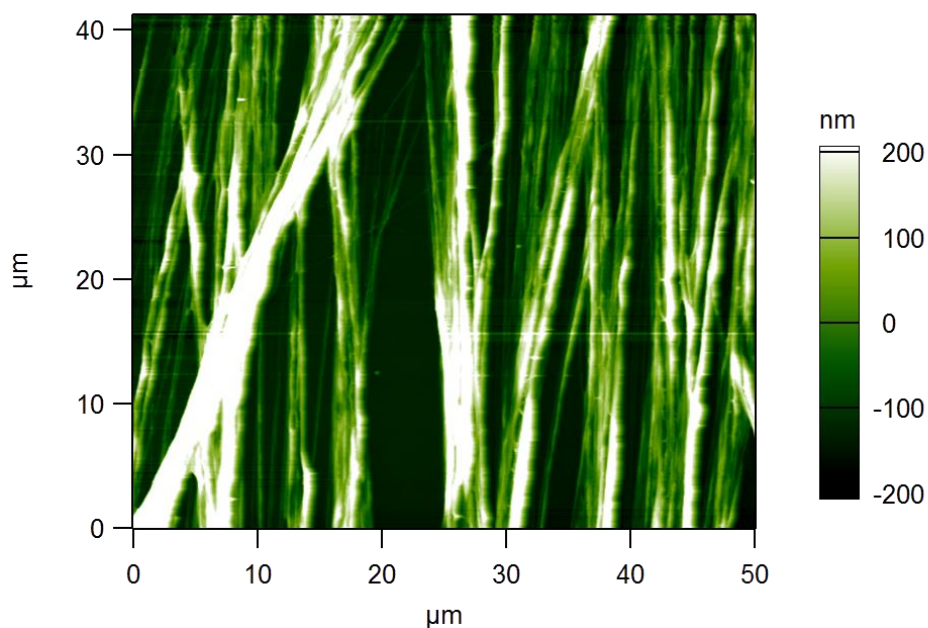


Figure 4.6: Tapping mode AFM reveals a very rough fibrous microstructure for OCSC P3HT:PCBM blends cast with TCB.

The fibrous film has a thickness between the fibers of 10-20 nm, corresponding to the thickness of the PEIE buffer, and a thickness over 300 nm on the fibers. This is in contrast to the control device which has a thickness near 100 nm, typical of conventional BHJ PSCs. This result explains the poor device behavior: ignoring the fact that a good BHJ morphology has not been confirmed to exist within the aligned fibers, the rough morphology was too thick on the active

material for effective cross-fiber (thru-plane) charge carrier transport. Additionally, there is likely direct contact between the top electrode buffer and the bottom electrode buffer, allowing for direct charge transport along this shunting pathway through the device.

These BHJ control devices with aligned P3HT:PCBM fibers provide an indication of expected results and complications in in-plane planar heterojunction devices. The thickness and roughness of TCB aligned P3HT films may prove to be device limiting characteristics in spite of the good polymer backbone alignment.

#### Section 4: Optimization of in-plane P3HT alignment

The TCB concentration in P3HT solution in chlorobenzene is changed in order to optimize the polymer alignment as characterized by the dichroic ratio. As the amount of TCB in solution is changed from 2, 4, 6, 8 and 10 volume percent, the dichroic ratio at 610 nm varies from 3.3, 5.1, 3.3, 4.0 and 4.5, peaking at 2 volume percent. Although there was a lot of variation within the samples, stemming from poor control over the nucleation and growth of the P3HT fibrils, the 2 volume percent sample is further optimized by varying the spincoating speed from 200, 300, 400, 500 and 600 rpm for 30 seconds. The absorption of aligned P3HT fibrils has a very interesting shape; absorption along the fiber alignment direction has sub-band gap features which are dependent upon spincoating speed, as shown in Figure 4.7. Identification of the origin of these features is beyond the scope of optimizing the polymer alignment, and although this feature is coincident with the wavelengths of photoluminescence, this absorption feature is possibly due to the structure. The sub-gap feature is not present in absorption perpendicular to the fibers, thus the peak dichroic ratio is in the near infrared (near 820 nm).

Anisotropy in the photoluminescence is not nearly as strong as in absorption, as shown in Figure 4.8. The peak dichroic ratio of 2-3, appears around 630 nm in the excitation and emission scans, near the band edge of P3HT. Additionally, the excitation and absorption spectra show much stronger peaks near the 610 nm aggregation peak of P3HT, indicating greater ordering. The extra peak in the excitation at about 470 nm is from a peak in the spectrometer lamp emission. Finally, the fact that the shapes of the normalized emission spectra overlap so well indicates that the emissive chromophore is independent of the alignment and ordering in the film;

there is little motivation for energy migration to the polarized species [29]. The alignment independent chromophore, whose emission has overlap with the scattering absorption band in one alignment direction, may account for the lower dichroic ratio in photoluminescent measurements.

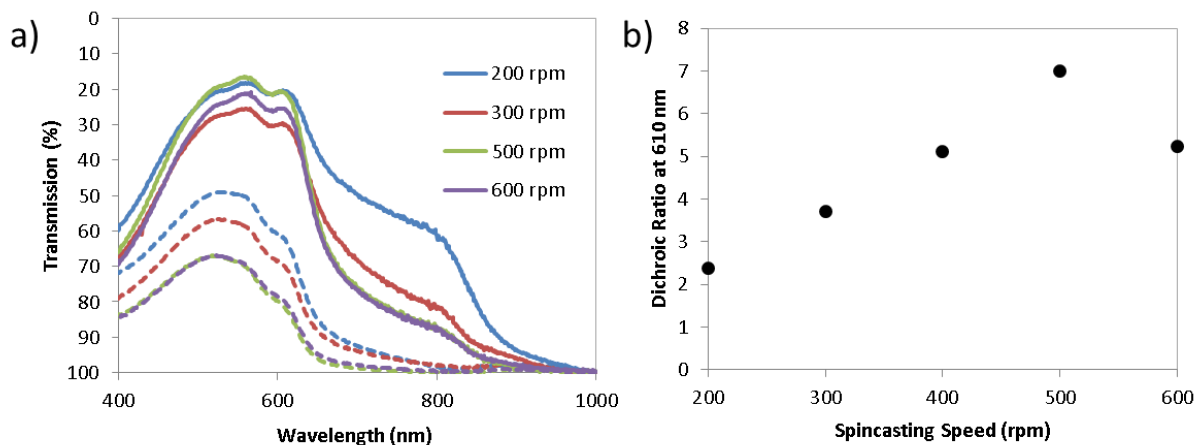


Figure 4.7: The absorption of aligned P3HT fibers shows interesting sub-band gap scattering beginning at 900 nm along the alignment direction but not against it (a). This leads to a very high peak dichroic ratio (not shown). However, the dichroic ratio in wavelengths where P3HT absorbs is closer to 8 (b) (one sample for each rpm).

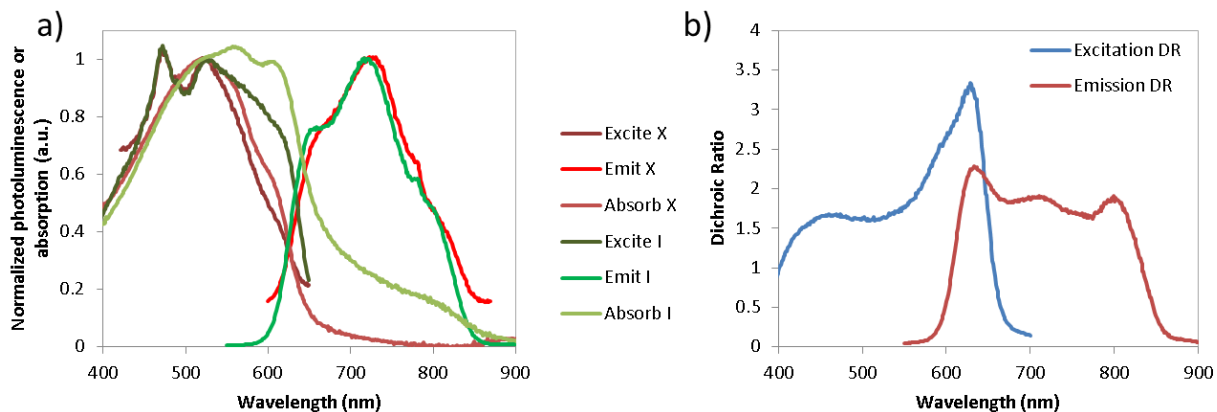


Figure 4.8: The normalized absorption, excitation and emission spectra of aligned P3HT fibers cast at 500 rpm (a). Absorption, emission and excitation are all larger along the polarization (I) than perpendicular to it (X), however the photoluminescent dichroic ratio, (b), is between 2-3.

Optical microscopy reveals centimeter scale alignment as well as the same type of fiber like morphology observed in the P3HT:PCBM blends, as shown in Figure 4.9. The samples appear to be well aligned, however, while turning the polarizer resulted in large differences in the visible color of the film, the emissive intensity did not seem to depend greatly upon polarization, further supporting the idea that the emissive chromophore is not alignment sensitive.

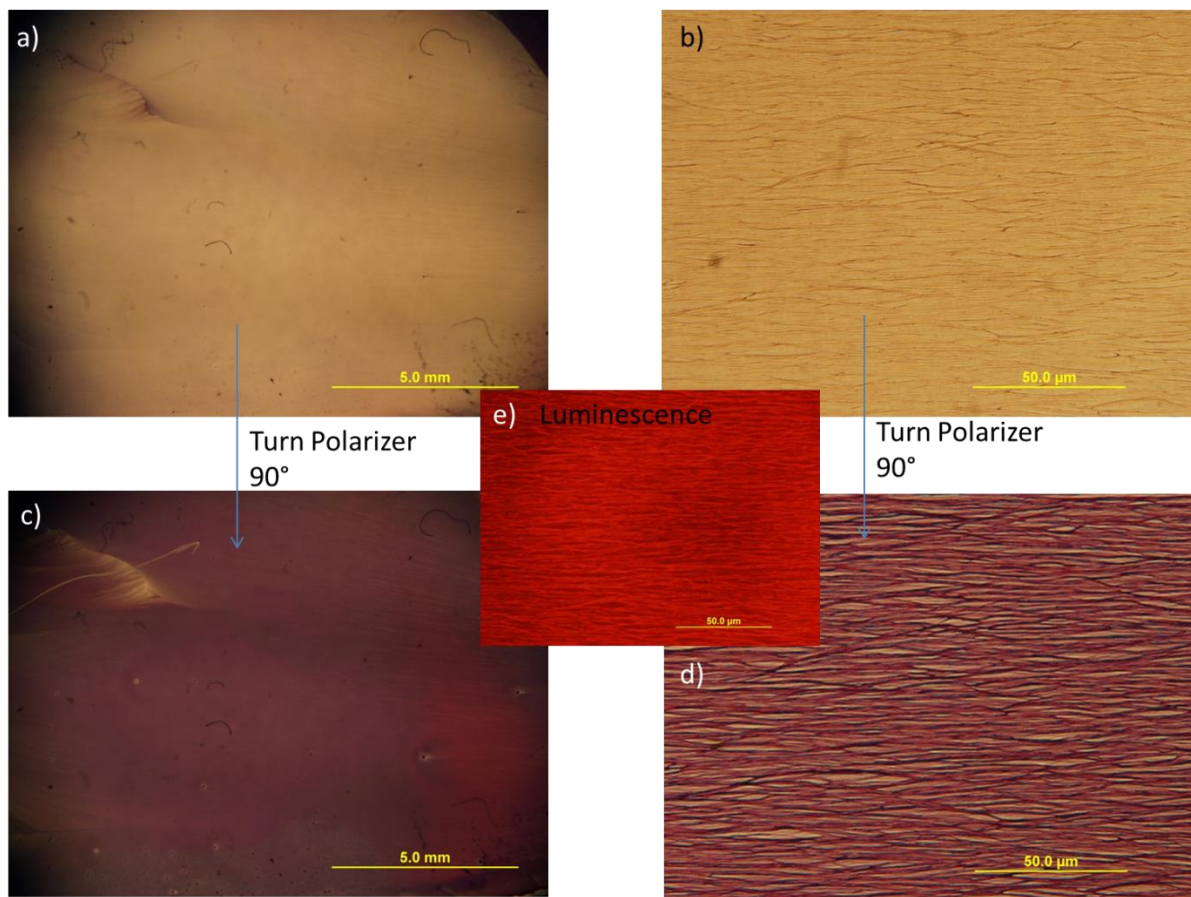


Figure 4.9: Polarized optical (a-d) and photoluminescent (e) microscopy of P3HT cast with TCB reveal centimeter scale alignment and fiber like morphology with non-polarized emission (turning the polarizer did not greatly change the emission strength).

## Section 5: In-plane planar heterojunction photovoltaic devices

The well aligned P3HT films were then applied to in-plane planar heterojunction test-of-concept devices. These devices have not been thickness optimized in control samples, however,

the influence of alignment is still expected to be present. As shown in Figure 4.10, the absorption of the aligned and unaligned films before and after assembly appears similar to the optimized P3HT films. After assembly, the absorption spectra appear as superimpositions of the constituents, suggesting that no great intermixing is occurring. As shown in Figure 4.11 and Table 4.1, the device characteristics are unimpressive.

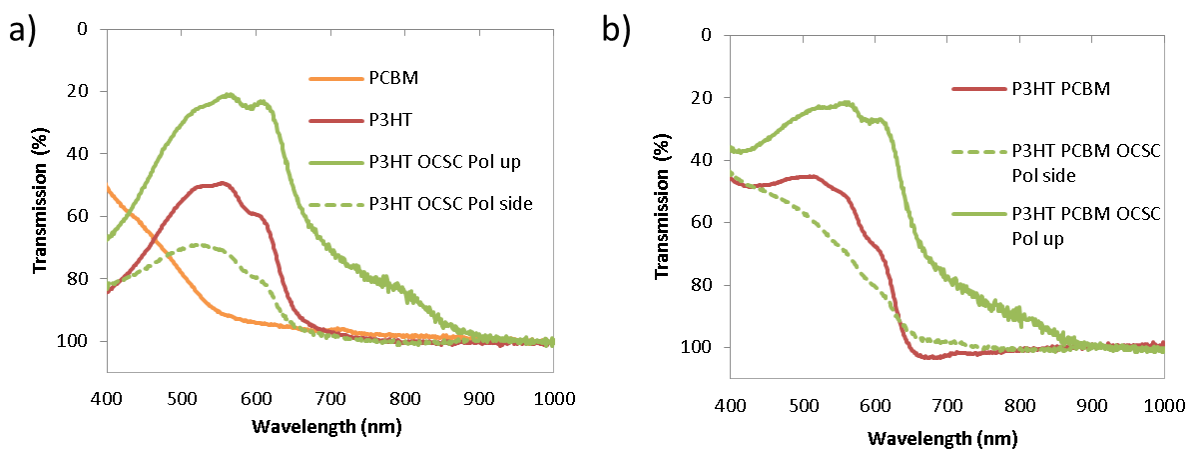


Figure 4.10: Absorption of the constituent films of the in-plane bilayer device before (a) and after (b) contact film transfer assembly of the device.

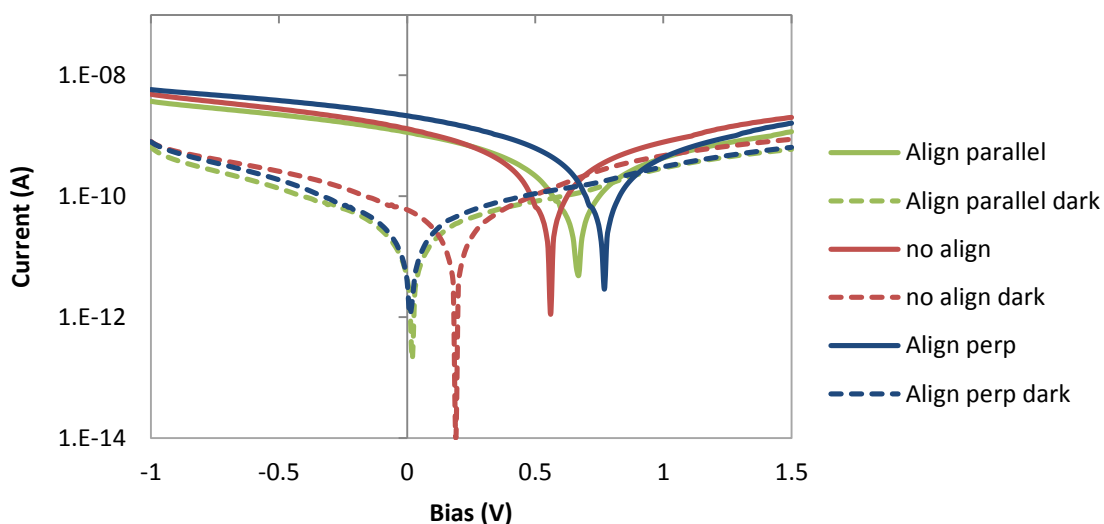


Figure 4.11: The current-voltage characteristics of in-plane planar heterojunction devices where the P3HT layer has alignment parallel or perpendicular to the charge carrier transport direction in the device.

Table 4.1: Photovoltaic characteristics of in-plane planar heterojunction OPVs

	Control	Parallel align	Perp. align
$V_{oc}$	$0.55 \pm 0.02$	$0.65 \pm 0.01$	$0.74 \pm 0.05$
$I_{sc}$ (nA)	$1.3 \pm 0.3$	$1.2 \pm 0.2$	$2.0 \pm 0.4$
FF	$22 \pm 2\%$	$23 \pm 1\%$	$22 \pm 1\%$
Channel (mm)	$0.15 \pm 0.08$	$0.38 \pm 0.02$	$0.21 \pm 0.02$

The fibers between the electrodes clearly show differing orientations, as shown in Figure 4.12, but control over the channel length is difficult due to the manual placement of the electrode evaporation mask. The fabrication procedure involves scraping out a center, bottom electrode before depositing the organic materials (thus there is some missed metal present in the device channel in the micrographs).

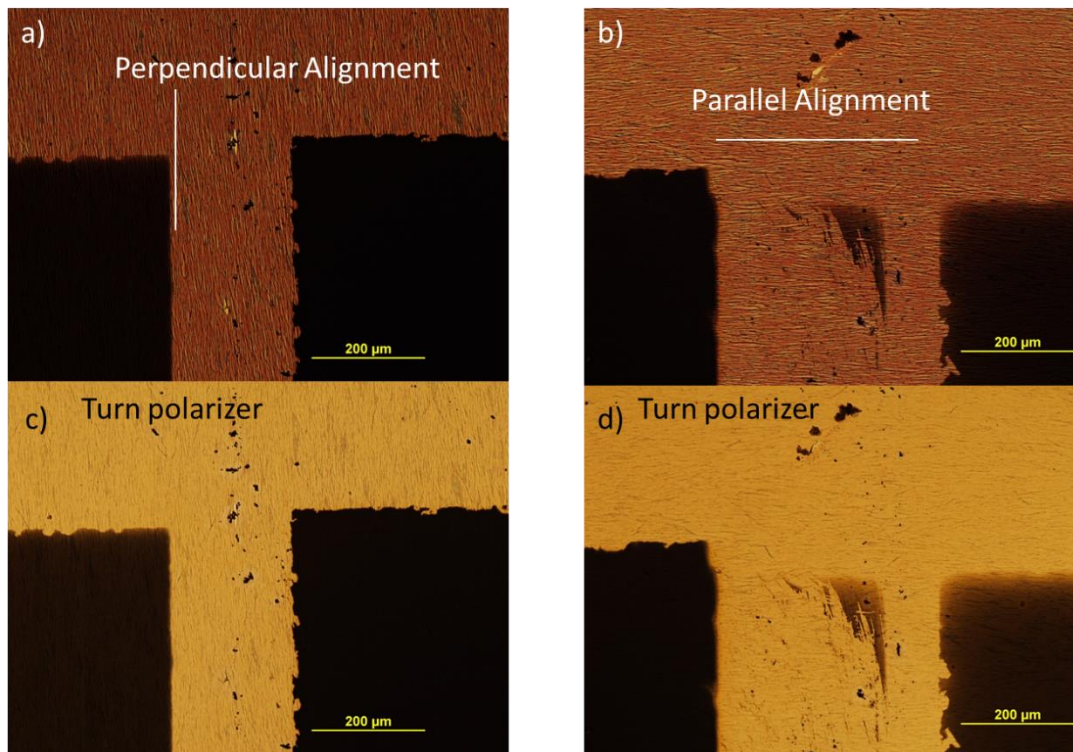


Figure 4.12: Polarized optical microscopy of the in-plane planar heterojunction PSCs reveals controlled alignment of the polymer fibers relative to the transport direction in the devices, in spite of poor control over channel length.

The photovoltaic characteristics of these in-plane devices surprisingly did not show the expected trends. Since transport is easiest along the alignment direction, we expected photocurrent to show a trend with alignment. Not only did the highest photocurrent device have polymer aligned perpendicular to the transport direction, but the differences in photocurrent were not very great. Additionally, attempts at seeing the influence of alignment on photocurrent through polarized illumination did not result in the expected absorption dependence. The fact that the devices did not respond to differences in the alignment of polarized illumination casts doubt on the role of P3HT acting as a light absorber which produced photocurrent in these devices. The FF was unsurprisingly low, given that the charge transport length is three orders of magnitude larger than in typical PSCs; the device curves appear to be greatly limited by the series resistance. Finally, there is a remarkable difference between the  $V_{oc}$  in the devices depending upon alignment. Although it would be reasonable to posit that the higher  $V_{oc}$  in the parallel and perpendicular aligned devices is due to a suppression of charge injection, and therefore recombination, in these resistive devices, this is not the case since the dark curves are all very similar. The  $V_{oc}$  also does not trend with channel length, so the change in  $V_{oc}$  is seemingly coupled to the strangely larger  $I_{sc}$  as an indication that charge extraction is easier as a function of bias in the device where the polymer alignment is perpendicular to the charge transport direction in the device.

This preliminary experiment in the optimization of the alignment of P3HT fibers directed epitaxially by TCB during off-center spincasting reveals that centimeter scale alignment with dichroic ratios of 7-8 can be achieved. The rough, aligned fibers show an interesting absorption or scattering at sub-band gap wavelengths which is not due to the formation of a new chromophore since the emission of the aligned fibers is unchanged. The aligned fibers are applied as an electron donor layer in in-plane planar heterojunction proof of concept PSCs. The performance of the devices indicates that polymer alignment perpendicular to the electrode transport direction appears to be beneficial to device performance, although the role of the polymer as an active absorber in the device is questionable. These results motivate and educate further research into these novel in-plane devices as a method to examine the influence of in-plane polymer alignment on PSC performance.

## Section 6: References

1. Y. Li, Y. Zou, *Adv. Mater.*, 20 2952-2958 (2008).
2. X. Guo, M. Zhang, L. Huo, F. Xu, J. Hou, *J. Mater. Chem.* 22 21024 (2012).
3. Z. Henson, K. Mullen, G. Bazan, *Nat. Chem.*, 4 699 (2012).
4. F. Ishikawa, H. Chang, K. Ryu, P. Chen, A. Badmaev, L. Gomez De Arco, G. Shen, C. Zhou, *ACS Nano*, 3 73-79 (2009).
5. F. Krebs, S. Gevorgyan, J. Alstrup, *J. Mater. Chem.*, 19 5442-5451 (2009).
6. F. Krebs, M. Jorgensen, *Sol. Energy Mater. And Sol Cells*, 119 73-76 (2013).
7. J. Jiang, M. Yuan, K. Dinakaran, A. Hariharan, K. Wei, *J. Mater. Chem. A*, 1 4415 (2013).
8. J. You, L. Dou, K. Yoshimura, T. Kato, K. Ohya, T. Moriarty, K. Emery, C. Chen, J. Gao, G. Li, Y. Yang, *Nat. Comm.*, 4, DOI: 10.1038/ncomms2411, (2013).
9. G. Li, V. Shrotriya, Y. Yao, Y. Yang, *J. App. Phys.*, 98 043704 (2005).
10. M. Kim, B. Kim, J. Kim, *ACS App. Mater. and Interfaces*, 1 1264-1269 (2009).
11. J. Peet, L. Wen, P. Byrne, S. Rodman, K. Forberich, Y. Shao, N. Drolet, R. Gaudiana, G. Dennler, D. Waller, *App. Phys. Lett.*, 98 043301 (2011).
12. W. Li, K. Hendriks, W. Christian Roelofs, Y. Kim, M. Wienk, R. Janssen, *Adv. Mater.*, 25 3182-3186 (2013).
13. L. Murphy, W. Hong, H. Aziz, Y. Li, *Sol. Energy Mater. and Sol. Cells*, 114 71-81 (2013).
14. L. Yang, H. Zhou, W. You, *J. Phys. Chem. C*, 114 16793-16800 (2010).
15. J. Liu, H. Choi, J. Kim, C. Bailey, M. Durstock, L. Dai, *Adv. Mater.*, 24 538-542 (2012).
16. I. McCulloch, M. Heeney, C. Bailey, K. Genevicius, I. MacDonald, M. Shkunov, D. Sparrowe, S. Tierney, R. Wagner, W. Zhang, M. Chabinyk, R. Kline, M. McGehee, M. Toney, *Nat. Mater*, 5 328-333 (2006).
17. B. Huang, E. Glynos, B. Frieberg, H. Yang, P. Green, *ACS App. Mater. and Interfaces*, 4 5204-5210 (2012).
18. J. Kim, Y. Park, D. Lee, J. Lee, J. Park, J. Kim, K. Cho, *Adv. Funct. Mater.*, 20 540-545 (2010).
19. T. Lei, J. Dou, J. Pei, *Adv. Mater.*, 24 6457-6461 (2012).
20. B. Kim, E. Jeong, J. Chung, S. Seo, B. Koo, J. Kim, *Nat. Mater.*, 12 659-664 (2013).
21. H. Tseng, H. Phan, C. Luo, M. Wang, L. Perez, S. Patel, L. Ying, E. Kramer, T. Nguyen, G. Bazan, A. Heeger, *Adv. Mater.*, DOI: 10.1002/adma.201305084 (2014).
22. Y. Yuan, G. Giri, A. Ayzner, A. Zoombelt, S. Mannsfeld, J. Chen, D. Nordlund, M. Toney, J. Huang, Z. Bao, *Nat. Comm.*, 5 DOI: 10.1038/ncomms4005 (2014).
23. A. Tada, Y. Geng, Q. Wei, K. Hashimoto and K. Tajima, *Nat. Mater.* 10, 450 (2011).
24. Y. Zhou, C. Fuentes-Hernandez, J. Shim, J. Meyer, A. Giordano, H. Li, P. Winget, T. Papadopoulos, H. Cheun, J. Kim, M. Fenoll, A. Dindar, W. Haske, E. Najafabadi, T. M. Khan, H. Sojoudi, S. Barlow, S. Graham, J.-L. Brédas, S. Marder, A. Kahn and B. Kippelen, *Science* 336, 327 (2012).
25. C. Muller, M. Aghamohammadi, S. Himmelberger, P. Sonar, M. Garriga, A. Salleo, M. Campoy-Quiles, *Adv. Funct. Mater.*, 23 2368-2377 (2013).

26. D. Motaung, G. Malgas, C. Arendse, S. Mavundla, D. Knoesen, *Mater. Chem. and Phys.*, 116 279-283 (2009).
27. S. Berson, R. Bettignies, S. Bailly, S. Guillerez, *Adv. Funct. Mater.*, 17 1377-1384 (2007).
28. G. Li, Y. Yao, H. Yang, V. Shrotriya, G. Yang, Y. Yang, *Adv. Funct. Mater.*, 17 1636-1644 (2007).
29. A. Montali, C. Bastiaansen, P. Smith, C. Weder, *Nat.*, 392 261-264 (1998).

## Chapter 5: Conclusion and outlook

Organic photovoltaic devices are an interesting research subject. The interfaces in these devices mediate charge injection, extraction, and separation and are sites for recombination and loss during these processes. We have studied the influence of molecular structure at these interfaces on the performance and characteristics of these devices in order to outline molecular design principles to reduce loss and increase efficiency. We placed multilayer spacers at the donor-acceptor interface in order to modify exciton splitting, separation and recombination. With two spacer layers, charge transfer was suppressed but recombination took seven layers in order to reach a minimum. The suppressed charge transfer critically reduced the short circuit current density, but the reduced recombination lead to an increased open circuit voltage. Additionally, the spacer gave an increased charge pair energy at open circuit, plausibly due to reduced coulomb binding, further aiding the increase in open circuit voltage. These findings suggest that a simple molecular spacing change at the donor-acceptor interface cannot completely suppress recombination losses without adversely affecting charge transfer and current generation.

The character of the active layer-electrode interface is crucial for bulk heterojunction solar cells. Charge selectivity at the electrode interface provides diode-like current rectification. This rectification allows photo-generated current to be dominant at low positive and reverse applied bias and enables power generation. We fabricated bulk and planar heterojunction devices without electrode buffer layers and found that charge selectivity is lost when direct contact between the two device electrodes occurs along one of the active layer materials. Interestingly, charge selectivity can be restored by placing thin, insulating buffer layers at the electrode interface to break the percolated direct contact between the electrodes.

The affinity of the electrode interface for the components of the active layer can direct film morphology formation during spincoating and can ultimately influence device performance. When the cathode buffer layer has a strong interaction with the hole-conducting polymer, it separates to this interface and acts as an electron blocking layer at the electron collecting electrode. This results in a device with a reduced efficiency. By placing an additional layer with

low interaction strength between the two strongly interacting layers, the device efficiency is restored.

The electrode-active layer interface is the site of two important processes in photovoltaic power conversion: electron injection and extraction. These processes require the active layer charge transport energy levels to line up well with those of the electrodes- an effect which can be achieved through work function modification. Polymeric materials are found to modify the work function of a common transparent conducting oxide, indium tin oxide, by bearing polar functionality. Acid- or base-like moieties increase or reduce the work function, respectively, as long as they are not accompanied by a heavy counterion. Interestingly, this work function modification is found to occur upon substrates which have the chemical functionality of their surface blocked, implying that the work function modification is not wholly surface mediated. We found that electrophoretically deposited polyelectrolyte films, which have deposited with a charge in response to a charged substrate, modify the work function similarly to spincoated films with acid- or base-like functionality. Further, we found charging like character in XPS spectra of spincoated acid- or base-like polymers. Together, these results support the hypothesis that work function modification by polar polymers occurs due a dipole between static charge within the polymer film and the counter charge on the conducting substrate. These findings help motivate the design of buffer polymers which maintain diode rectification and promote charge injection and extraction without unwanted morphology development.

The conductivity of conjugated polymers forces compromise between light absorption and charge extraction. However, control over the in-plane alignment of conjugated polymers can lead to great enhancements in mobility as the native anisotropic properties are brought out. We optimized the in-plane alignment of P3HT, achieving dichroic ratios of 7-8, with off center spincoating with an epitaxial alignment directing solvent additive. The aligned P3HT films were applied in novel in-plane planar heterojunction devices to see the influence of polymer alignment on charge transport in long transport length devices. The polymer alignment was oriented parallel and perpendicular to the charge transport direction in the planar devices, and differences in open circuit voltage were observed. Contrary to expectation, no great changes in photocurrent were observed, and the best device had anti-transport aligned fibers. These preliminary results act as inspiration for further optimization and experimentation with in-plane devices.

Our studies of the polymer morphology and interfaces in photovoltaic devices shine light upon the loss processes affected by molecular and device structure. We have related guidelines and limitations involved in the design of the molecular structure of the donor-acceptor and active layer-electrode interfaces within polymer solar cell devices. These studies will help guide the design and application of future materials for higher performance devices.

The future of organic photovoltaic development is beckoning. New measurement techniques, new molecules and new device architectures enable control and visualization of processes occurring on very small and very short time and length scales in soft matter. In the past five years the record power conversion efficiency of organic devices has doubled to over 10%. The efficiency of these devices will continue to grow as more researchers join the field and discover and overcome their lifetime and power conversion losses. The practicality of these devices, however, likely depends upon innovative application of their unique processability and flexibility. Many competing photovoltaic technologies are more efficient (above 20% PCE) and cheap enough to already be commercially implemented. The natural utility of organic devices will likely hinge upon the identification of an application where lightweight, mobile, flexible or transparent power conversion outweighs the cost of the power. Even in spite of this, organic photovoltaic devices present an ideal platform for device-oriented materials science study and will continue to attract interest; the properties of these devices rely heavily upon device architecture and material properties, and the materials' properties are so highly tunable that investigations into relationships between these characteristics yield fruitful information about the nature of processes within soft semiconducting materials. These structure-property-processing relationships will continue to enable the design of new, tailored soft materials for high performance applications, and will ensure a bright future for those who pursue them.

## Appendix 1: Additional data

### Section 1: Temperature and light intensity dependent $V_{oc}$ characteristics

This section contains all of the  $V_{oc}$  vs temperature and light intensity curves which were used to estimate the polaron pair energy for each device in chapter 1. The polaron pair energy is taken from the y-axis intercept of the linear region of the  $V_{oc}$  vs temperature plots.

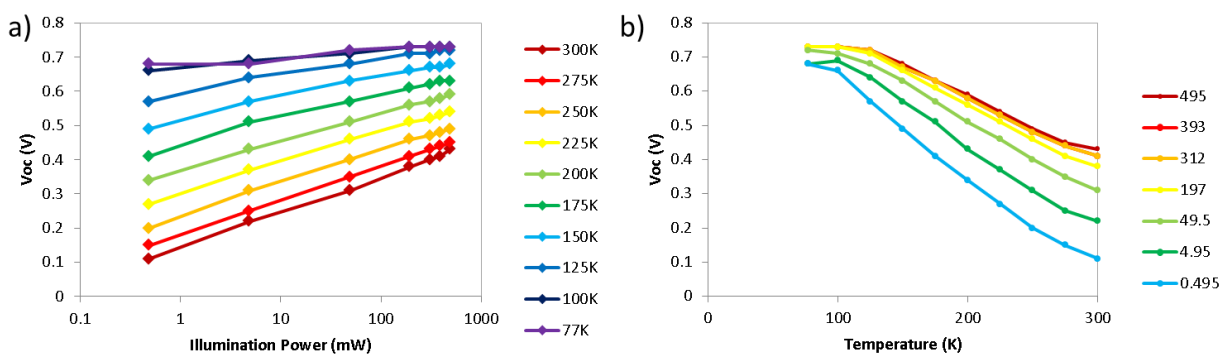


Figure A.1: The temperature (a) and light intensity (b) dependence of a device with no spacer between P3HT and PCBM.

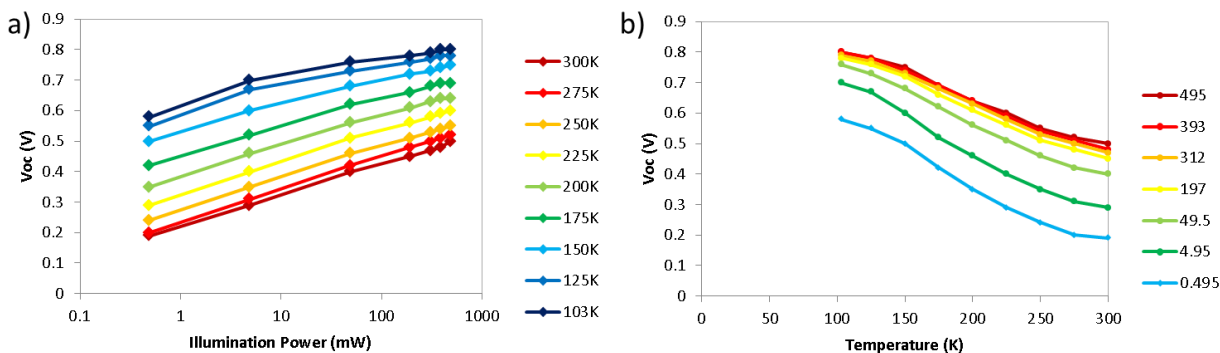


Figure A.2: The temperature (a) and light intensity (b) dependence of a device with one monolayer of PPE between P3HT and PCBM.

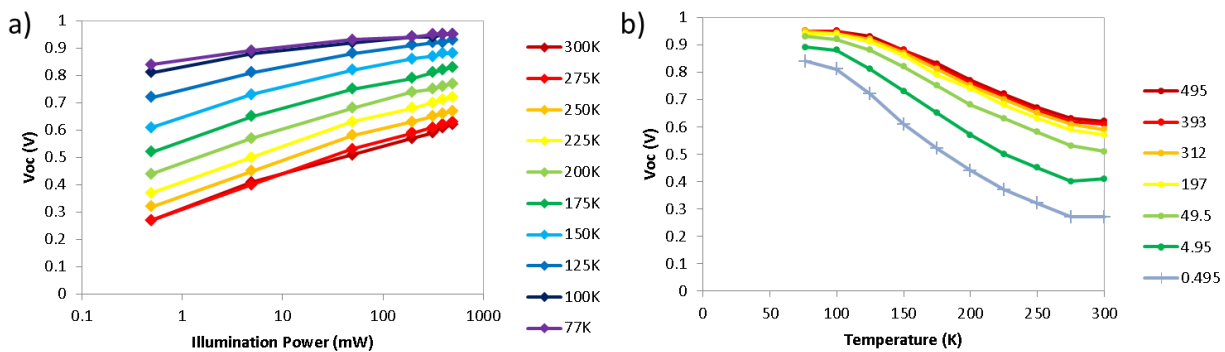


Figure A.3: The temperature (a) and light intensity (b) dependence of a device with two monolayers of PPE as a spacer between P3HT and PCBM.

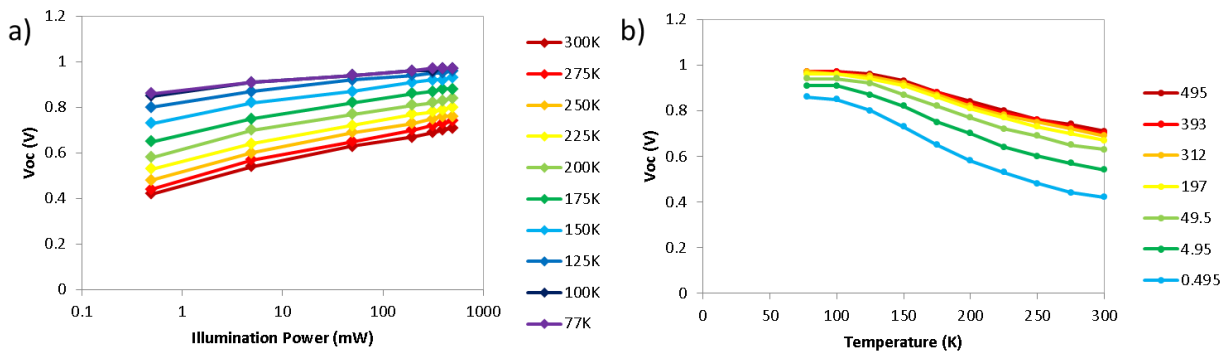


Figure A.4: The temperature (a) and light intensity (b) dependence of a device with three monolayers of PPE as a spacer between P3HT and PCBM.

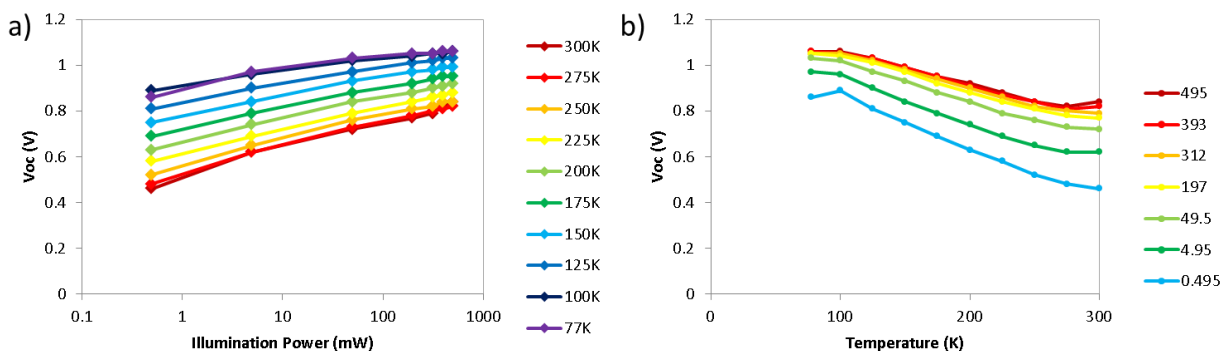


Figure A.5: The temperature (a) and light intensity (b) dependence of a device with four monolayers of PPE as a spacer between P3HT and PCBM.

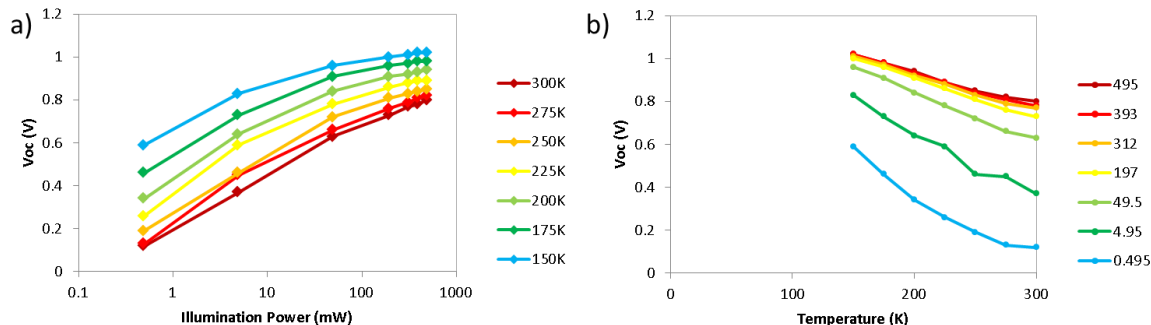


Figure A.6: The temperature (a) and light intensity (b) dependence of a device with five monolayers of PPE as a spacer between P3HT and PCBM.

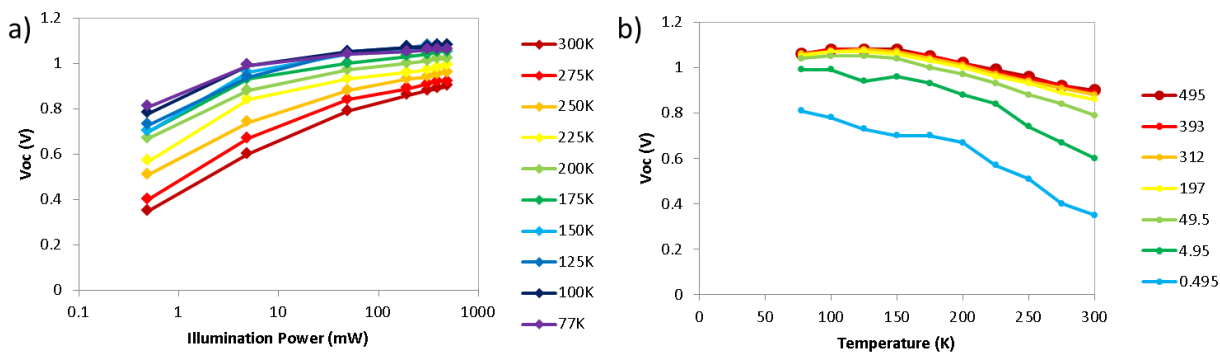


Figure A.7: The temperature (a) and light intensity (b) dependence of a device with seven monolayers of PPE as a spacer between P3HT and PCBM.

Section 2: Ellipsometry data of PCDTBT:PCBM blend films on glass/PEIE

**Sample: Glass-PEIE-PCDTBT-PC70BM-refl**

Fit Results	Optical Model
MSE = 12.521	
Roughness = $1.34 \pm 0.049$ nm	
Thickness # 3 = $54.84 \pm 0.340$ nm	
EMA % (Mat 2) = $81.7 \pm 0.23$	
Thickness # 2 = $1.38 \pm 0.344$ nm	
EMA % (Mat 2) = $0.0 \pm 19.31$	
n of Glass @ 632.8 nm = 1.516	

	Roughness = <b>1.34 nm</b> (fit)
	- Layer # 3 = <b>EMA</b> Thickness # 3 = <b>54.84 nm</b> (fit) # of Constituents = <b>2</b> Material 1 = <b>PCDTBT</b> Material 2 = <b>PC70BM</b> EMA % (Mat 2) = <b>81.7</b> (fit) depolarization = <b>0.333</b> Analysis Mode = <b>Bruggeman</b>
	- Layer # 2 = <b>EMA</b> Thickness # 2 = <b>1.38 nm</b> (fit) # of Constituents = <b>2</b> Material 1 = <b>PCDTBT</b> Material 2 = <b>PC70BM</b> EMA % (Mat 2) = <b>0.0</b> (fit) depolarization = <b>0.333</b> Analysis Mode = <b>Bruggeman</b>
	Layer # 1 = <b>PEIE</b> Thickness # 1 = <b>8.18 nm</b>
	Substrate = <b>Glass</b> Substrate Thickness = <b>1.0000 mm</b>

### Experimental and Model Generated Data Fits

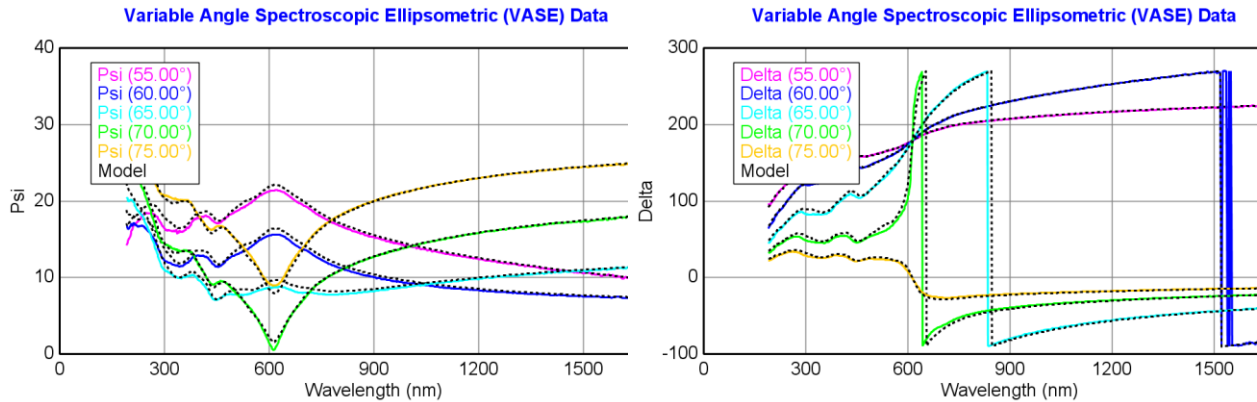


Figure A.8: The model used to fit the PCDTBT:PCBM vertical phase separation with ellipsometric data.

### Section 3: Leakage behavior of diodes depending upon the contact work function

OPV devices made with P3HT:PCBM as the active layer have different behavior depending upon how they are contacted. By choosing contacts with work functions closer to the desired charge carrier travel energy levels on the active layer materials, the diode rectification can be maintained in spite of removing an opposite-side charge selective electrode buffer layer.

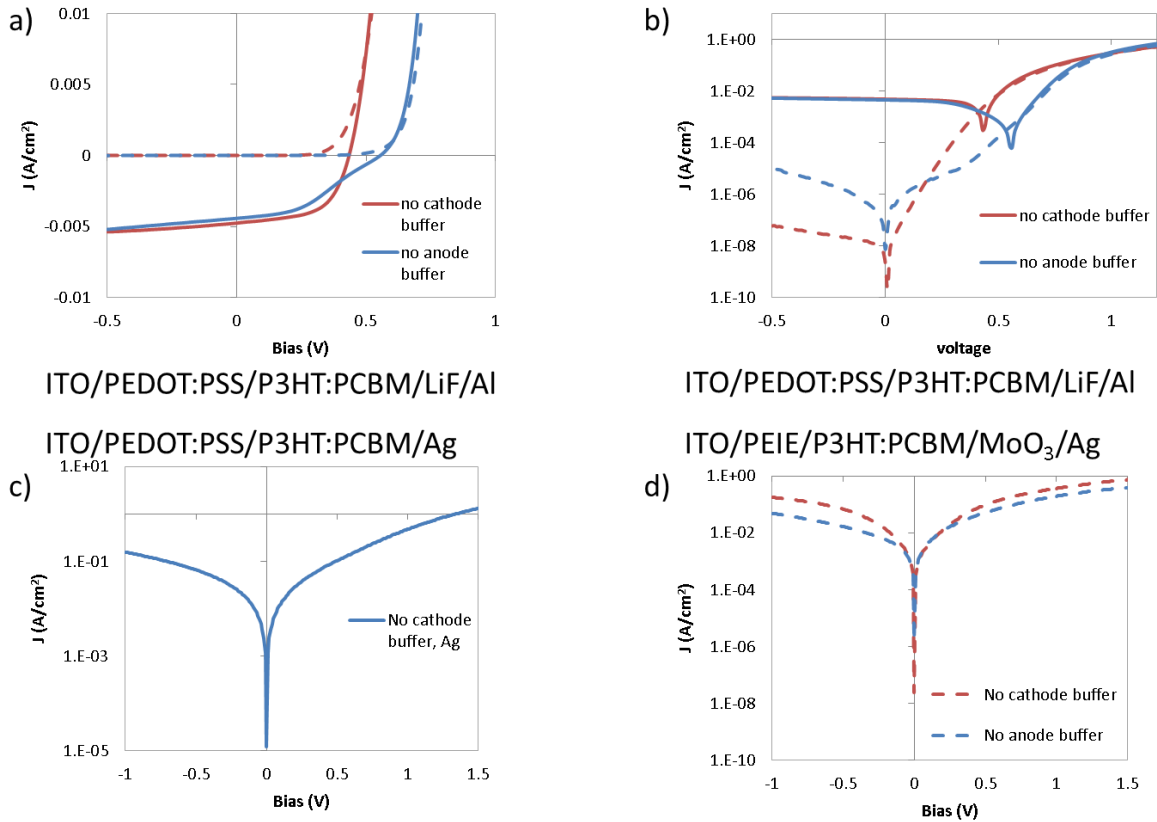


Figure A.9: The J-V characteristics of P3HT:PCBM devices depending upon the materials and buffers used as electrical contact. Some of these give short-like loss of diode rectification (c and d), while others do not (a and b) due to the influence of changing the electrode to one with a different work function.

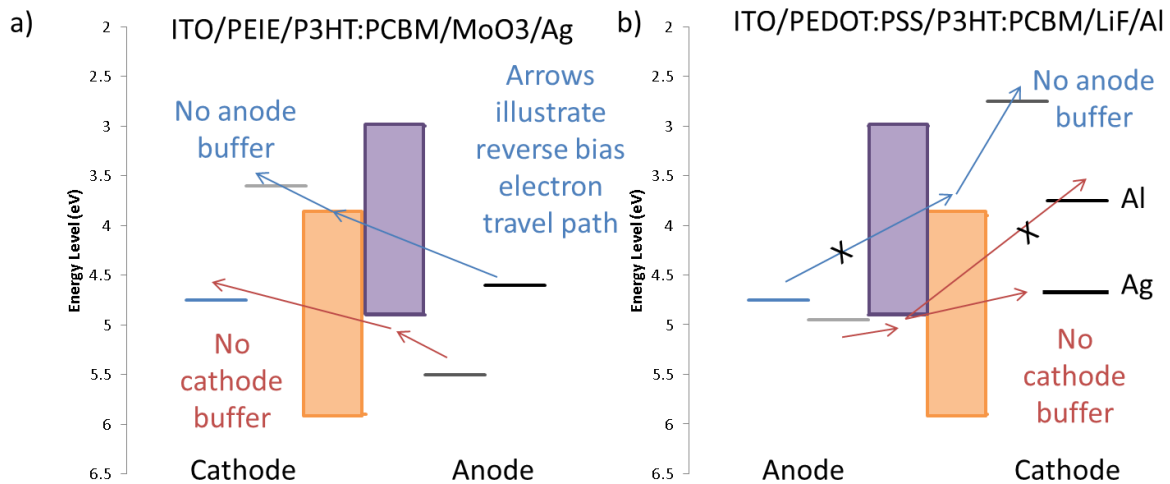


Figure A.10: Proposed electron travel paths across P3HT:PCBM OPVs under reverse bias. Some of the detrimental paths (a) are shut down by choosing contact materials with different work functions (b).

#### Section 4: Information about the homemade kelvin probe

A simple kelvin probe is fabricated with an Arduino UNO R3 electronics controller, and some amplification circuitry, as shown in Figure A.11. The kelvin probe operating principle is such that the contact potential difference between two conductors can drive a current flow if the distance between the conductors changed (they act as a parallel plate capacitor). A computer sound driver (speaker) is used, at a distance, to create a 100 Hz oscillation between two pieces of ITO, one as a reference and one as a sample. At the same time, pulse width modulation (500 Hz) from a digital output on the Arduino is used to partly charge a 100 uF capacitor, creating a smoothed output voltage which varies the backing potential applied to the reference ITO glass.

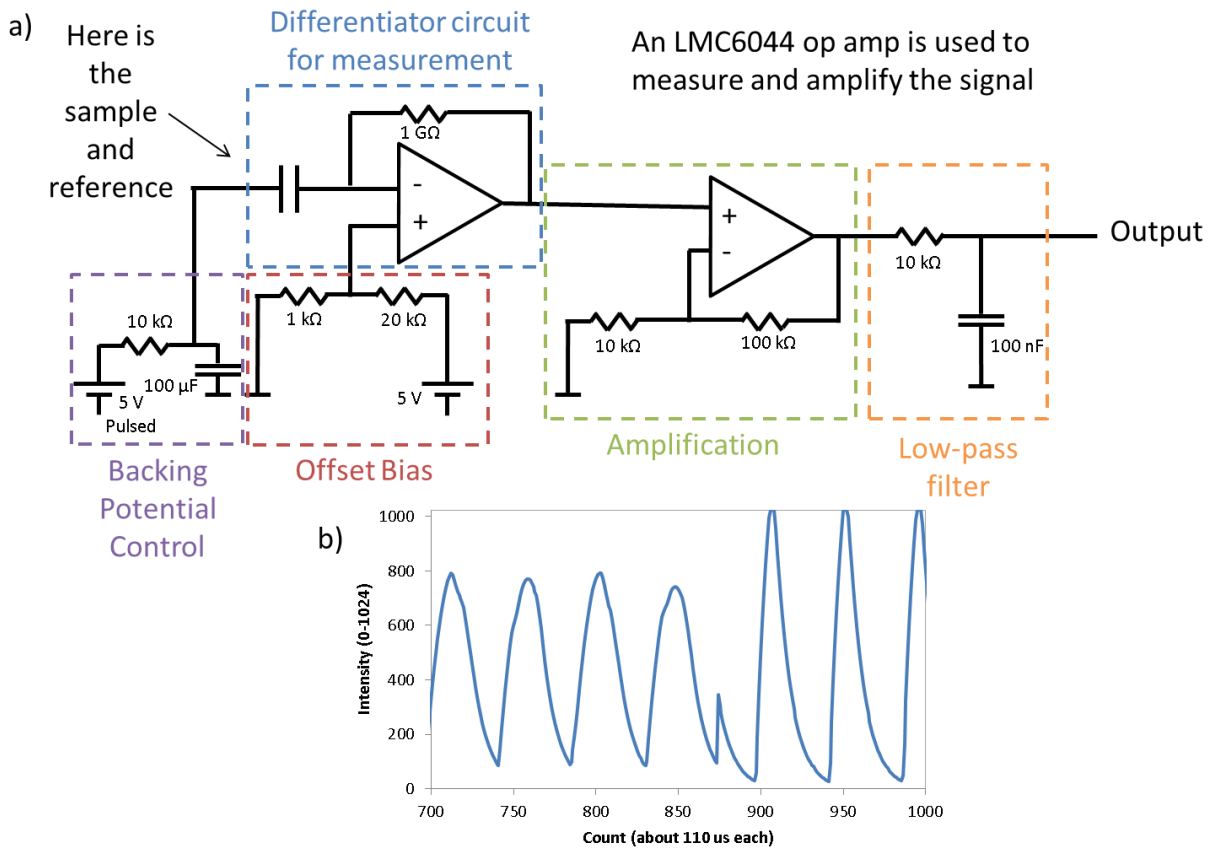


Figure A.11: A simple kelvin probe circuit schematic (a) and sample output signal (b). Different applied bias gives different current oscillation amplitude.

When the reference ITO is biased with a backing potential that matches the work function of the sample, no current will flow in spite of the oscillating distance between the sample and reference. This bias is the contact potential difference.

The kelvin probe is made using a differentiator circuit with an operational amplifier (enabling measurement of the small current coming from the ITO-ITO parallel plate capacitance change), an offset voltage to enable measurement of voltages between 0-5 V (an Arduino limitation), a second amplifier to make the small signal larger, and a filter to remove the amplified pulse width modulation which is inadvertently picked up and amplified in the measurement.

#### Section 5: Survey XPS spectra

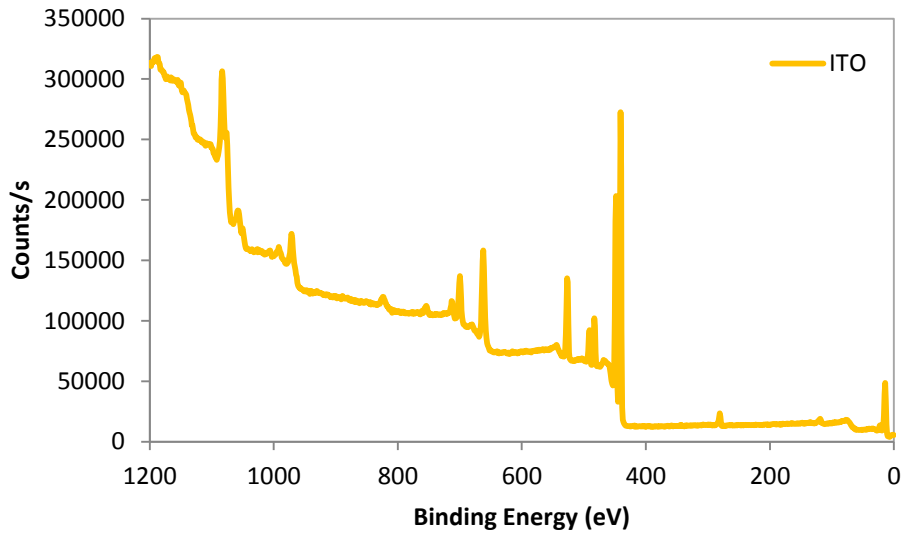


Figure A.12: Survey XPS spectra of ITO.

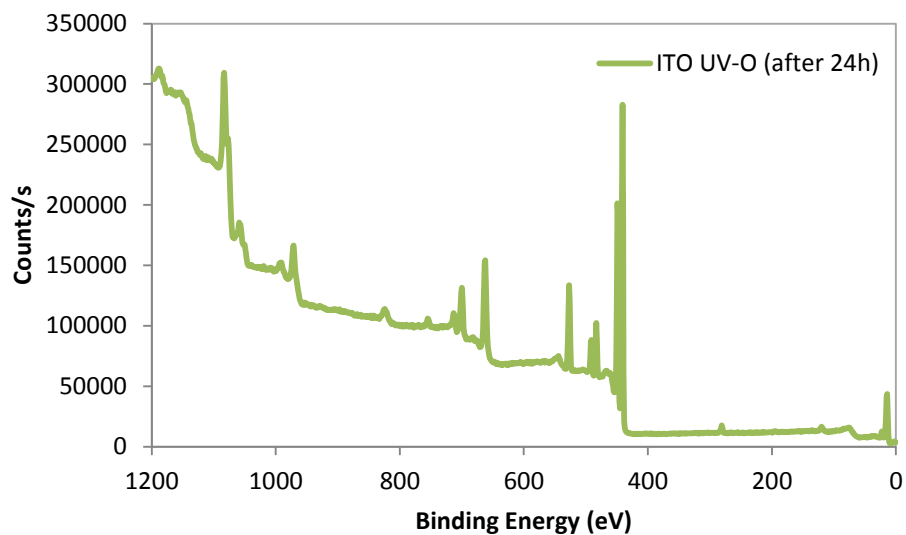


Figure A.13: Survey XPS spectra of UV-ozone treated ITO.

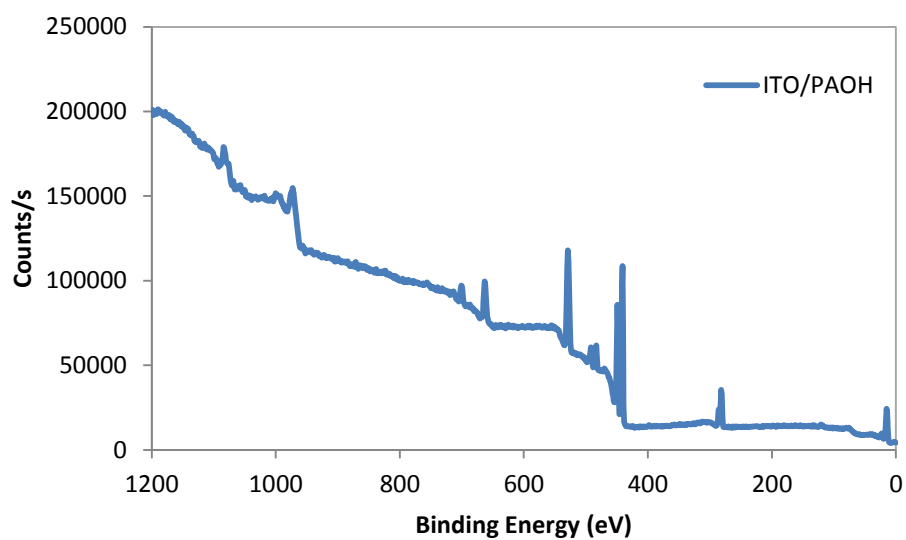


Figure A.14: Survey XPS spectra of poly(acrylic acid) on ITO.

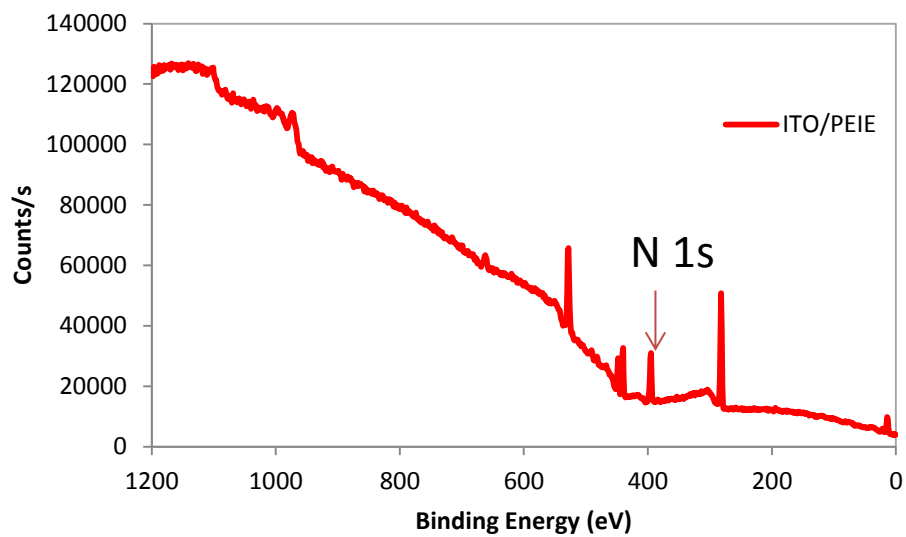


Figure A.15: Survey XPS spectra of poly(ethylenimine) ethoxylated on ITO.